An-Najah National University

Faculty of Graduate Studies

WAFER PROBING MEASUREMENTS OF ITkPix-V1 FOR ITk PIXEL ATLAS UPGRADE

By

Hosnia Saleem Mohammad Salahat

Supervisor

Dr. Ahmed Bassalat

This Thesis is Submitted in Partial Fulfillment of the Requirements for the Degree of Master of Physics, Faculty of Graduate Studies, An-Najah National University, Nablus - Palestine.

2024

WAFER PROBING MEASUREMENTS OF ITkPix-V1 FOR ITk PIXEL ATLAS UPGRADE

By

Hosnia Saleem Mohammad Salahat

This Thesis was Defended Successfully on 3/7/2024 and approved by

Dr. Ahmed Bassalat Supervisor	Signature
Dr. Abdenour Lounis External Examiner	Signature
Prof. Mohammed Abu-Jafar Internal Examiner	Signature

Dedication

I am dedicating this thesis to

My parents, my sister and my brothers

and My aunt who mean a lot in my life.

I am so thankful for their continuous support to me throughout my studying years.

Acknowledgements

Foremost, i thank Allah for granting me to continue my studying journey and write this thesis.

I am forever grateful to Dr. Ahmed Bassalat who guided me during my studying years in university and specially for giving me a chance to do an internship in IJCLab-Orsay in France that prepared me to write this thesis.

I also thank the IJCLab team that I worked with including Ana Torrento and Abdelali Slimani lead by Abdelnour Lounis. In addition to my colleagues, Omar Istaitia and Jenan Zakaria who worked with me and gave me many advices that guided me a lot during my internship period.

Declaration

I, the undersigned, declare that I submitted the thesis entitled:

WAFER PROBING MEASUREMENTS OF ITkPix-V1 FOR ITk PIXEL ATLAS UPGRADE

I declare that the work provided in this thesis, unless otherwise referenced, is the researcher's own work, and has not been submitted elsewhere for any other degree or qualification.

Student's Name: **Hosnia Saleem Mohammad Salahat**

Signature: 

Date: **3/7/2024**

List of Contents

List of Tables

List of Figures

List of Appendices

WAFER PROBING MEASUREMENTS OF ITkPix-V1 FOR ITk PIXEL ATLAS UPGRADE

By
Hosnia Saleem Mohammad Salahat
Supervisor
Dr. Ahmed Bassalat

Abstract

This thesis is related to a Toroidal LHC Apparatus (ATLAS), the biggest general-purpose detector at the Large Hadron collider (LHC). Inside the LHC ring, two high energy hadron beams collide. This collision needs to be detected to check the predictions of particle physics theories, such as the properties of the Higgs boson, which is so crucial to the Standard Model. For that, ATLAS and other detectors were built.

Researchers need to boost the LHC's performance by increasing its integrated luminosity by a factor of ten beyond its design value to maximize discoveries possibility in 2029, known as the High Luminosity-Large Hadron Collider (HL-LHC) plan. ATLAS detector is going under upgrading processes to cope with this higher luminosity, in which its inner detector (ID) that is composed partially of silicon is going to be replaced by a new inner tracker (ITk) consists completely of silicon.

The new ITk is composed of a strip detector and pixel detector. The building blocks of the ITk's pixel detector are the pixel modules which contains readout chips called the ITkPix-V1. Those chips are going under tests to check its suitability to be used in the new ITk. One of those tests is the wafer probing tests.

In Laboratoire De Physique Des 2 Infinite Irène Joliot-Curie (IJCLab), the wafer propping set-up used for this task has to undergo a quality control process to decide its fit to do the tests on the chips, so the main topic of this thesis is analyzing the results of the tests done by the wafer probing set-up of IJCLab on the ITkPix-V1 chips and comparing it to reference measurements done by the University of Bonn on the same chips in order to help qualifying the set-up of IJCLab to do the wafer probing tests. Part of the test results were similar to the reference results while some were not. Depending on the analysis done, some reasons that cause the non consistent results were found.

Keywords: ATLAS; LHC; HL-LHC; ITk; ITkPix-V1.

Chapter One
Introduction and Motivation

The LHC is the most powerful particle accelerator in the world, established by the European Organization for Nuclear Research (CERN) in Geneva. In collaboration with over 12000 scientists and a large number of universities and laboratories, it was commissioned on the 10th of September 2008.

It collides two beams of hadrons that move at a speed closer to the speed of light in opposite directions before being brought into collision in which each beam carries 7 TeV at maximum (1).

It has a 27 km ring of superconducting electromagnets (2) with a series of accelerating structures that increase the energy of the particles all along the way making them move in a speed closer to the speed of light before being brought into collision.

This collision and the particles resulting from it needs to be recorded and analyzed to test the predictions of scientific models such as the Standard Model and measure the Higgs boson properties like its decay and production since it provided remarkable insights to the origin of mass, the Standard Model validity, and the fundamental nature of particles. As well as discovering contradictions that might require development of new physics.

For this reason, huge detectors capable of reconstructing what happened during the collision and keeping up with the massive collision rates were built.

The LHC beams collide at four positions around the ring of the accelerator which corresponds to the locations of four main particle detectors, ATLAS, A Large Ion Collider Experiment (ALICE), Compact Muon Solenoid (CMS) and Large Hadron Collider beauty (LHCb), as shown in figure 1.1 (see Appendix).

ATLAS detector focuses on studying the top quark and searching for the Higgs boson. While CMS provides precise particle momentum measurement and plays an important role in studying the Higgs boson as well as searching for new physics theories.

ALICE is designed to study heavy-ion collisions, which helps to reproduce the early universe conditions and search for the quark-gluon plasma properties. On the other hand, LHCb detector aims to study decays of the particles containing the bottom quark.

Scientists needs to boost the LHC's performance to increase the integrated luminosity by a factor of ten above the LHC's design value, in order to maximize the possibility of discoveries in (3). This process of increasing the luminosity of the LHC is called the High Luminosity- Large Hadron Collider (HL-LHC) plan.

As a result, ATLAS detector has gone and is still going under a lot of upgrading processes after the first run phase of the LHC which was Run 1. One of the important upgrading process that was done to its inner part (ID) was the addition of the Insertable B-Layer (IBL) to the ID of ATLAS in 2014 (4). However, for ATLAS detector to operate properly during the HL-LHC period, it has been going under an upgrading process that aims to replace the whole ID, that consists partially of silicon by an all-silicon ITk (5). This ITk is composed of two detectors, a pixel detector and strip detector.

The chips used to build up the modules of the pixel detector of the ITk should undergo a quality control process in order to decide which ones are good to build up the module. This quality control process includes applying a type of electrical testing called the wafer probing tests on the chips. Before this, all the ITk pixel groups contributing to this task have to qualify its wafer probing set-up performance to do the tests on the chips.

In IJCLab, which is a Mixed Research laboratory of the University of Paris, Centre national de la recherche scientifique (CNRS), and the University of Paris Saclay, located in Orsay-France, IJCLab ATLAS ITk pixel group is working now on this set- up qualification process via performing the wafer probing tests on the ITkPix-V1 chips. This thesis is a detailed analysis of some of the results of these wafer propping tests.

The main goal of the thesis is to help qualifying the wafer probing set-up of IJCLab by analyzing its measurement results done on the ITkPix-V1 chips and comparing it to a reference measurement done by the University of Bonn on the same ITkPix-V1 chips.

- **The Standard Model and the LHC**

The universe is composed of matter and antimatter, and all the matter in the universe is made up of two types of particles which are the leptons and quarks as shown in figure 1.2 (see Appendix).

There are four types of forces or interactions in this universe, which are the strong, weak, electromagnetic, and gravitational.

Table 1.1

The four fundamental forces in the Standard Model (6,7)

Force	Particles that experience it	Force carrier	Range (m)	Strength
Gravitational	Any particle that has a mass	Gravitons (those particles are not discovered yet)	∞	Weaker ↓ Stronger
Weak	Leptons and quarks	W Bosons (W^+ and W^-) Z Bosons (Z^0)	10^{-18}	
Electromagnetic	Every Charged Particle	Photons (γ)	∞	
Strong	Gluons and quarks	Gluons (G)	10^{-15}	

There are four types of forces or interactions in this universe, which are the strong, weak, electromagnetic, and gravitational forces.

Each of these forces has its own mediator or force carrier that belongs to a group of particles called bosons. Particles experience the forces between them through the exchange of specific force carrier according to table 1.1.

Until now, the Standard Model is the considered the best theory to describe the building blocks of the universe (8), it describes how the quarks like neutrons and protons and leptons that includes electrons, made up all the matter in the universe.

However, it's still incomplete, its major problem is the incapacity to include gravity or justify the absence of the graviton (its force carrier).

Moreover, it fails to explain phenomena such as dark energy and dark matter (9) which constitute most of the energy and matter in the universe.

The experiments in the LHC will help us to find the missing pieces in the Standard Model, since its able to reproduce the conditions existed back when the big bang occurred (10) .

It allows physicists to collide high energy particles and observe the interactions resulting from the collision. This is exactly why we need the HL-LHC or why we need to upgrade the detectors because it will help us witness many rare processes that may explain a lot of unexplained phenomena.

- **How LHC Accelerates Particles**

Stage 1: Linear Particle Accelerator 4 (Linac 4)
With 160 Mev acceleration energy (11), Linac 4 has taken the place of Linac 2 in 2020 as an injector to the Proton Synchrotron Booster (PSB), increasing the PSB beam brightness by a factor of two (12).

Linac 4 works to accelerate negative hydrogen ions (H^-), it uses radio frequency cavities for acceleration, in which the H^- passes through a series of accelerating cavities connected to an alternating voltage source that causes the cavities to be charged positive and negative alternately as illustrated in figure 1.3 a) (see Appendix), as a result, the cavities behind the H^- bunches will push it forward and those in front of it would pull, causing them to accelerate.

In Linac 4, H^- source is used with a source of hydrogen gas forming a discharge plasma. Then an electric field is applied to strip off electrons from every hydrogen atom to produce positive hydrogen atom (H^+).

Those H^+ are drawn to a cathode surface that contains cesium. Cesium will reduce the cathode work function to be a better electrons donor to the H^+ which enhances the H^- production.

The H^- leave the ion source with 45 KeV (12) passing through the series of accelerating structures illustrated in figure 1.3 b) (see Appendix), to finally leave Linac 4 with 160 MeV (11).

Stage 2: Proton Synchrotron Booster (PSB)

Two electrons are stripped off from each negative hydrogen ion H^- that leaves Linac 4, this stripping process is done during injection from Linac 4 to the PSB using a carbon stripping foil to create protons that will enter the PSB with 160 MeV energy (12).

The PSB is composed of four stacked synchrotron rings that receive the proton beams from Linac4 with 160 MeV and accelerates them using electric field to around 2 GeV (13). Also, large electromagnets are used to bend their paths round the circles because according to Lorentz force, magnets can exert a force on the accelerating protons at right angles to the direction of motion making them move in circular path. Then the accelerated protons are injected into the third stage of acceleration which is the Proton Synchrotron (PS).

Stage 3: Proton Synchrotron (PS)

The four proton packets are recombined to enter the PS which will accelerate it to 25 GeV (14) reaching 99.9% of the speed of light, as soon as the velocity reaches this limit, the added energy cannot be translated into an increase of the velocity, instead, it translates into increase of the mass of the proton which is the effect of special relativity (mass dilation).

Stage 4: Super Proton Synchrotron (SPS)

The 25 GeV proton packet will enter the fourth stage of acceleration, the SPS, which is the 7 km ring that will accelerate the packet to reach 450 GeV to be ready to enter the 27 km ring of the LHC (15).

Stage 5: The 27 km ring of the LHC

The 27 km ring of the LHC has two vacuum pipes, one in which the protons will move clockwise and in the other one the protons will move counter clockwise.

The protons packet will go round the ring getting a boost of energy in every revolution from the pulsed electric filed, finally, each proton will have an energy of 7 TeV at maximum (16). The two proton packets that move in opposite directions will cross over

and collide in the four detector locations with a collision energy of 14 TeV (16) for each proton-proton collision, which is double that of the opposing protons. Figure 1.4 (see Appendix), shows a schematic drawing of the LHC that illustrates the locations in where the five stages of particle acceleration takes place.

- **Previous Run Phases of the LHC and Current Run Phase**

One of the most crucial LHC achievements came in 2012 by the discovery of the Higgs boson at a centre of mass energy of 7 TeV, with an observed mass of 125 GeV (17). This discovery was the result of the first LHC run phase, Run 1 (18). The detection of the Higgs boson was very important to the physics community since this particle is believed to give masses for all elementary particles, so without the Higgs boson, particles would have no masses and the universe would not be existed as we know it today.

It was followed by two years of shut down which is called the Long Shut-down 1 (LS 1) period. Because of the changes applied during the LS 1, the LHC was ready for a long running period, the main target was to re-establish a high intensity operation with new running parameters.

In 2015, LHC was restarted again for another running phase which is Run 2 for further exploring of the Standard Model's physics at a higher beam energy.

On 3-12-2018, Run 2 ended successfully, during this run phase the LHC performance was beyond expectations, achieving around $16x10^{15}$ proton-proton (p-p) collisions with an energy of 13 TeV, almost double the energy reached in Run 1, recording an amount of data five times more than in Run 1 phase (19).

During Run 2 scientists were able to take detailed measurements of the Higgs Boson interactions and properties (20). Thanks to this second run phase, we were able to know the masses of the top quark, W boson and the Higgs boson with higher precision. These measurements are crucial for considering the Standard Model as a stable theory (21).

After over 3 years of maintenance and upgrading work of the LHC which was the Long Shut-down 2 (LS 2), a new period of data taking which is Run 3 was started in 2022 at a record collision energy of 13.6 TeV per beam for the first time, which is expected to last

until the end of 2025. This run phase is expected to record more data with higher quality than the previous runs (22).

Run 3 have expectations for probing the nature of Higgs boson with unprecedented high precision, and it will look at how strongly it interacts with force particles and matter and whether it decays to give new particles that could make up the dark matter for example (23).

They also expected to search for candidates for the dark matter either by precise measurements or direct searches. The most important one is the interaction between the Higgs boson and the heaviest particle ever (24), top quark since this will be the door to the new physics (23). Figure 1.5 (see Appendix) shows the running plan of the LHC.

- **Physics Goal of the HL-LHC**

Luminosity is an essential indicator of the performance of LHC, It's defined by the ratio of the number of collisions (dN) that take place in a specific amount of time (dt) to the cross section (σ) (25):

$$L = \frac{1}{\sigma}\frac{dN}{dt} \tag{1.1}$$

That is the higher the luminosity, the more information we can get from the experiments allowing us to keep an eye on rare processes like Higgs boson production by the vector boson fusion (VBF), and explore known mechanisms in more depth, as well as witness uncommon new phenomena that may emerge.

The HL- LHC will generate at least $15x10^6$ Higgs bosons each year, compared to roughly $3x10^6$ Higgs bosons from the LHC in the year 2017 (3, 26).

It will also have an instantaneous luminosity of $5x10^{34}$ to $7.5x10^{34}$ cm^{-2} s^{-1}, and will be capable of collecting up to 3000 to 4000 fb^{-1} of data throughout a 10 year period of operation (27). A comparison between the current LHC and the HL-LHC parameters is shown in table 1.2.

Table 1.2

Comparison between the parameters of the current LHC and the expected HL-LHC (27,30)

Parameter	LHC	HL-LHC
Centre-of-mass Energy ($\sqrt{s}$)	13.6 TeV (Run 3)	14 TeV
Peak Instantaneous Luminosity	$2x10^{34}$ cm^{-2} s^{-1} (Run 3)	$5x10^{34}$ to 7.5 x 10^{34} cm^{-2} s^{-1}
Total Integrated Luminosity Throughout the years of operation	254.6 fb^{-1} (Since Run 1 up to the year 2023)	3000 fb^{-1} - 4000 fb^{-1} (By the end of its operation)
Pile-up	50 interactions per bunch crossing (Run 3)	140-200 interactions per bunch crossing.

- **Consequences of Having the HL-LHC**

- Increasing the luminosity to reach $7.5x10^{34}$ cm^{-2} s^{-1} (27) will increase the radiation dose, where the radiation fluence around the region of interaction will be greater than $2.2x10^{16}$ n_{eq}/cm^2 (31) requiring more radiation-hard components in terms of readout electronics and sensors.
- The increase in radiation dose will degrade the current detectors and damage the sensors. To be able to withstand these harsh conditions, the detectors must go under a lot of upgrading processes.
- Increasing the pile-up to 200 collisions per bunch crossing (30) will also need a detector that can cope with the higher readout rates.
- Thermal Effects: The HL-LHC will increase the amount of power deposited in the detectors, resulting in high thermal loads. Therefore, we must have effective cooling systems to ensure the efficient performance of the electronics and sensors, saving them from thermal damage.
- The increased collision rate will result in higher data rates, which evolve challenges regarding data analysis and storage. As well as complicating the isolation of individual collisions events for the purpose of studying them .

- **What will the HL-LHC bring to the scientific community?**

- The main result of Run 1 phase of the LHC in 2012 was the discovery of the Higgs boson, its interaction strengths and couplings with other particles are measured with aprecision that lies between 15% and 30% by CMS and ATLAS. However with 3000 fb^{-1} expected luminosity in the HL-LHC period, the precision will increase (i.e. 5% more) (32) .
- Those measurements and other measurements are important because the deviation of Higgs boson properties from the expectation of the Standard Model suggests the existence of new physics, so we must have the highest experimental precision to explore the highest energy scales using Higgs boson indirectly as a tool (32) .
- The HL-LHC will give us experimental access to Higgs boson couplings with particles from the second family, through the studies of the: $H \longrightarrow \mu\mu$ decay where μ is the moun particle (32).
- Supersymmetry (SUSY) is a crucial theory because it aims to fill the Standard Model gaps, be able to find candidates particles for dark matter and explain the light mass of the Higgs boson. The HL-LHC will allow for precise measurements of the Super-symmetric particles properties such as measuring their masses, their production rates and decay modes with more accuracy.
- Theories with extra dimensions that could explain why the gravity force is so weak compared to other forces would be explained, also the HL-LHC would enable the experiments to boost observations of new interactions and new particles.

Chapter Two
ATLAS Experiment at the LHC

2.1 ATLAS Detector

ATLAS, the biggest volume particle detector in the world , is one of the LHC's two general - purpose detectors while CMS is the other one (33, 34) .

It looks at a variety of physics topics, from the quest for the Higgs boson to additional dimensions and particles that might make up the dark matter, figure 2.1 (see Appendix) shows ATLAS detector illustrated in it its four main components.

ATLAS detector is mainly made up of four sub-detectors which are the Inner Detector, the Magnet System, the Calorimeters and the Muon Spectrometer.

- **The Inner Detector (ID)**

The innermost region of ATLAS detector is the ID which is explained in detail in section 2.2.

- **ATLAS Magnet System**

A magnetic field is needed to separate and measure the momentum of the charged particles resulted from the p-p collision at the LHC (35). For this purpose, a magnet system that is constructed from four superconducting magnets which are a central solenoid, a barrel toroid and two end-cap toroids, were built. The three toroids are illustrated in figure 2.2 (see Appendix).

The central solenoid is basically a one layer coil that is wound in a cylinder as shown in figure 2.2 (see Appendix) and is surrounded by a liquid argon (LAr) calorimeter that is detailed later in this section. This solenoid provides the ID with a 2T magnetic field (36).

On the other hand, the three toroids are made up each of eight superconducting coils that are connected with each other in series and are arranged around the beam line as shown in figure 2.2 (see Appendix). These toroids generates the needed magnetic field for the muon spectrometer.

ATLAS Calorimetry System

The Calorimetry system of ATLAS is basically constructed from two main calorimeters shown in figure 2.3 (see Appendix). The two calorimeters are :

A**.** The Liquid Argon (LAr) Calorimeter

This calorimeter is divided into sections of electromagnetic and hadronic parts as illustrated in figure 2.3 (see Appendix). Its structure made up from absorbers that includes metals like copper, tungsten or lead and liquid argon. Its function is to measure the energy of particles like photons, electrons and hadrons which are produced from the p-p collision at the LHC through the following method:

First, the absorbers absorb the energy of the particles that interacts with it and convert it to a shower of new particles that have a lower energy. Then those lower energy particles decay then into other particles with much less energy. This process of producing lower energy particles with each decay stops when the daughter particles of the decay do no longer have an enough energy to produce other particles.

The lower energy produced particles then ionize the liquid argon existed between the metal layers and the energy of each daughter particle is measured by observing the ionization that they did to the liquid argon.

and the free electrons that resulted from this ionization process are then extracted via an electric field that is generated by a voltage applied to the argon, hence, detecting these free extracted electrons as a current. The current magnitude is proportional to the electrons number which is on its turn proportional to the amount of deposited energy by the all the shower particles which is equal to the energy of the initial particle.

B**.** The Tile Calorimeter

It lies in a location surrounding the LAr calorimeter and consisting of one fixed barrel and two moveable barrels as shown in figure 2.3 (see Appendix). Its structure is made up from steel plates that works as absorbers and plastic scintillators that emit light when its exited.

This calorimeter is a hadronic calorimeter that is designed specially to measure the energy of the hadrons that didn't deposit all of its energy in the LAr calorimeter through the following method:

When the particles produced in the p-p collision hits the calorimeter material, it produce a shower of particles that excites the plastic material when it interacts with it which on its turn generates photons that are converted then to electrical signals through photo-multiplier tubes. The electrical signal strength is proportional to the energy of the shower particles which is equal the energy of the particle that hits the calorimeter material first.

ATLAS calorimeter has shown a successful performance during the Run 2 phase of the LHC, and is expected to continue the good operation at the end of Run 3 Period of the LHC (37-39).

- **Muon Spectrometer**

The muon spectrometer is the outer and final element of ATLAS detector and is constructed from three main regions, which are the barrel region and the two end-caps. The muon spectrometer region in ATLAS detector is shown in figure 2.1 (see Appendix). This spectrometer is designed specially to detect a specific type of particles, which is the muons and measure their momentum.

Muons are one of the subatomic particles that are identical to the electrons but with a larger mass. They are one of the leptons that includes neutrinos, electrons and their antiparticles.

They are resulted from the p-p collision that happens in the LHC and because of its large mass and hence its low interaction with materials, it can pass via the ID and Calorimeter without being detected. That's why the spectrometer is designed specially to detect this type of particles. Its important to detect muons because its signals enables the predictions and deductions about particles that arises from protons impact.

The muon spectrometer uses monitored drift champers which is basically tubes that is filled with a mixture of Ar and CO_2 gases with an anode wire positioned at each tube center. The gas mixture is ionized when the muons pass through it (40), leaving behind them tracks in these tubes. Then the free electrons resulted from the ionization drift toward the anode wire as a result of an applied electric field between the central wire and the tube wall, the electrons tracks are then registered to be used in the muon track reconstruction.

› Magnet System of Moun Spectrometer (Toroid Magnets)

The magnetic system of the muon spectrometer is constructed from three superconducting systems, one system for the barrel region and another two systems for the two end-caps. Those three magnetic systems are the three toroids that i mentioned before as a part of the atlas magnet system. Those toroids are illustrated in figure 2.2 (see Appendix).

Those magnet systems are chosen to have an air core not an iron core despite the fact that the iron core would help to provide a stronger and more uniform magnetic field because the air core would be useful to minimize the multiple scattering, hence reduce the momentum measurement degradation, which is more important than the magnetic field uniformity in our case. Because of this, the magnetic field generated by those eight coils is not completely toroidal and has a strength of 0.5 T (41) .

- **How Different Particles Interact with ATLAS Sub-detectors**

As previously mentioned, ATLAS detector is made up of different layers that detect different types of particles. New high energy particles resulting from the collision occurs in the LHC travel throughout the layers of ATLAS as illustrated in figure 2.4 a) (see Appendix). Each type of particle interacts differently with the detector which helps us to distinguish each one from another.

The process of particles crossing through sub-detectors of ATLAS can be explained by the following:

- As illustrated in figure 2.4 b) (see Appendix), we have four chambers: the tracking chamber which is the ID, the electromagnetic calorimeter, the hadronic calorimeter, and the muon chamber.
- The ID, which its layers are shown in figure 2.5 a) (see Appendix),is submerged in a magnetic field that works to bend the particles paths as they passes along its layers, so that it can measure their trajectory (42-44) as shown in figure 2.5 b) (see Appendix), only charged particles leave tracks in the ID.
- Here is how different particles interact with ATLAS sub-detectors:

A. Electrons and positrons: they leave tracks in the tracking chamber where also a magnetic field is applied to enable momentum measurement, then they deposit all their energy in the electromagnetic calorimeter.

B. Photons: they are uncharged, so they don't leave tracks in the tracking chamber, but they deposit their energy also in the electromagnetic calorimeter.
C. Charged hadrons like protons: they leave tracks in the tracking chamber, but they deposit all their energy in the hadronic calorimeter because the electromagnetic calorimeter material is not massive enough to stop heavy particles like hadrons.
D. Uncharged hadrons like neutrons: they leave no tracks, but they deposit their energy in the hadronic calorimeter.
E. Muons: they pass through all the detector layers leaving tracks and they deposit small amounts of energy in all the calorimeters so they can pass through without being detected either by the ID or by the calorimeter so they are detect by the muon spectrometer as was mentioned previously in this section. Also, in the muon spectrometer, a large magnetic field applied to measure their momentum.
F. Neutrinos: they don't leave any track since they are uncharged and because of their little mass, they barely interact with the material, so their presence is detected by noting the missing momentum and energy in collisions.

The tracking chambers reveal the paths of charged particles through the tracks they leave behind by ionizing the atoms of the detector material when they pass through it and these ionized atoms give rise to an electric current that can be recorded as computer data, then the patterns of the tracks recorded by the detector is reconstructed by a computer program and displayed on the screen.

Regarding the charge of the particle, it is determined by its path curvature in the magnetic field and from these information, the particle momentum can be calculated as explained later in subsection 2.4.2 .

On the other hand, the calorimeters measure the energy lost by the particle by forcing it to deposit all its energy when it passes through. The electromagnetic calorimeter measures the energy of electrons, positrons, and photons as they interact with the charged particles inside the matter, while the hadronic calorimeter measures the energy of hadrons like protons and neutrons as they interact with the atomic nuclei.

2.2 ATLAS Inner Detector (ID)

The inner detector of ATLAS which is illustrated in figure 2.6 (see Appendix), is extremely compact and delicate, made up of three separate sensor systems, all of which are submerged in a magnetic field that is parallel to the beam axis. The charge, momentum and direction of the electrically charged particles created in each p-p collision are measured by the ID (45).

The Transition Radiation Tracker (TRT), the Semiconductor Tracker (SCT), and the Pixel Detector are the three major components of the ID.

1. Pixel Detector

The pixel detector of ATLAS is explained in detail in section 2.3.

2. Semiconductor Tracker (SCT)

The SCT of ATLAS detector shown in figure 2.7 a) (see Appendix), is basically a silicon strip detector that has a cylindrical shape and surrounds the pixel detector of the inner detector. It is made up of four-barrel layers and nine disks on each end cap of the cylinder.

The region occupied by the SCT is the volume enclosed between the smallest barrel layer that lies 30 cm away from the LHC beam line and the last layer that located 52 cm from the beam line, while the length of the cylinder in the beam line direction is 5.6 m, providing over a $|\eta| = 2.5$ of pseudo-rapidity (46).

The main building block of the SCT is the silicon strip modules. The barrel part of the detector is constructed from 2112 silicon strip modules while each end-cap is populated with 988 silicon strip modules (46).

Regarding the barrel part, each one of these barrel modules is made up of two pairs of silicon strip sensors that are attached back-to-back on a baseboard of pyrolytic graphite, this baseboard works to transfer the heat resulted from the sensors and the readout electronics to a cooling pipe. Each module has strips that lead to 1536 readout channels. Those strips are readout by front-end electronics which are the front-end (FE) chips, that is, each sensor pair has six readout chips which means that each one of these chips can readout 128 strips (47).

For the end-cap modules, they are mounted on three rings existed on each disk, the inner, the middle and the outer rings. Modules that are used in the inner ring are constructed from two silicon sensors whereas the outer and middle rings are populated with modules that have four sensors.

When the charged particle resulted from the p-p collision passes through the silicon material, it ionizes it along its track which generates a trail of free electrons that will drift to the closest strips under an electric field applied across the silicon material which will on its turn result in a current signal. From this signal, we can determine the particle track. The information about the particle's position is determined based on the strips that detects its signal. That is, because each one of these strips has a particular location on the silicon surface, if a strip gives a signal, we know that the original particle should have passed somewhere close to this strip.

The SCT has shown a smooth and successful functionality during Run 1 phase of the LHC (48), that is, 99% out of 6.3×10^6 strips were operating perfectly (46). The basic reasons of the non-functioning strips were the disabled modules which contributes to about 0.73% of the whole number of modules, the non-working FE chips that constitute around 0.11% and the disabled strips with a percentage of 0.18%. Approximately, half of the non-working modules were due to cooling issues and high voltage/low voltage problems (48).

It also showed an excellent performance during the Run 2 period, where the peak luminosity of the LHC reached 2.1×10^{34} cm^{-2} s^{-1} which was two times more than the luminosity during the Run 1 phase (49).

Regarding the Run 3 phase of the LHC that started in 2022, the SCT operated successfully since it started and is expected to keep the excellent performance at the end of this running period (49).

3. Transition Radiation Tracker (TRT)

The TRT illustrated in figure 2.7 b) (see Appendix), is the third and outermost element of the ID, extending to have a radius of of 108 cm from the interaction point (50).

Its a gaseous detector that is constructed from around $3x10^5$ straw tubes that have a diameter of 4 mm. At each tube center, there is a wire of tungsten that has a diameter of 31 μm (51). The tungsten wire is kept at ground potential while the tube itself has a potential of 1.5 kV. Those straw tubes are filled with a mixture of different gases which are, Xe, CO_2 and O_2 (52) and their walls are built up from polyimide.

The high voltage and gas mixture are chosen in order to reach the needed transition radiation performance and to achieve the required stability.

The TRT is composed of two regions, the barrel region that has 52544 straw tubes, each is 1.5 m long and lying parallel to the beam line. This barrel part occupies a region that has a radius extends from 50 to 110 cm from the interaction point, covering up to $|\eta| < 1$ of pseudo-rapidity (52).

The straw tubes populated in the end-cap regions are arranged in a vertical direction to the beam line. Each end-cap region is constructed from 122880 tubes covering a pseudo-rapidity that ranges from $1 < |\eta| < 2$ (52).

› How TRT detect Particles?

While the charged particle resulting from the p-p collision passes through the gas mixture inside the straw tubes, it ionizes the gas along its path. As a result of this ionization, free electrons will come out and these free electrons moves then towards the central wires under the electric field effect that is generated by the 1.5 kV voltage mentioned before. By calculating the drift time that the free electrons takes to reach the wire, the position where these electrons were released can be known, hence, the tracking of the particle path.

Also, when the particle traverse the medium boundary between the gas mixture and the tube wall it emits the transition radiation which is a type of electromagnetic radiation that is emitted when a charged particle passes through a boundary between different two media. Then the TRT detects the emitted transition radiation which its amount differs from one particle to another based on their mass, that is heavier particles emit less transition radiation than lighter ones with the same momentum, and by analyzing the emitted transition radiation, researchers can differentiate between different particles.

The TRT exists in the inner detector of ATLAS in Run 1 and Run 2 phases of the LHC(53) in a addition to the Run 3 period which is still going on now in 2024. But the conditions

of high radiation and pile-up during the previous running phases caused high hit occupancies of the TRT, and due to the fact that these conditions is going to be even more strictest during the HL-LHC period which is expected to start in 2029, especially when the spaces between the particles tracks becomes nearly comparable with the diameter of the straw tubes of the TRT as a result of the dense particle environment, the TRT is planned to be completely removed from the ID of ATLAS and the whole ID is going to be upgraded and replaced by a new all-silicon ITk (5).

2.3 Pixel Detector of the ID

The pixel detector of the ID is the innermost part of ATLAS detector, lying 3.6 cm away from the beam line (54). Because of this very close position to the beam line, it is exposed to the highest rate of radiation doses and hits which made it an extremely critical and sensitive part of the experiment, that is, its design should qualify it to withstand this high radiation without being damaged.

On the other hand, because of this proximity of the pixel detector, it can detect particles that can't be detected further away, like particles with short life time that decays so fast, that is, the detector can detect them before they decay to other particles thanks to its closeness to the beam line. It also helps to reduce the multiple scattering effect, that is, the particles resulted from the collision may deviate from its original track as a result of the interactions with the material of the detector itself or with other particles resulted from the collision and these interactions will increase the inaccuracy in determining the correct track of the particle.

The detector has a cylindrical geometry and is constructed mainly from three-barrel layers which are the barrel layer 0 or the B-layer, the barrel layer 1 and the barrel layer 2, with three similar end-cap disks at each end of the detector as shown in figure 2.8 (see Appendix). The main building blocks of the pixel detector layers is the pixel modules which are explained in detail in subsection 2.3.1.

2.3.1 Pixel Modules of the pixel detector of the ID

The main building blocks of the pixel detector is the pixel modules, where each module is constructed from FE readout chips called the FE-I3 chips that are connected to a single silicon sensor via solder bumps. The selection of silicon for the bulk material of the sensor

was based on its low cost and its electrical properties that made it a superior material for detection such as its small band gap.

The silicon sensors, FE readout chips and the solder bumps are all explained later in this subsection. All modules used in the pixel detector are functionally identical (55).

The assembly is glued then to a flexible printed circuit board (flex PCB) to provide electrical contact. The flex PCB is designed specially to be bendable. It is made from a flexible plastic material which is the polyimide, at where the flexible circuit that involves integrated circuits are attached. This kind of flex PCBs are preferred over the rigid ones due to their flexibility and lighter weight.

In the pixel module, the flex PCB works as an interface that provides data connection and voltages for the readout chip. It also provides the p-n junction of the sensors with the reverse bias voltages. Via this reverse bias voltage, the detector can work effectively to detect particles as explained in detail in subsection 2.3.3.

- **Sensors**

The pixel sensors are the most sensitive element of the module and plays the crucial role in detecting the charged particles resulted from the p-p collision, so it has to meet the strictest constrains regarding the thickness, in addition to the efficiency in collecting the charges. At the same time, it must be able to sustain a large amount of radiation damage. The selection of the bulk material used to build the sensor and the design of the sensors plays the main role in ensuring all these criteria.

The sensors used in the pixel modules are called planar sensors, which is basically a type of sensors that uses silicon as the bulk material due to its high resistivity and effective charge collection and the electrodes used in this sensor are attached on the surface of the silicon material.

The complete process of how these silicon sensors works in integration with the other parts of the pixel module to detect the charged particles is explained in detail later in subsection 2.3.3.

- **Readout Chips**

The readout chips is one of the most important parts in any pixel system as its responsible of converting the detected signal by the sensors from analog to digital so it can then be processed and studied by computers. It also contains amplifiers that works to amplify the signals in order to be easier to read it out. Moreover, it works to improve the data quality collected by the sensors by processing the electrical signals through many ways such as, filtering the background noise that guarantee reliable and precise measurements.

Those readout chips works in integration with the sensors in order to guarantee an efficient transfer of the signal in addition to the noise and interference minimization, which on its turn leads to an overall enhancement of the performance of the pixel system. FE-I3

The readout chip that was used in the pixel detector of ATLAS during the Run1 phase of the LHC has gone under three stages of production to reach the final form which is the readout chip.

The first produced chip comprised the basic functionalities only, which leaves a room in the pixel for adding another functionality for improvements, for example, the second chip includes many additional features such as voltage drop recompense. In the end, we had the final form which is the FE-I3 read out chip.

- **Solder Bumps**

The solder bumps that used to connect the silicon sensor to the readout chips in the pixel module is basically a small ball that have a diameter that ranges from a scale of (Tens-Hundreds micrometers) and are made up of an electrically conductive material like the lead tin (Pb-Sn), this material has an extremely high conductivity and can form very strong bonds between the readout chips and the sensors.

They have a spherical shape in order to ensure a larger area of connection between the bonding pad of the device and the bumps surface compared to the cylindrical-shaped bumps for example, which will ensure the uniform and strong contact between the readout chips and the sensors. Figure 2.9 (see Appendix) shows the solder bumps layer that used to connect the sensor layer to the read out one.

The parameters of the pixel module that was used in the pixel detector of the ID including the FE-I3 chips number, the sensor thickness, the number and size of pixels in the sensor are shown in table 2.1.

Table 2.1

Parameters of the ID pixel modules (56,57)

Parameter	Value
Sensor thickness	250 µm
FE-I3 chips number	16 chips
Number of pixel	47232 pixels
Pixel size	50 x 400 μm^2

2.3.2 Hybrid Silicon Detector

The pixel detector of the ID is a hybrid silicon pixel detector which is is a type of detector that is used to give a precise detection of the charged particles when they pass through its silicon sensor material.

The building block of the hybrid silicon pixel detector is the module which is basically a pixel matrix that is illustrated in figure 2.10 a) (see Appendix), it consists of three layers which are the silicon sensor layer, the readout chip layer and a solder bumps layer that electrically connects the readout layer with the sensor one.

The readout chip is made up of a number of readout pixels called pads, each pad is connected to a corresponding pixel on the silicon layer. Figure 2.10 b) (see Appendix) shows a pixel cell from the pixel module that includes a pad connected via a solder bump to the pixel sensor.

The silicon sensor layer consist of pixels where each pixel represents a pn-junction diode, which is a junction or interface formed between two types of semiconductor materials, n-type and p-type. The semiconductor material in our case is silicon (^{14}Si).

In n-type silicon material, the silicon is doped with an element from the 5th group in the periodic table, resulting in an excess of the negative charge because in each silicon atom there is four valence electrons, so when its doped with an element from the 5th group, for example, the phosphorus (^{15}P) whose atom has five valence electrons, four of these electrons will bond with the four valence electrons from the silicon atom as illustrated in figure 2.11 a) (see Appendix), and one electron will be left free, so there will be an excess

of negatively charged carriers or electrons in the silicon material, that's why it's called n-type.

The p-type silicon material is formed via doping the silicon with an element from the 3^{ed} group, for example, the boron (^{3}B) were those elements misses the 4th valence electron which will create what's called the holes (absence of electrons) in the lattice, as shown in figure 2.11 a) (see Appendix), resulting in an excess of the positively charged carriers, hence, its name.

The p-type and n-type silicon material is connected to form a pn-junction at their interface. Electrons will naturally diffuse from the n-type region to the p-type, leaving positively charged ions behind them in the n-type region. Likewise, holes will diffuse from the p-type to the n-type region leaving negatively charged ions as illustrated in figure 2.12 (see Appendix).

The region around the interface of the two-type material is called the depletion region due to the depleted charge carriers, this region is neutral (no free charges).

As a result of the depleted charge carriers, an electric field is created across the interface. This built in electric field makes a potential difference which is the barrier potential, it opposes further diffusion of the charge carriers from both sides as shown in figure 2.12 (see Appendix).

The pn-junction diode is created via putting the pn-junction in reverse bias, this is done by applying a positive voltage to the n-region and negative one to the p-region as illustrated in figure 2.11 b) (see Appendix), causing the electrons to move from the n-side to the p-side, hence, increasing the depletion region size.

In this case, very little current will pass through the diode, this current is called the reverse current and its value is extremely small because it results from the flow of the minority charge carriers, that is, the flow of the electrons from p-type material into n-type and the holes from n-type into p-type.

2.3.3 Pixel Detector Detection Principle

The hybrid silicon pixel detector detects the passing charged particle according to this technique:

First, the particle hits the silicon layer generating an electron-hole pair, this electron- hole pair appears as a result of the ionization, that is, when an electron transition from the valence band to the conduction band it leaves a hole in the valence band, keeping in mind that the electron-hole pairs number depend on the energy deposited by the charged particle.

Both the electrons and the holes from the electron-hole pairs can move freely within the silicon lattice but the silicon sensor operates under a bias voltage, this voltage creates an electric field through the silicon material, this electric field is responsible of the acceleration of the electron-hole pair in which, the electrons will move to the n-doped side toward the anode and the holes will move to the p-doped one toward the cathode, inducing current pulses or electrical signals at the pixels where the ionization happens. Those electrical signals are called particle hits and are transferred to the readout electronics layer via the solder bumps.

Knowing where and in which pixels the ionization took place helps us to know where the original particle has passed which allows to reconstruct the particle trajectory as it passed through the pixel detector.

Also a stronger or higher amplitude current signal means a higher number of electron-hole pair which is on its turn directly proportional to the energy deposited by the original particle that caused the ionization.

The induced current which is the reverse current is relatively weak, ranges from (nano-pico) amperes, that’s why it needs to be amplified via amplifiers existed in the readout electronics to be easier to be readout. Also the readout electronics contains analog to digital converters that digitize the signal in order to be readout and analyzed by the computers.

2.4 Track Reconstruction and Momentum Calculation in the ID of ATLAS

2.4.1 Track Reconstruction in the ID of ATLAS

As mentioned previously ATLAS's ID consists of sub-detectors that includes the pixel detector, the SCT and the TRT.

In the same way that was explained previously in subsection 2.3.3 for the pixel detector, the electrical signal resulted from the ionization done to the silicon atoms by the charged particle are used to reconstruct the particle trajectory in the SCT of the ID.

While, in the TRT, the particle trajectory is reconstructed based on the electrical signals resulted from the ionization of the gas mixture existed in its straw tubes.

The charged particle track reconstruction process in the ID includes the following steps which has been used in Run 1, Run 2, and Run 3 phases of the LHC, and are still expected to be used in the ITk but with some optimizations regarding the HL-LHC.

The charged particle track reconstruction process includes the following steps:

1. Hits Formation

The charged particle resulted from the p-p collision in the LHC passes through the layers of the inner detector leaving behind it hits or deposits of energy as a result of the ionization it does to the atoms of the silicon material of the detector, these hits are represented by the pixels or strips in the pixel detector and SCT and they are shown in figure 2.13 a) (see Appendix) in which the yellow points represent the particle hits and the arrows represents the track candidates for the particle. The complete process of hits formation was explained before in subsection 2.3.3.

2. Clusterization

The hits are then grouped together to form what's called clusters, each cluster is formed by associating the nearby hits either in space or time. There are two types of these clusters and they are explained in subsection 3.2.1. Figure 3.3 (see Appendix) shows theses two types.

3. Seed Tracking

The next stage is finding the seeds of track that represents candidates of the initial track which provides the starting point for the whole track reconstruction. This process starts with marking the clusters in the innermost part of the detector that corresponds to the most likely positions where the particle has passed through.

Those seeds are generated from the innermost layers of the detector that are the pixel detector and the SCT, moving outward to continue the full track reconstruction. An example of track candidates for a particle resulted from the p-p collision is illustrated in figure 2.13 a) (see Appendix). This process is called inside out seed tracking and it suits the track reconstruction for the charged particles produced closer to the collision point.

4. Ambiguity Solving

After finding the track candidates, fitting algorithms are applied in order to find the track parameters that gives the best fit, which includes optimizing the parameters such as its azimuthal and polar angles and curvature so that the predicted track and the clustered hits well closely match.

After this, the track candidates will be subjected to ambiguity solving algorithms. Since we are talking about high energy collision, several factors can cause the ambiguity, for example, many charged particles may pass simultaneously through the detector and their paths may intersect or overlap as illustrated in figure 2.13 b) (see Appendix), which leads to an ambiguity in associating the hits to its corresponding correct track.

In addition the readout electronics and sensors might introduce uncertainties or errors in the measurements of the hit positions which could propagate through the track reconstruction process.

These algorithms will help to solve those issues by rejecting fake or lower quality track candidates that share a high number of associated hits with higher quality tracks (shared hits between tracks candidates is a sign of fake tracks) and select the most suitable track candidates based on several quality criteria such as hits number, goodness of fit and consistency with the primary collision point. An example of the high- and low-quality track candidates are shown in figure 2.13 b) (see Appendix).

2.4.2 Momentum Calculation Mechanism in the ID

With its three sub-detectors, ATLAS's ID can measure the momentum of the charged particles resulted from the p-p collision at the LHC.

In the subsection 2.4.1 we showed how the ID can reconstruct the particle's trajectory, this reconstructed track serves as the foundation for the momentum determination.

The ID is submerged in a strong magnetic field created by a superconducting magnet, so the particle path will be influenced by this magnetic field.

when a charged particle enters a uniform magnetic field region with an angle θ between its velocity $\vec{v}$ and the magnetic field $\vec{B}$, it will experience a force called Lorentz force given by:

$$\vec{F} = q\,(\vec{v} \times \vec{B}) \tag{2.1}$$

Where q is the charge of the particle. In this case, the velocity $\vec{v}$ has two components, $v_\perp = v\sin(\theta)$, which its direction is perpendicular with $\vec{B}$ generating the following force component:

$$F_\perp = q\ v_\perp B \tag{2.2}$$

Since the angle between $\vec{v}_\perp$ and $\vec{B}$ is 90°, this force will cause the particle to move in a circular path, but the other component of the velocity is $v_\parallel = v\cos(\theta)$, which its direction is parallel to $\vec{B}$ causing the particle to move in a straight line in the direction of $\vec{B}$, not exerting any force on the particle since the angle between is $\vec{v}_\parallel$ and $\vec{B}$ is zero:

$$F_\parallel = q\ v_\parallel B \sin(0) = 0 \tag{2.3}$$

In conclusion, the combined form of these two particle movements will generate a helical path illustrated in figure 2.14 a) (see Appendix).

In the case of high energy particles, the relativistic effects should be considered. The momentum of a relativistic particle as stated by special relativity is given by:

$$\vec{p} = \frac{mo\,\vec{v}}{\sqrt{1-\frac{v^2}{c^2}}} \tag{2.4}$$

Where m_o is the rest mass of the particle, c is the light speed and $\vec{p}$ is the particle's relativistic momentum. Using the fact that $\vec{F} = \frac{d\vec{p}}{dt}$, we can rewrite equation (2.1) as follows:

$$\frac{d\vec{p}}{dt} = q\,(\vec{v} \times \vec{B}) \tag{2.5}$$

By substituting equation (2.4) in equation (2.5), we get:

$$\frac{d}{dt}\left(\frac{mo\,\vec{v}}{\sqrt{1-\frac{v^2}{c^2}}}\right) = q\,(\vec{v} \times \vec{B}) \tag{2.6}$$

Then by expanding the left-hand side of equation (2.6) we can solve for particle's equation of motion which will involve many algebraic manipulations and vector calculus that is too long to be provided here and can only be solved numerically.
However, the particle's final equation of motion will be a helix equation just like in the classical case.

ATLAS's geometry is described by cylindrical coordinates, as in figure 2.14 a) (see Appendix), the helical path of the charged particle is shown illustrated in it the transverse momentum of the particle (P_T) which is parallel to the direction of the beam line and the longitudinal momentum (P_L). The transverse momentum of the particle given by $P_T = P \sin(\theta)$, can be calculated by integrating equation (2.5) with time t to get:

$$P = q\,B\,R \tag{2.7}$$

Where R is the radius of curvature of the particle's trajectory, then by Substituting P_T in equation (2.7), we will have:

$$P_T = q\,B\,R\,\sin(\theta) \tag{2.8}$$

If the particle charge is known, what's left in order to determine the value of the transverse momentum of the particle, is calculating R.
In figure 2.14 b) (see Appendix), the trajectory of the particle in the magnetic field is illustrated in a blue curve while the particle hits are represented by the green dots. The sagitta of the particle's track (S) is given by:

$$S = R\,(1 - \cos(\alpha)) \tag{2.9}$$

But for small angle α, cos(α) = 1- $\frac{\alpha^2}{2}$, and by substituting this value of the cosine in equation (2.9), we get:

$$S = \frac{R\alpha^2}{2} \tag{2.10}$$

Also, when α is so small, sin(α) = α, so we get:

$$\alpha = \frac{L}{2R} \tag{2.11}$$

Where L is the straight distance between the first hit and the last one. By substituting the value of α from equation (2.11) in equation (2.10) we get:

$$R = \frac{L^2}{8S} \tag{2.12}$$

Now, by substituting the value of R from equation (2.12) into equation (2.8) we will be able to determine the transverse momentum of the particle.

Chapter Three
Upgrades of the ID of ATLAS

3.1 Insertable B-Layer (IBL)

In the LS 1, which started in 2013 and ended in 2015 (58), the LHC needed to be upgraded in order to increase its luminosity, allowing for more precise tests of the Higgs bosons of the Standard Model regarding its properties and interactions (59). The high radiation will cause a lot of failures in ATLAS detector, therefore, its design has to be improved in order to be able to handle it.

The addition of a new pixel layer, the IBL, to the original pixel detector that operated in Run 1 phase of the LHC, was one of the important upgrades that was done to the inner detector of ATLAS during the LS 1. This layer is shown in figure 3.1 a) (see Appendix) and the pixel detector after inserting the IBL layer is shown in figure 3.1 b) (see Appendix).

It was inserted between the vacuum pipe of the LHC and the already existed innermost layer of this pixel detector in May 2014 (4). This addition was possible after the reduction of the LHC beam pipe diameter from 5.8 to 4.7 cm (60).

The basic motivation for this new pixel layer insertion was to maintain and improve the performance of ATLAS detector during the Run 2 operation of the LHC despite the irreversible effects of radiation damage that have taken place in the pixel modules of the detector's layers especially the B-layer.

It also helps to improve the detector's ability to precisely determine the collision point named the primary vertex. As well as, providing much more accurate measurements of the particle track close to the collision or interaction point, which will help to improve the extrapolation of the track projection back to the vertex because of the close position of the IBL to the interaction point, since it surrounds the beam pipe with a radius of 3.3 cm away from it (60).

This precise track measurement is important for detecting bottom quarks and other particles with a short life time that decay very fast. Moreover, with higher luminosity conditions, there is a higher chance that different p-p collisions will occur at the same

time per bunch crossing, so the IBL allows for reducing this increased pile-up effects which on its turn helps to discriminate between tracks originated from different interactions.

- **IBL Pixel Modules**

As illustrated in figure 3.1 a) (see Appendix), the IBL was designed to have a cylindrical geometry and built to surround the new reduced radius LHC beam pipe, it was inserted then in the core of the pixel detector of ATLAS.

This IBL is constructed from 14 staves, where each stave has a length of 64 cm and a width of 2 cm, each one of these staves has its own CO_2 cooling pipe and is populated with 32 pixel modules. Each module on its turn is constructed from a silicon sensor that is bump bonded to FE-I4 chips (61).

This chip type differs from the FE-I3 readout chips that was used in the pixel modules of the pixel detector that operated during the Run 1 phase of the LHC. The main physics goal of producing those chips was basically the higher radiation conditions that the pixel detector must be able to handle during the Run 2 phase of the LHC, including the increase of the integrated luminosity which will result in higher hit rate that the architecture of the FE-I3 read out chip is not qualified to withstand, which will cause degradation of the pixel detector. A comparison between the FE-I3 and FE-I4 readout chips is illustrated in table 3.1.

Table 3.1

Comparison between the FE-I3 and FE-I4 readout chips (61,63)

Parameter	FE-I3 (Before IBL)	FE-I4 (After IBL)
Pixels number	2880 pixels	26880 pixels
Pixel matrix size	18 columns x 160 rows	80 columns x 336 rows
Pixel size	50 x 400 μm^2	50 x 250 μm^2

The reduction of the pixel size improves the data resolution. Each pixel in the chip is divided into two sections, the digital and the analog parts.

The chips is fabricated to withstand a 700 fb^{-1} of integrated luminosity which corresponds to 2.5x 10^6 Gray and more than $5x10^{15}$ n_{eq}/cm^2 fluence (64).

Two different technologies were used in building the sensors used in the pixel modules in the IBL, the planar silicon sensors already used in the rest of the layers of the pixel detector and a new 3D pixel sensor technology (63).

The difference between the planar and the 3D sensors is that, the two p-doped and n-doped electrodes are implemented perpendicularly in the silicon bulk in the 3D sensors whereas in the planar sensors, the electrodes are attached to the bulk surface as illustrated in figure 3.2 (see Appendix) (65). The advantages of this technique is that the design of 3D sensors allow for faster signals due to the higher charge collection rate thanks to the shorter distance between the electrodes compared to the planer sensors since in planar sensors, the distance between the electrodes is represented by the sensor thickness itself which is not the case in 3D sensors as shown in figure 3.2 (see Appendix). In addition, the needed bias voltages to get the same electric field will be less because it depends on the distance between the electrodes which is less in 3D sensors (65, 66).

The planar sensors has a thickness of 200 µm whereas, the 3D sensors has a 230 µm thickness. Both sensor types were intended to operate at over $5x10^{15}$ n_{eq}/cm^2 fluence (67).

The pixel module used in the IBL is constructed from a bare module that is basically made up from the FE-I4 readout chip which is bump bonded to the silicon sensor. This bare module is glued on its turn to a flex PCB in order to provide the needed electrical contact. The modules are then fixed on the staves.

Just 25% of the modules used in the IBL will 3D sensor modules while the rest which is 75% will be planar sensor modules. The choice of this percentage and the choice of where exactly each sensor type is used is based on a balance between the sensor performance and cost.

In May 2015, the Run 2 phase of the LHC has officially started and the data taking begun again after around three years of shutdown. The insertion of the IBL has shown its success and reached the expected performance with a high tracking capability, low number of dead modules and high efficiency (67).

The main and crucial achievements that resulted from inserting the IBL into the pixel detector, is that all the FE-I4 readout chips along with all the sensors was kept fully

operational during the whole Run 2 phase, allowing an excellent and complete tracking performance (67).

The IBL community is now working on producing pixel modules with both planar and 3D technologies that is suitable to cope with the high luminosity upgrading plan of the detector.

3.2 The New ATLAS Inner Tracker (ITk)

After inserting the IBL layer, the pixel detector increased the ID ability to cope with the increased luminosity and radiation dose during the Run 2 phase and Run 3 phase which is still not finished yet (22). However, this ID will not be able to survive the HL-LHC era because of the unprecedented high luminosity values that will be reached as was explained previously in chapter one. For this reason, a new all-silicon harder radiation ITk will totally replace the current ID after Run 3 phase (68-70).

This replacement aims to maintain and increase the ID performance in the intense particle environment of the HL-LHC and be able to handle higher occupancies, data rates and radiation doses that would damage the current sensors and degrade the detectors if they don't undergo the needed upgrade that will be explained later.

3.2.1 Challenges of Tracking in the Dense Environment of the ITk

The harsh environment of the HL-LHC will be a challenge to the ITk design, since it must be able to handle the increasing luminosity and radiation fleunce. Here is some challenges that the ITk must handle:

- With a 14 TeV collision energy, 200 p-p collisions per bunch crossing are expected (71). This very high energy leads to higher P_T and with higher P_T, the overlapping possibility between the tracks of the particles would increase since the separation between them will be reduced and the particle tracks will be more collimated as can be seen in the top part of figure 3.3 (see Appendix) (72). So, there will be a higher number of merged particle hits which would negatively affect the precision and efficiency of track reconstruction (71).
- In a normal particle environment, not very dense, the energy deposits of a specific particle passing within the silicon sensor material grouped together to form a cluster, hence we call it a single- particle cluster. However, in the dense particle environment

expected to take place at the HL-LHC era, the P_T of the particles will increase, which will cause the trajectories of different particles to collimate closer to each other (72). As a result of this process, the energy deposits of various particles will be grouped next to each other forming what's called a merged clusters. Both the single-particle and the merged clusters are shown in the bottom part of figure 3.3 (see Appendix).

3.2.2 Design of ATLAS ITk

The current ID of ATLAS is designed to reconstruct the charged particle tracks with a coverage up to $|\eta| < 2.5$, whereas, in the ITk, the coverage will be extended up to $|\eta| < 4$ (73).

The ITk is one of the most important upgrades of the ATLAS detector that will be carried out at the start of the HL-LHC era. This new ITk will allow ATLAS detector to measure 4000 fb^{-1} data (74), thus, increasing the detector capability of revealing new physics that might be hidden within the rare processes.

Throughout the HL-LHC period, ATLAS detector will face an increase of seven times its instantaneous luminosity, it will also see 200 interactions compared to around 50 interactions per bunch crossing (30). Those operating conditions surpass the current ID capabilities and would result in a direct destruction and degrade of the detector as mentioned previously. Therefore, the ITk is designed to bear these conditions and operate efficiently during the HL-LHC.

The ITk will have a cylindrical geometry covering an area of about 180 m^2 and having over $5x10^9$ readout channels compared to the currently installed ID that has an area of around 63 m^2 and around $1x10^8$ readout channels (73).

The chosen design for the ITk of ATLAS detector will be made up of two sub-systems, the pixel detector which lies in the innermost region of the detector and is explained in detail later in section 3.3 and the strip detector, located in the ITk's outermost layer surrounding the pixel detector and is detailed later in this section.

Both of these detector systems are immersed in a 2 T magnetic field just like the current ID (75). The ITk schematic layout is illustrated in figure 3.4 (see Appendix) in which the pixel detector active elements are illustrated in red lines where the active elements of the

barrels part are shown in light red and those of the end-caps part in dark red. The strip detector active elements are illustrated with blue lines where the active elements of the barrel's layers are shown in light blue and those of the end-caps disks in dark blue. The z-axis represents the axis of the LHC beam line where the point (0,0) is the interaction point and the y-axis represents the measured radius from this interaction point.

The design will be a lot more complex compared to the current ID design, since it will feature ten times the strip channels number and sixty times the pixel channels number in comparison with channels number of the present ID Which is mentioned in table 3.2. The design of the ITk of ATLAS is illustrated in figure 3.5 (see Appendix) in which the pixel detector is shown inside the yellow region and the remaining area outside the yellow region represents the strip detector .

The basic building unit of the ITk is the module, consisting of readout electronics and sensors. This ITk will have a number of modules equals to five times the number in the current ID. Additionally, the surface of each pixel detector module and strip detector module will be around three times and five times larger than that of the currently existed ID respectively.

Both the strip and the pixel detectors are mounted onto structures of local support, forming a cylindrical layer's system in the central part of the detector called the barrel layers and a rings system at the two end sides of the detector, called the end-cap rings as illustrated in figure 3.5 (see Appendix).

Some major differences between the ID and the new ITk of ATLAS experiment are listed in table 3.2.

Table 3.2

Comparison between the current ID and the new ITk of ATLAS detector (68, 73, 76)

Parameter	ID	ITk
Composition	Partially-Silicon Tracker composed of 3 Layers (SCT,TRT and Pixel detector)	All-Silicon Tracker composed of 2 layers (Strip and pixel detector)
pseudo-rapidity (η)	Covers up to $\|\eta\| < 2.5$	Covers up to $\|\eta\| < 4$
Number of Readout Channels	$1x10^8$	$5x10^9$

- **ITk Strip Detector**

The strip detector of the ITk of ATLAS which surrounds the pixel detector is composed from four barrel layers, L_0, L_1, L_2 and L_3 together with six disks on each end side of the barrels, R_0, R_1, R_2, R_3, R_4 and R_5 (77). Both the barrel and the end-cap regions are shown in figure 3.6 a) (see Appendix).

Each disk is composed of 32 petals where each petal carries the strip modules which on its turn are organized in six rings as illustrated in figure 3.6 b) (see Appendix) that shows a petal illustrated in it parts from the six rings that holds the modules. As a result, the whole number of petals required for the two end-cap regions in the strip detector is 384 petals. In the barrel part, 392 rectangular staves are used as the support structure (78), each stave holds 28 strip modules in which 14 modules is used at each side of the stave (76).

A. Strip Modules

The strip modules are the fundamental building block of the strip detector where it will be contain 18000 strip modules (76).

The two innermost barrel layers of detector are equipped with short strip modules while the two remaining outer layers contains long strip modules (78). The layout of the short strip module is shown in figure 3.7 (see Appendix).

Both the long strip and short strip sensors existed in the modules that used in the barrel region of the detector have a rectangular shape and the orientation of the strips in this region runs towards the LHC beam line direction.

Regarding the disks part of the detector, the sensors are glued to the modules existed in strips that lies vertically to the beam line and six different shapes of sensors are used in this region.

Each module is composed of hybrids which is a flex PCB that houses the FE readout chips, a silicon sensor and power-boards that are glued directly on the sensor surface (78). The power-boards and the hybrids number in each strip module depends on the type of the module. Modules existed in the barrel layers region can have two or one hybrids and just one power-board while in the end-cap region, the number of hybrids in the strip

module ranges from one to four while the number of power-boards can be one or two. Those hybrids are powered via the power-boards that consist on its turn of a DC-DC converters which guarantees that the hybrids will be powered by the required steady output voltage (78).

B. Sensors

In general, the strip detector of the ITk is populated with sensors that have a thickness of 320 μm (78).

In the barrel region of the detector, a rectangular-shaped sensors are used. These sensors have a size of 97.95 x 97.62 mm^2. The sensor used in the two innermost barrel layers of the strip detector is sectioned to four segments where each one has a length of 24.12 mm. In the two remained outer layers, each sensor is divided into two sections and each one of these sections is a 48.305 mm long. On the other hand, in the disks region, six geometrical shapes are used (78).

In general, this strip detector of the ITk is expected to withstand a radiation dose of $1.6x10^{15}$ n_{eq}/cm^2 in order to get a 4000 fb^{-1} of integrated luminosity, which makes the testing of the sensor performance at the end of the life time a crucial task (79).

3.3 ITk Pixel Detector

The pixel detector which is the vertex detector for ATLAS experiment faces the largest amount of particle flux as a result of its very close distance to the beam pipe of the LHC, corresponding to the highest hit occupancies and radiation damage in ATLAS, which leads to unprecedented requirements for reading out speeds and radiation hardness (56).

3.3.1 Design of the ITk Pixel Detector

The system will be composed of three parts which are mechanically independent. The inner system, the outer barrel system and the outer end-caps part. The layout of the pixel detector of the ITk is illustrated in figure 3.5 (see Appendix).

The radius of the ITk will extend 33 mm a way from the LHC beam pipe to 400 mm (76). It will cover up a pseudo-rapidity of $|\eta| < 4$ while at the same time multiple scattering will be minimized by greatly reducing the material budget compared to the current ID (80).

1. Inner System

The inner system of the ITk's pixel detector is the closest part to the beam pipe of the LHC, where its innermost layer is placed at a distance of 34 mm away from the LHC beam pipe. It has two barrel staves layers which are the L_0 and L_1 layers, together with a number of end-caps rings. There are three different designs for the end-cap rings which are R_0, $R_{0.5}$ and R_1 rings (73, 81). These three designs are shown in figure 3.8 a) (see Appendix).

The $R_{0.5}$ ring is located in between the R_0 and R_1 layers and each one of these rings is constructed from two half rings with a core of carbon that contains electrical and cooling services. Services that includes, data transmission and cooling will be carried out by the outer shell (81).

Two types of pixel modules are used which are the quad and triplet modules that are both explained later in detail in subsection 3.3.2, those modules are mounted on the staves and rings via gluing them (81).

The L_0 and L_1 layers are planned to be extracted after 2000 fb^{-1}, because the detector modules performance is expected to get degraded as a side effect of the high radiation (73). The reason of extracting the inner systems only is because of its close distance to the beam pipe, hence it will experience the highest amount of radiation compared to the outer system.

The assembly of this system is done using integrating quarters and one of these quarters is shown in figure 3.8 b) (see Appendix) in which the quarter holds part of the rings and the two barrel layers of the system. Those quarter shells have two layer barrel staves to build the L_0 and L_1 layers and a number of rings.The rings and staves are considered as structures for local support in where the modules are mounted (81).

2. Outer Barrel System

The outer system of the ITk's pixel detector differs a little bit from the inner system. Here, the system spans the central region of the ITk detector at larger radii than the inner system and its planned to stay till the end of the HL-LHC period.

It is composed of three barrel layers which are the L_2, L_3 and L_4 layers. Each barrel layer is constructed from two sections. The first section is represented by the two ends of the barrel and its local support structure are half inclined rings (they are inclined with respect to the beam line axis) while the support structure in the second section which is the central region of the barrel are flat staves. The flat staves used in the barrel region of this system are called longerons (81). Those two local supports are illustrated in figure 3.9 (see Appendix). From the left to the right side of figure 3.9 (see Appendix), the module cells are glued on the basblocks for cooling purposes. Then, those base-blocks are screwed onto the outer barrel local supports which on its turn can be inclined rings or longerons. The support structures are assembled then into the half barrel as illustrated on the right side of the figure.

The reason of using inclined rings in the ends part and flat staves in the central region is because, in the central region, most of the particles resulted from the p-p collision traverse the detector layers in a perpendicular direction with respect to the beam line, while in the end parts region most of the particles tend to travel in angles as illustrated in picture figure 3.10 (see Appendix).

The inclined rings in the end parts would help to capture a higher number of particles traversing this region compared to flat staves which would improve the detector efficiency.

3. Outer End-caps

The outer end-caps part is made up of three sets of rings on each side of the outer barrel . The local support structures are sets of two-sided half rings with three different sizes that are made of carbon with a titanium tube embedded within it (81) as shown in figure 3.11 a) (see Appendix).

The half rings of each size are assembled together to construct a half barrel that is illustrated in figure 3.11 b) (see Appendix). As a result there will be three different sized half barrels. By assembling the half barrels together, we will have three barrels or end-caps on each side of the outer system as shown in figure 3.11 b) (see Appendix) that illustrates the whole layout of one of the end-caps (73, 81). Also the pixel modules is mounted on both the two sides of the half rings.

A comparison between the pixel detector of the current ID of the ATLAS detector and the new ITk pixel detector of ATLAS detector is illustrated in table 3.3.

Table 3.3

Comparison between the pixel detector of the ID and the new ITk of ATLAS detector (45,82)

Parameter	Pixel Detector of the ID	Pixel Detector of ITk
Number of Layers	Four pixel layers	Five pixel layers
Number of readout channels	9.2×10^7	5×10^9
Surface area of the pixel system	1.7 m^2	13 m^2

3.3.2 ITk Pixel Modules

The pixel detector will be made up of around 10000 modules with five billion readout channels (80), covering a 13 m^2 of the ITk's total area compared to an area of 1.7 m^2 that the current pixel detector have (82).

The building block of the pixel detector are the pixel modules, which on its turn are composed of silicon sensors and readout chips. Those readout chips are attached to the sensors via bump bonding and those three layers of the pixel module are shown in figure 3.12 a) (see Appendix). The assembly are glued then to a flex PCB in order to form the pixel module. The module fabrication technique is illustrated in detail later in subsection 4.1.1.

Two types of pixel modules are planned for the ITk which are the triplet and quad modules (73, 80, 81):

A. The triplet pixel module: this module type is made up of three FE chips bump bonded to a high resistivity 3D silicon sensor, then this assembly is glued on a flex PCB, this kind of modules is populated in the innermost layer of the pixel detector, L_0 (73, 83).

B. The quad pixel module: it is composed of four FE chips bump bonded to a planar sensor. This module type instruments the rest of the layers, from L_1 to L_4 (73, 83).

Both the triplet and quad modules are illustrated in figure 3.12 b) and c) (see Appendix).

- **Pixel Sensors**

Different pixel dimensions and technologies are used in the ITk's sensors. In general planar and 3D sensors are employed within the ITk layers (73). Those sensor technologies

are not brand new, they has been already used in the IBL as mentioned before in section 3.1. However, they are now undergoing a number of modifications and improvements in order to be suitable for using it in the innermost layer of the ITk pixel detector.

1. Planar Sensors

A comparison between the planar sensors used in the IBL of the current pixel detector and the planar sensors used in the pixel detector of the ITk is shown in table 3.4.

Table 3.4

Comparison between the ITk and the IBL planar sensors (57,67,73)

Parameter	ITk planar sensors	IBL planar sensors
Sensor thickness	150 μm in the outer barrel system and the outer end-caps and 100 μm in the inner system	200 μm
Pixel matrix size	18 columns x 160 rows	80 columns x 336 rows
Pixel size	50 x 50 μm^2	50 x 250 μm^2

The less thick sensors are used in the inner layers in order to achieve the optimal detection performance regarding the power dissipation due to the confined available space for the cooling tubes.

Sensors existed in the outer system layers have to handle high values of particle fluence. However,the sensors presented in the inner layer L_1 have to withstand stricter conditions regarding radiation hardness as a result of their closer distance from the LHC beam pipe in where the p-p collision occur.

The two planar sensors of thicknesses 100 μm and 150 μm has shown a hit efficiency higher than 98% with 400 V and 600 V bias voltages respectively, after being subjected to a $5x10^{15}$ n_{eq}/cm^2 of particle fluence (73).

- **3D Sensors**

The 3D sensors in the pixel detector of the ITk have a smaller pixel size compared to that of the 3D sensors that was used in the IBL. The size of the pixels in the barrel layer L_0 is 25 x 100 μm^2 and in the disks part is 25 x 100 μm^2 compared to a 50 x 250 μm^2 size used

in the IBL (57, 73). This smaller pixel size help to improve the resolution and minimize the ambiguity in track reconstruction.

Also, those sensors have a thinner substrate with respected to the thickness of the IBL's 3D sensors. The active thickness is decreased here to 150 µm in comparison to 230 µm in the IBL (67, 80).

This 3D sensors that were developed for the ITk have shown exceptional radiation hardness, reaching over $1.6x10^{16}$ n_{eq}/cm^2 of particle fluence by obtaining a hit efficiency over 96% with a 150 V bias voltage, which is the values needed in the innermost layer of the ITk (73).

Hence, the reason of using it in the innermost layer of the ITk pixel detector which lies just 33 mm away from the LHC beam pipe is actually the ability it showed to withstand high radiation tolerant which on its turn refers to the way it was fabricated as explained previously.

The 3D sensor is expected to be replaced after 2000 fb^{-1} data collection as a part of the replacement of the inner system of the pixel detector that was mentioned previously (77).

3.3.3 ITkPix-V1 Readout Chip

The previous FE readout chips that were used in the pixel detector of ATLAS, which is the FE-I3 and FE-I4 readout chips were designed and produced by the Development and Research 53 collaboration (RD53) which is one of the research and development collaborations in CERN consisting of 24 organizations from both United states and Europe. The main goal of the this collaboration is to produce the designs and tools that will help developing the pixel readout chips required for both CMS and ATLAS detectors at the HL-LHC (84).

The design of the FE readout chip that is used in the ITk of ATLAS was developed by the same collaboration under the name RD53B. The real fabricated chip of this design for ATLAS was produced under the name ITkPix-V1 chip. It was fabricated using a new 65 nm CMOS technology (85) and evolved from the RD53A prototype which was developed by the same collaboration for ATLAS experiment. Figure 3.13 (see Appendix) shows both the prototype chip RD53A and the RD53B chip.

A Comparison between the ITkPix-V1 chip and the RD53A prototype chip is shown in table 3.5.

Table 3.5

Comparison between the ITkPix-V1 chip and the prototype chip RD53A (84,87)

Comparasion parameter	RD53B-ATLAS (ITkPix-V1)	RD53A
Chip Size	20 x 21 mm^2	20 x 11.5 mm^2
Pixel matrix size	400 columns x 384 rows	400 columns x 192 rows
Pixel size	50 x 50 μm^2	50 x 50 μm^2

- **ITkPix-V1 Chip Floorplan**

The ITkPix-V1 chip is composed of two regions:

1. Chip bottom region: this region carries all the functionality of the system together with the wire bonding pads of the chip. Also, the size of this region is fixed and doesn't depend on the size of the matrix (86).
2. Pixel matrix region: the pixel matrix is constructed from similar 8 x 8 pixel cores organized in 48 rows and 50 columns. The 64 pixels existed in each core are organized in 16 assembles called analog islands, where each island is made up of 4 pixels as illustrated on the top part of figure 3.14 a) (see Appendix). The islands are incorporated in a flat digital sea, where the islands appears in blue and the digital sea is shown in black as shown in the figure 3.14 a) (see Appendix) (86). Also, each core has a size of 400 x 400 μm^2.

A real physical chip cannot have a width smaller than 20 mm which accounts for 50 cores as illustrated in figure 3.14 b) (see Appendix) since that is the width of the frame of the wire bonding pad for this chip. However, it can be wider than this value. On the other hand, the height of the chip is constrained to a maximum number of 50 rows of cores due to the required readout timing and power (86).

Regarding the bottom part of the chip, there is two bottom parts:

a. Analog chip bottom: it contains sensors that provide the correct values of voltages and frequencies required for operation to the digital logic. In addition to the power regulators that helps to maintain and ensure a stable voltage supply to different parts of the chip (88).

b. Digital chip bottom: this chip bottom works to assemble the digital data from the pixel matrix It also responsible for chip control. Moreover, it decodes and encodes the information sent to and from the chip (88).

In general, both the analog and digital chip bottoms works together to monitor, readout and configure the chip. Both of them are shown on the bottom part of figure 3.14 a) (see Appendix).

This ITkPix-V1 readout chip is going now under many tests that will be explained in subsection 4.1.2.

Chapter Four
Wafer Probing Tests

4.1 Module Fabrication and Testing

4.1.1 Module Fabrication

Hybrid pixel modules are produced via bump bonding the silicon sensors to the readout chips to form the bare modules that are illustrated in figure 4.1 a) (see Appendix). This bare module is glued then to a flex PCB (89).

The module assembly process is done using a specific tooling illustrated on the left side of figure 4.1 b) (see Appendix). This tool comprises two jigs to carry the bare module and the flex via vacuum suction as illustrated figure 4.1 b) (see Appendix). Those jigs contain dowel pins that ensure a correct alignment of the components. It helps stacking them on top of each other with a precision of ∓ 50 µm (90).

Using a stencil tool consisting of a stencil sheet and stencil frame illustrated in figure 4.1 b) (see Appendix) in which the left side of the figure shows the tool used to assemble the module, this tool is made up of two jigs, the first jig holds the bare module and the second one holds the flex PCB, it also has screws used to adjust the distance between the jigs while the right side of the figure illustrates the process of applying the glue onto the stencil sheet in order to transfer it to the flex PCB. An amount of glue is spread on the sheet that will be put on the flex to transfer the glue then it will be taken away and the two jigs will be attached to each other. The height of the glue can be controlled by adjusting the distance between the two jigs using screws exists on the tool. The height of the glue is specified to be 40 ∓ 15 µm (90).

A parylene coating is applied to the wire bonds area of the module in order to give a High voltage (HV) protection and protect it from moisture, contamination and any expected physical stress that may cause destruction.

Also, a tape is stuck to the module backside and the connector area of the module in addition to a protective cover before the coating process in order to make sure that the parylene coating covers the intended area only which is the bonding wires area.

4.1.2 Module Testing

In order to build operating modules, its components should be tested carefully, that is, the silicon sensor, the flex and the readout chips must all be declared as functioning before starting the fabrication steps explained above.

Regarding the readout chips, the performance is examined through laboratory tests that includes electrical and visual tests.

The visual testing is performed by eye using a camera or microscope and includes checking for defects or debris on the chip surface because it might be a reason for possible failures that may happen in the tests that will be performed later. Also, the wire bonds status is checked simply by looking through the microscope for any improperly bonded wires since they all should be in a straight line without touching each other.

Electrical tests on the chips, including current-voltage characterization are performed in a controlled environment regarding the temperature and relative humidity. The current-voltage tests is performed at 20 ℃ and at relative humidity below 50％ (90). One of the set-ups used for the electrical testing is a semi-automatic probe station that is shown in figure 4.2 a). This set up is used for doing wafer probing tests on the readout chips that is used to build up the modules.

Wafer probing is basically an electrical testing process that is performed on readout chips to test their electrical properties such as its voltage and current.

4.2 Overview and Objective

This thesis is about the analysis done to the results of the wafer probing measurements that were performed in IJCLab on the ITkPix-V1 chips that I talked about previously in subsection 3.3.3.

Since ATLAS's inner detector will be upgraded to operate during the HL-LHC by replacing it with the new ITk, the chips used in the modules of the ITk pixel detector should be suitable for this upgrade.

For this reason, all the produced ITkPix-V1 readout chips should go under a quality control process which includes performing wafer probing tests on these chips to decide which ones are suitable to build up the module for the ITk.

However, before doing this, all the ITk pixel groups that will contribute to this task have to qualify its wafer probing set-up performance to do the tests on the chips.

The IJCLab ATLAS ITk pixel group is one of these groups and its now working to qualify its wafer set-up by performing wafer probing tests on the ITkPix-V1 chips.

The main goal of this thesis is to help analyzing the results of this wafer probing tests that was done using the wafer probing set-up in IJCLab and comparing it with reference measurements that were done on the same ITkPix-V1 chips by the University of Bonn in order to qualify the IJCLab set-up for doing the tests.

4.3 Wafer Probing Set-up

The ITkPix-V1 chips are delivered to the IJCLab in the shape of wafers of 132 chips each, the ITkPix-V1 wafer is shown on the left side of figure 4.3 a). We do the wafer probing tests on this wafer before dicing it to individual chips. The process of how exactly the wafer probing tests is done is clarified in section 4.4.

The wafer probing tests are done on the chips in IJCLab in a clean room using a semi-automatic probe station named Signatone WL350 with a Board for Data Acquisition (BDAQ53) that has been developed by the University of Bonn. The wafer probing set-up is shown in figure 4.2 a) and the BDAQ53 board is shown on the right side of figure 4.3 a).

The set-up scheme is shown in figure 4.2 b). On the leftmost of the figure, there is the data acquisition PC that controls the measurements through a python software which sends and receives signals from the probe station, power supplies, BDAQ53 and the probe card, so it actually controls all devices in the experiment.

Regarding the functionality of the chip its evaluated the BDAQ53, which is on its turn linked to the probe card through the display port cables illustrated by green lines in figure 4.2 b), in order to transfer the received data of the chip to the PC through a RJ45 connector illustrated by a blue line in figure 4.2 b). So the BDAQ53 makes the communication

between the readout chip and the python software on the PC. The electrical connection to the readout chips is achieved via the probe card that has around 200 tungsten probes makes a temporary contact with the wire bond pads of the chips. This probe card is shown in figure 4.3 b).

Figure 4.2

Wafer probing set-up: a) components of the wafer probing set-up, b) scheme of the BDAQ53 wafer probing system for the ITkPix-V1 chip

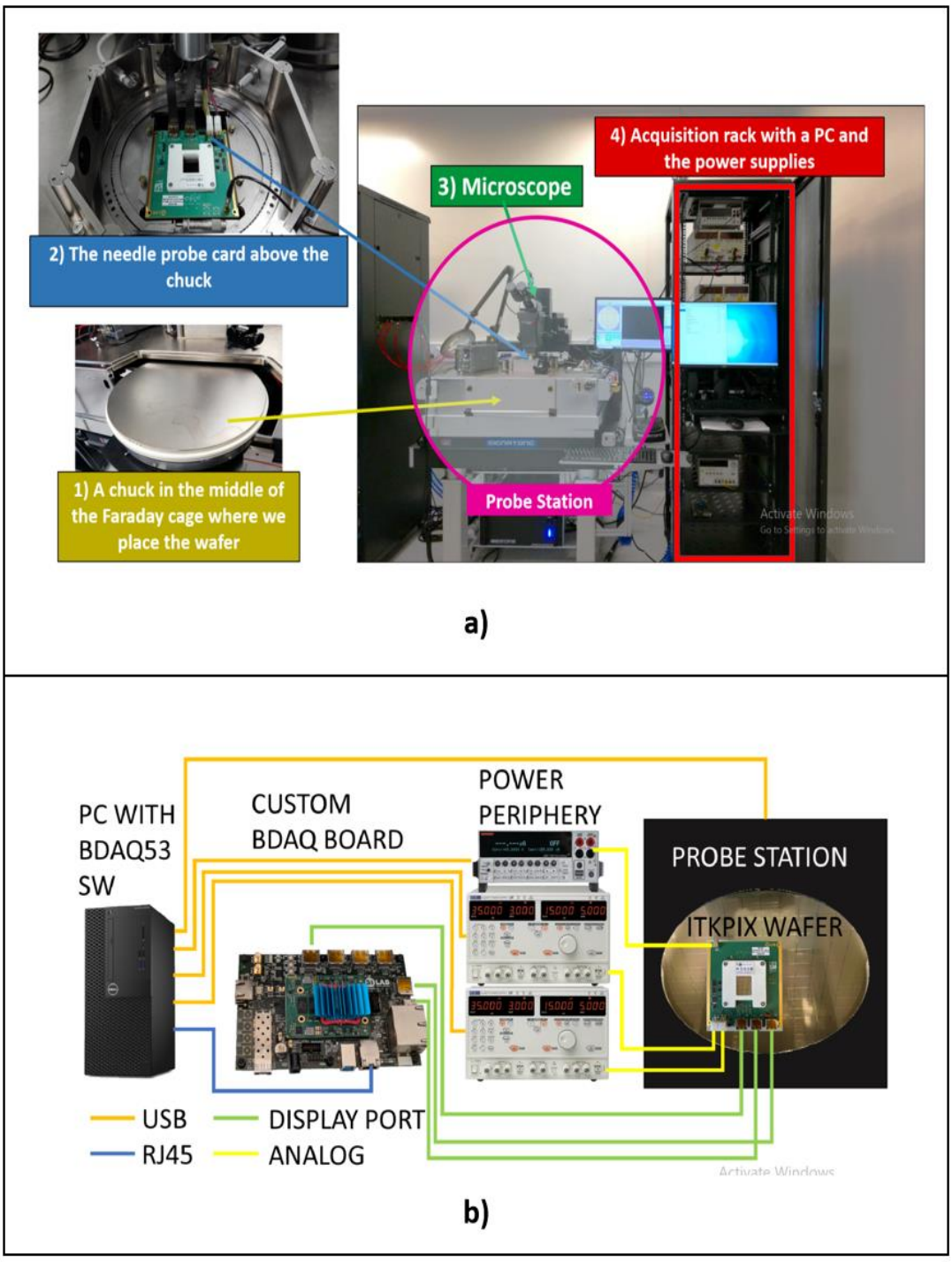

Regarding the power supplies, they give power to the probe card through two MOLEX connectors and the acquired chip data (current and voltage) are sent to the data acquisition PC through a LEMO connector.

4.4 Wafer Probing Methodology

The whole wafer is checked on the probe station before dicing it into individual chips. The checking process is done via the following steps:

1. The wafer is installed on the chuck. The wafer will not move after installing it on the chuck due to the fact that there are vacuum suction holes on the chuck that works to hold the wafer in place. Then the probe card is fixed above the wafer. To ensure that the probes correctly touch all pads of the chip, we check the planarity of the chuck and of the probe card and we align the wafer and the probes. The chuck planarity is adjusted using two knobs as shown in figure 4.4 (see Appendix).

2. The chuck is lifted carefully until electrical contact between the probes and the pads is done. The lifting process is done while simultaneously monitoring it under the microscope via a screen that shows the view under the microscope. The screen is shown in figure 4.2 a) directly next to the acquisition rack. To make sure that the electrical contact is achieved, a red light appears when the rightmost and leftmost probes touch the wafer.

3. The python script in the PC launches several tests on the analog and digital parts of a chip. When the test is finished the probe station moves automatically to the next chip and so on. A complete test of the whole wafer takes 48 hours to finish, that is, 20 minutes per chip. Figure 4.3 c) shows a picture under the microscope for the needle prints on the chips pads that resulted from the electrical contact that is made between the probe needles when they touch the chips surface.

4. The test results are analyzed via the python script on the PC, and they are summarized in (Excel, CSV, YAML, etc…) files. Also, an output yield map of the wafer is resulted as a part of the analysis, this yield map collects the results and shows the bad and good operating chips. For example, a yield map for the 48-hour test that was done on the ITkPix-V1 wafer by Bonn is shown in figure 4.5 (see Appendix). It shows the good operating chips in green, the bad operating one in red, and chips that operates in specific conditions in yellow.

For the chip to be operating good, all its control tests must be succeed, for example, the ground voltage must be low and all the measured input voltages must be as close as possible to the voltages injected to the chip.

In the analysis in this thesis, the chip is good if its measurements were close to the reference measurements and bad if its not. From now on, I will be using the phrase “good chip” to refer to the chip in which its data is close to the reference data and the “bad chip” phrase to refer to the chip that its data is very far from the reference one.

Figure 4.3

a) The ITkPix-V1 wafer and BDAQ53 board. b) The probe card and the probe needles under the microscope. c) The needle prints on the ITkpix-V1 chip pads under the microscope

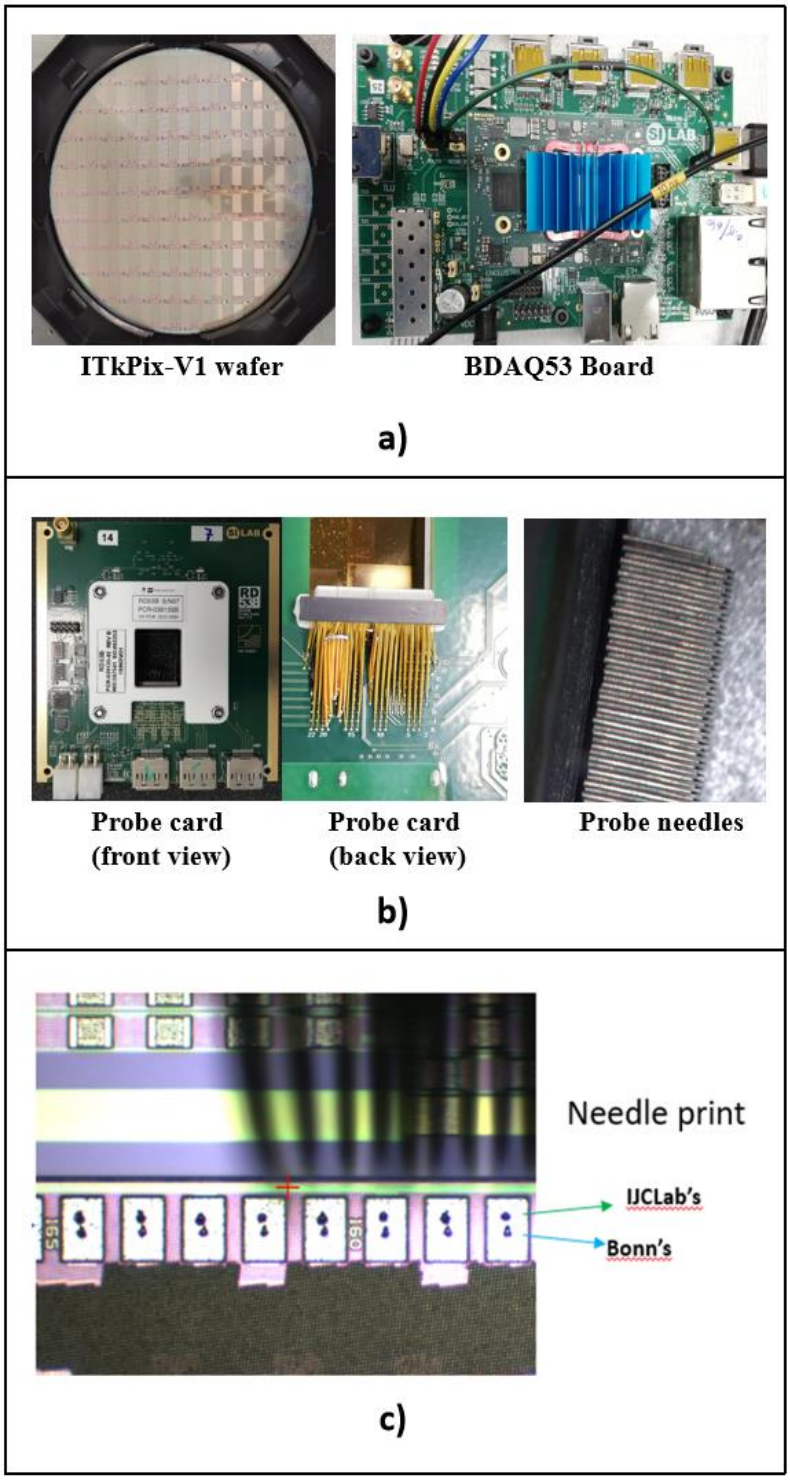

Chapter Five
Discussion and Conclusion

5.1 Discussion of the Wafer Probing Tests Results

5.1.1 Analysis of the IJCLab 48-hour Test Results

For the ITkPix-V1 wafer that was already tested by Bonn, we did another 48-hour test to qualify the performance of our set-up. Part of the results of the test were similar to the reference results while some parameters were not. The most important parameters were analyzed and studied which are, the Voltage Input for Analog regulator (VIN_A), Voltage Input for Digital regulator (VIN_D), Analog Ground (GNDA) and Digital ground (GNDD).

In particular, for the VIN_A and VIN_D parameters, we measure a voltage drop. This voltage drop problem means that there was a big difference between the measured voltages and the injected voltage values.

Regarding the GNDA and GNDD parameters, their values were high compared to the reference values. These two problems are discussed in detail later in this section.

To do the analysis, I built python codes that helped to do further analysis for the results, these codes are totally separated from the python script used in the PC of the experiment. They were built to investigate the two problems mentioned above.

The data that I worked on came in YAML format in which each chip's data existed in a separate YAML file. each YAML file contains all the data of the chip but we are interested only in the IV curves part of the file that is shown in figure 5.1 (see Appendix), especially the four previously mentioned parameters, VIN_A, VIN_D, GNDA and GNDD.

- **Comparison between IJCLab and Reference Results Using Histograms**

In figure 5.1 (see Appendix), there are five injected voltage values under the IV curves, which are, 1.5 V, 1.6 V, 1.7 V, 1.8 V and 1.9 V. For each one of these voltages there are a list of parameters values that includes the four parameters of our interest which are VIN_A, VIN_D, GNDA and GNDD.

Histograms of these four parameters for the injected voltage value 1.6 V were plotted in figure 5.2 a) in which each one of the four graphs has two histograms, one for the reference measurements in green and the other one is for IJCLab measurements in red to make the comparison between the two measurements easie.

It was noticed that the VIN_A and VIN_D parameters have a quite larger distribution with a smaller mean value compared to the distribution and mean value of the reference data, this smaller mean value ensures the voltages drop problem.

On the other hand, the GNDA and GNDD have a large distribution with a larger mean value than the reference ground voltage data, which is not good since having a large ground value may mean that we have a large background noise or fluctuations in the measurements, which would negatively impacts the measurements reliability and accuracy. In a well constructed and correctly grounded electrical systems, we should have a stable and low ground reference.

After that, the same exact histograms for VIN_A and VIN_D but after subtracting the corresponding ground values, GNDA and GNDD respectively were built which are both illustrated in figure 5.2 b). This is done in order to remove the ground noise.

When the ground value was subtracted, the distribution becomes larger which corresponds a higher standard deviation that indicates larger dispersion of the data from the mean value. Also, the mean value becomes even smaller meaning that the voltage drop now is greater, which is not good because obviously the mean value should be as close as possible to the reference voltage value.

Figure 5.2

IJCLab's and Bonns's histograms for the injected voltage value 1.6V of the parameters a) (VIN_A, VIN_D, GNDA, GNDD) and b) (VIN_A - GNDA) and (VIND - GNDD)

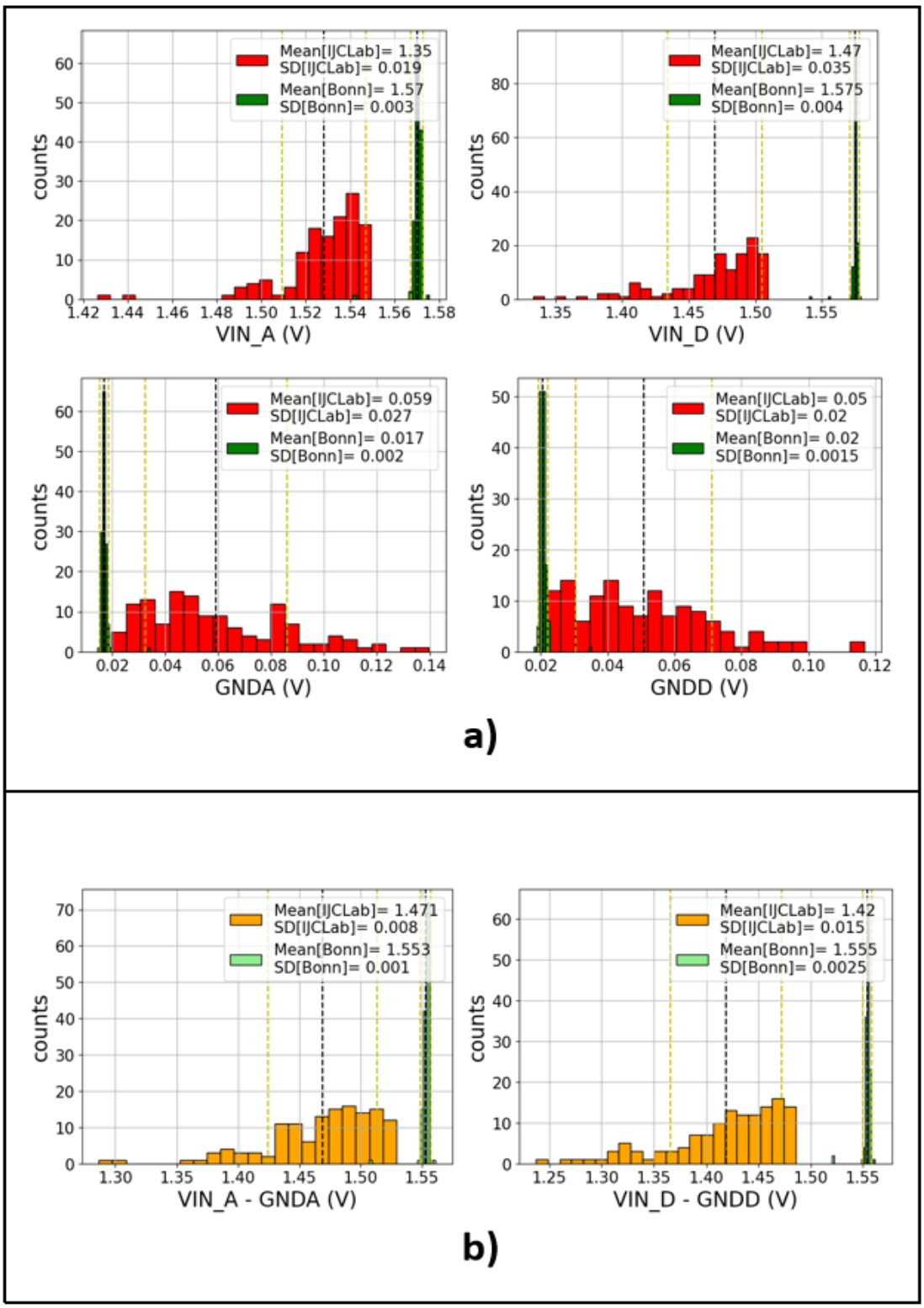

Figure 5.3

Two error bars Plots of the mean values of the (VIN_A, VIN_D) and (GNDA, GNDD) parameters versus their corresponding injected voltages

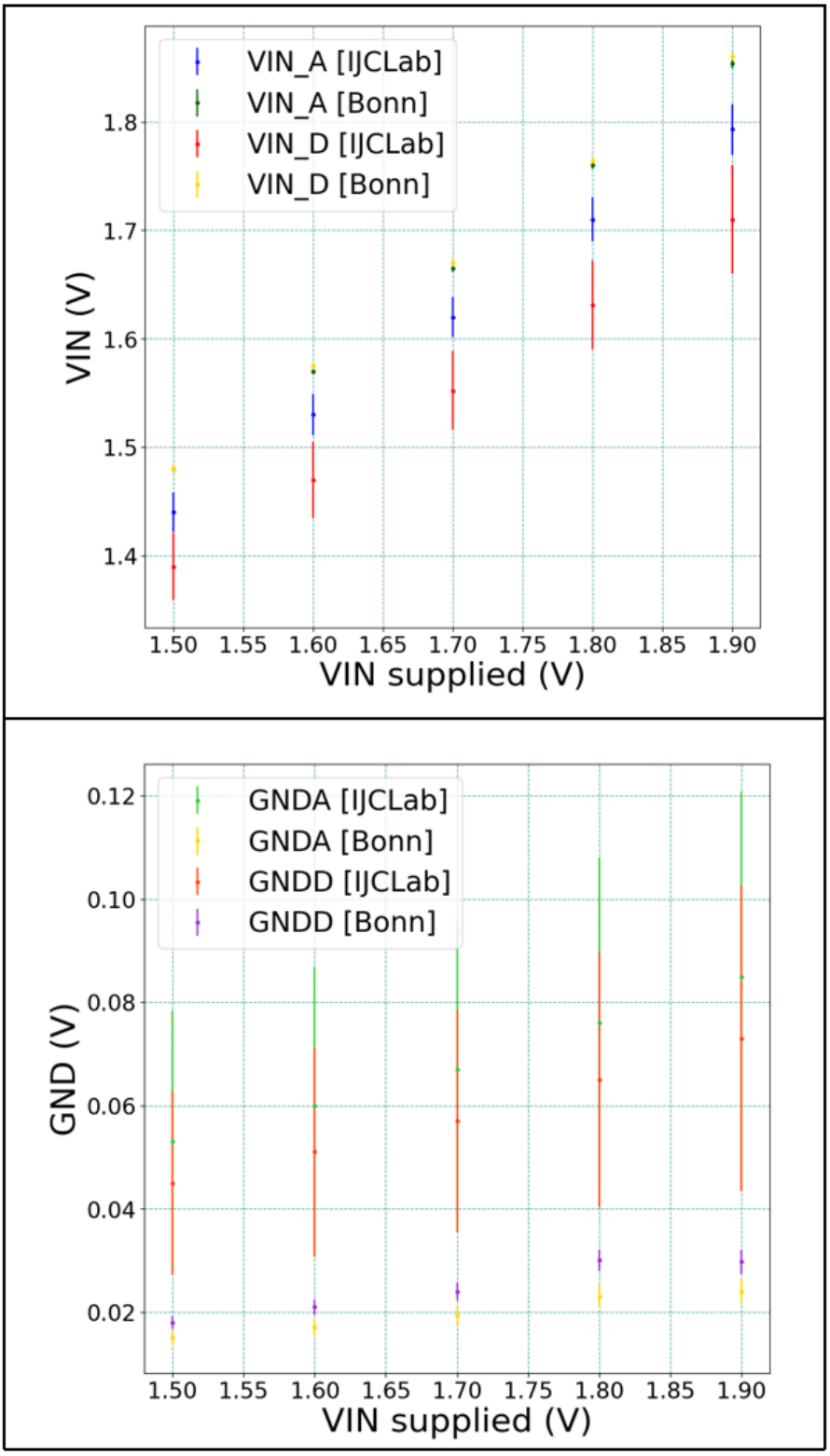

- **Comparison between IJCLab and Reference Results Using Error Bars**

In the upper plot of figure 5.3, the mean value of the parameters VIN_A and VIN_D was plotted versus the corresponding injected voltage values from 1.5 V to 1.6 V for both IJCLab and Bonn results using error bars in order to indicate the uncertainty or the error in the measurements in which the error bars have a length of twice the standard deviation of the distribution. The same plot was done for the ground parameters GNDA and GNDD in the bottom side of figure 5.3.

It was noticed that the error bars for our data were longer than that for the reference data for all the four parameters which is expected because longer error bars indicates a high variability and uncertainty in the measurements.

Also, the error bars for GNDA and GNDD were longer than that for the VIN_A and VIN_D parameters respectively which means that the imprecision in measuring the GNDA and GNDD are higher than that for VIN_A and VIN_D, hence the problem in the ground voltage is bigger. For this reason, only the ground results will be discussed in the next analysis and the GNDA parameter was chosen for the discussion.

5.1.2 The 30 Selected Chips Test

In order to see if there is any correlation between our data and the reference data, the results of our IJCLab 48-hour test on the whole wafer together with the reference results on the same wafer, along with the difference between these two tests results were plotted on the same graph shown in figure 5.4 in which.

It was noticed from figure 5.4 that the difference in the results between the two tests is large and random which is not good, so we have to look at the reasons of this bad correlation.

For this reason, after the 48-hour test, a number of selected chips from the wafer were tested individually. The number of the selected chips was 30 chips and they are shown on the wafer in figure 5.5 a).

The chips were chosen based on whether it were still in a good case to give correct measurements or not. Good here means that its surface is not damaged by the scratching caused by the multiple measurements.

Figure 5.4

Three plots of the GNDA values of the IJCLab's and Bonn's 48-hour tests along with the difference between them

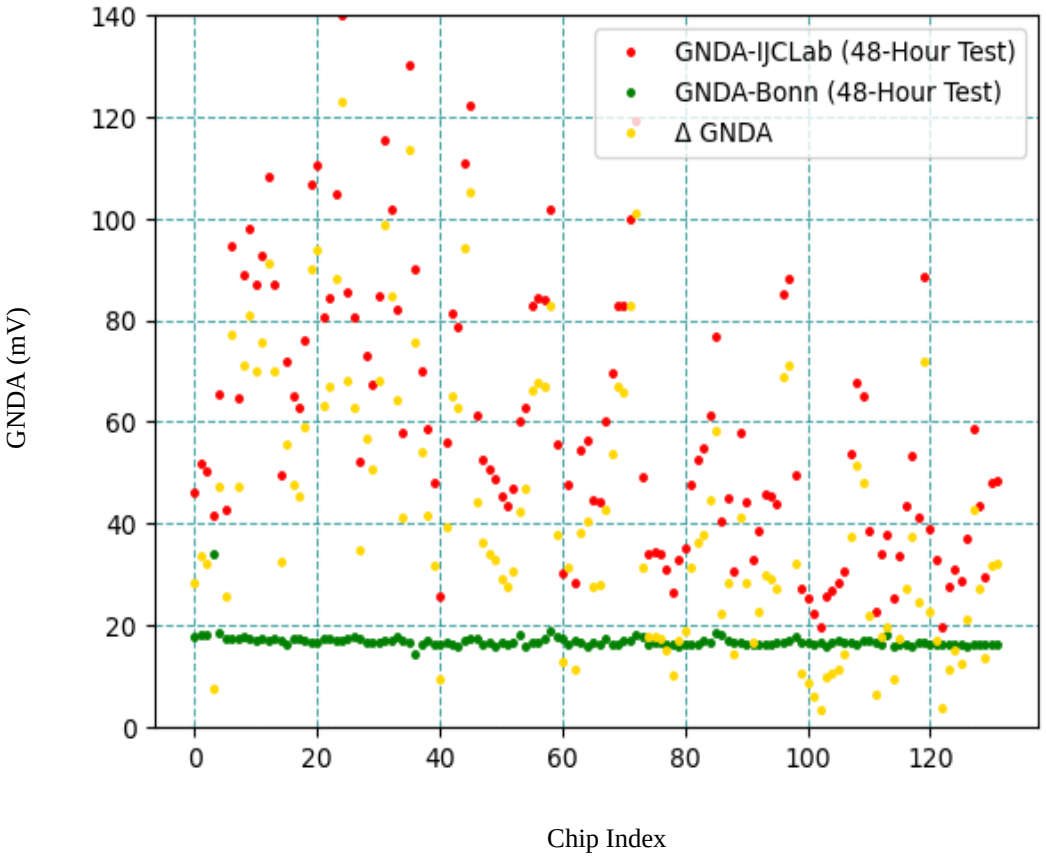

When the chip surface is scratched too much, it will be physically damaged which will cause roughness and irregularities leading to changes in the electrical characteristics of the silicon material which will result in performance degradation and distortion in the signal. As a result, this will negatively affects the reliability of the measurements.

Moreover, while doing the wafer propping tests, these scratches debris may interfere with the contact between the pads of the chips and the probe needles, causing the poor contact that will lead to bad measurements.

The results of these tests for the parameter GNDA along with the results of the 48-hour test of IJCLab and the reference results for the same selected chips were plotted and shown in figure 5.5 b).

It was noticed that the results of the tests that were done on the 30 selected chips is so close to the reference results for the 6^{th} and 7^{th} chips as illustrated in figure 5.5 b) which is a good result because the more the measurements are close to the reference ones, the better.

So we have to investigate the parameters that may cause the results to be that close to the reference results, two of these parameters are the Aurora Lane Test and the Register Test parameters. Those two parameters are basically communication protocols between the ITkPix-V1 chip, the BDAQ53 and the PC.

Figure 5.5

30 selected chips test

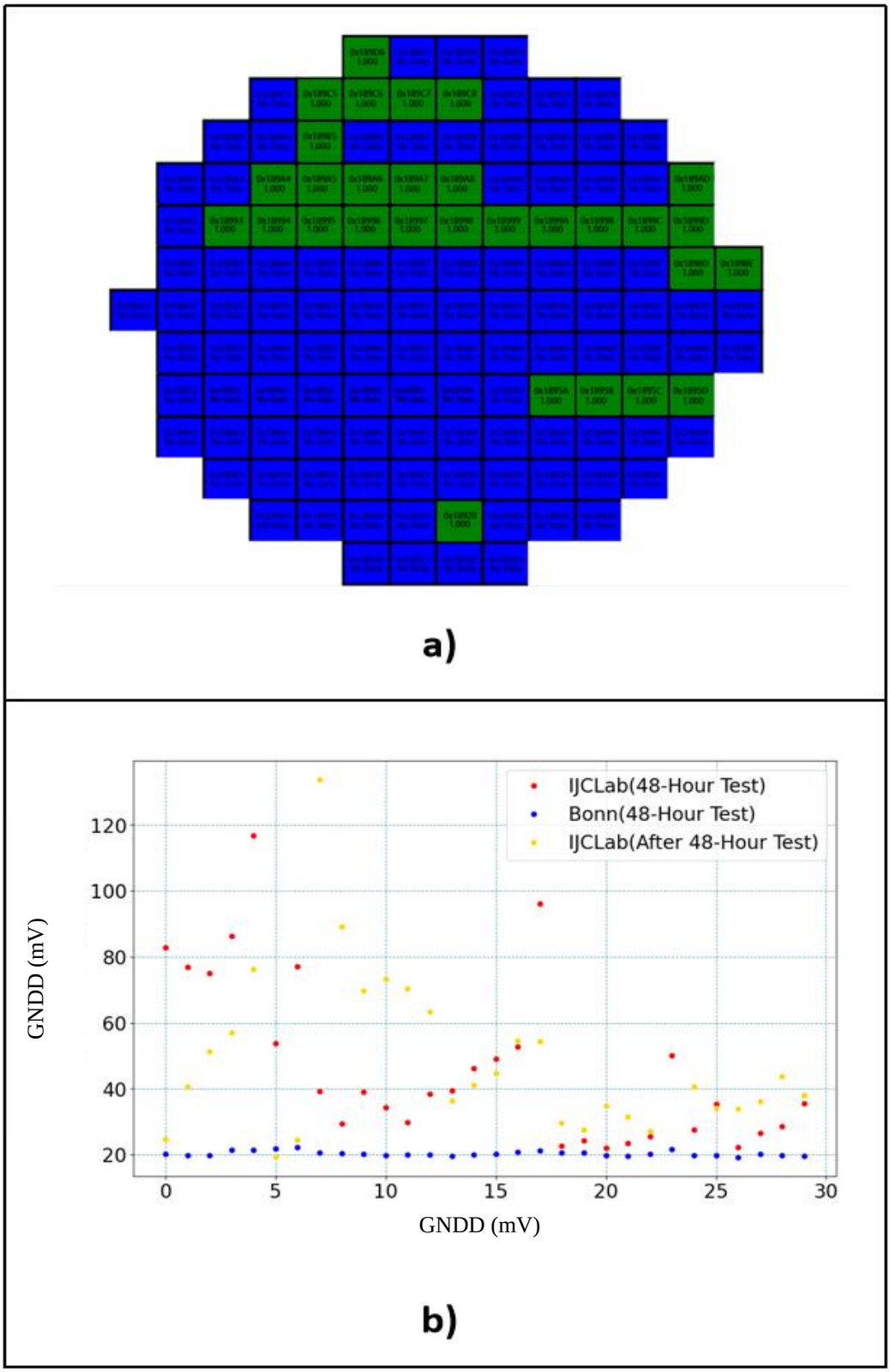

5.1.3 Aurora Lane Test and Register Test parameters Effect on the Measurements

In order to see if the two parameters mentioned in subsection 5.1.2, the Aurora Test and the Register Test are the reason of giving the good results to the two previously mentioned chips, 6^{th} and 7^{th} chips in figure 5.5 b), a histogram of the GNDA values for the IJCLab's 48-hour test when the Aurora Test was succeed, that is, Aurora Test = 1, was plotted as illustrated on the top left part of figure 5.6 a) and another histogram was plotted on the top right part of the figure for the same results when the Aurora Test was failed, that is, Aurora test = 0. The same two histograms was plotted but for the Register Test parameter and are illustrated on the bottom part of figure 5.6 a).

Then, the same histograms of the GNDA values for the two parameters, the Aurora Test and the Register Test were also done for the reference results and are shown in figure 5.6 b)

Regarding the IJCLab histograms, it was noticed that, there were four chips with the Aurora Test succeed, and two chips with the Register Test succeed, which are illustrated in red bars in figure 5.6 a), while in the rest of the chips, the Aurora Test and the Register Test were both failed.

On the other hand, for the reference results histograms, it was noticed that there were two chips with both the Aurora and the Register Tests failed and they are shown in green bars in figure 5.6 b), while in the rest of the chips, the Aurora and Register Tests were both succeed.

From these notes on the two previous figures, figure 5.6 a) and figure 5.6 b), it was suggested that there might be a connection between whether the Aurora Test and Register Test were failed or succeed and the results of the chips being bad or good respectively. That is, those chips in the IJCLab histograms with the Aurora Test or the Register Test succeed might be the same chips that have very close results to the reference results.

Figure 5.6

Histograms of : a) the GNDA results of IJCLab's 48-hour test when both the Aurora and Register Tests were either succed or failed and b) the GNDA results of Bonn's 48-hour test when both the Aurora and Registers Tests were either succed or failed..

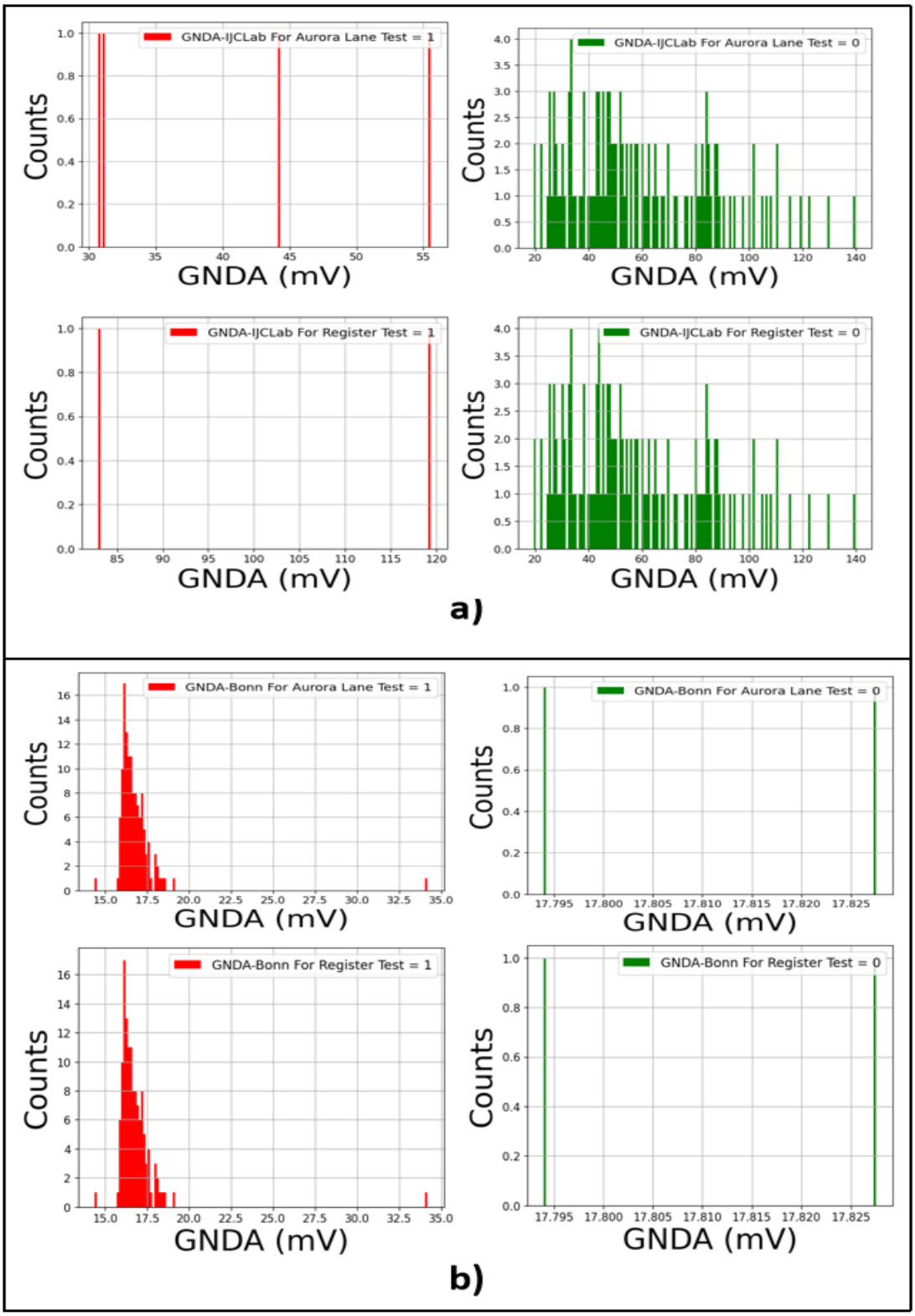

To check the validity of this assumption, a two-plots figure was made, one plot represents the GNDA results for the 48-hour test of IJCLab and the other represents the same results but for reference measurements. The figure is shown in figure 5.7 a). Each marker in these two plots has a specific shape and colour that indicates whether the Aurora Test and Register Test for this specific chip was failed or succeed.

It was noticed that, the points in reference results plot are close to each other forming nearly a straight line shape while the points in IJCLab results plot are random.

If we look at the first green circle shaped marker in refernce results plot we will notice that it's far from the straight line consistency of the plot and closer to the IJCLab result of the same chip, but the green circle marker here refers to the case where the Aurora Test and Register Test were both succeed which goes in contradiction with our assumption, because this note shows that the success of the Aurora Test and The Register Test doesn't necessarily mean that the chip result will be good.

Also, the two red square shaped markers in reference results plot lies within the consistency of the straight line even though the markers with this shape and colour refers to the case for which the Aurora Test and the Register Test were both failed, which also go against our assumption.

Moreover, the closest points from the IJCLab plot to the corresponding reference points are all represented with blue square shaped markers which are markers that refers to the case for which both the Aurora Test and the Register Test were failed, which again opposes our assumption.

As a result, it was concluded that the succeed and failed of the Aurora Test and Register Test is not the reason of the good and bad chip results respectively.

For the previous graph, figure 5.7 a), the vertical lines represents the beginning of each raw in the ITkPix-V1 wafer. It was observed from the IJCLab plot, that there was a noticeable drop in the results at nearly every vertical line, this drop may be caused by the bad planarity of the chuck because if we look at the plot, we can see that it has a snake shape that matches the snake track that the propping test of the chips takes while doing the test as shown in figure 5.7 b).

Figure 5.7

Effect of the Aurora and Register Tests on the measurements: a) two plots for the GNDA values of both IJCLab's and Bonn's 48-hour test and b) the snake-shaped path taken on the wafer while performing the 48-hour test

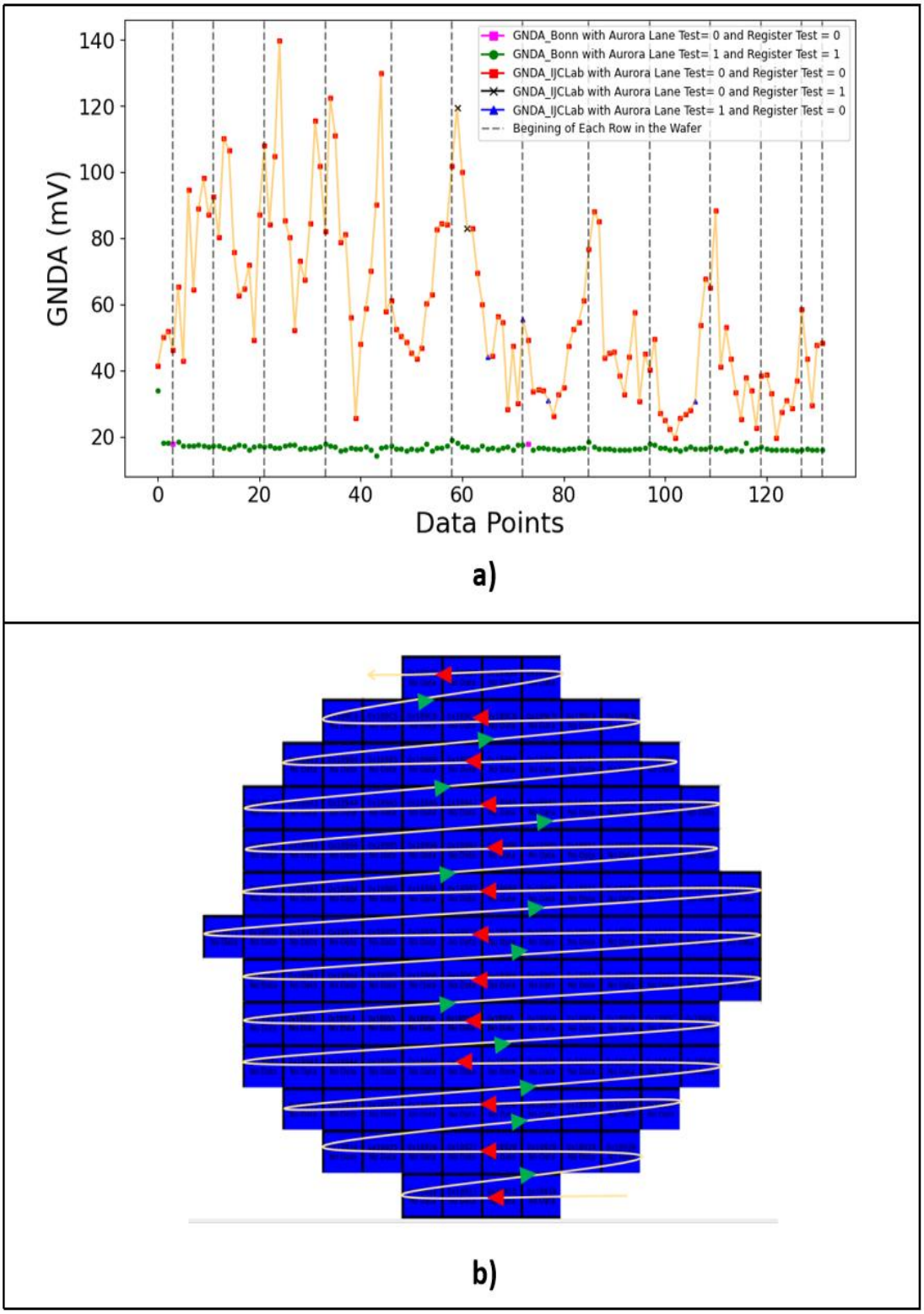

When the planarity of the chuck is well adjusted, that is, the chuck is perfectly aligned to maintain an even and flat surface for the wafer and the sloping angle of the chuck is exactly zero with the horizontal plane, all the needles of the probe card will make an equal contact with the chips pads, so, the contact will be completely equal on any point on the wafer, that is, it will not be stronger in some regions and weaker on others, which will lead to accurate measurements.

However, it appeared here that there was a problem with the planarity adjustment, this problem is explained by figure 5.8 (see Appendix) in which its shown that the wafer surface is inclined as a result of the misalignment of the chuck, therefore, the probe needles that makes contact with the beginning of each row of the wafer surface which is illustrated on the right side of figure 5.8 (see Appendix), is not making a good contact with the chips pads, hence, the drop in the voltage value at every vertical line in figure 5.7 a).

In addition, the probe needles that make contact on the other side of the wafer surface shown in figure 5.8 (see Appendix), are making a very strong contact with the chips pads which will damage the chip surface, hence, inaccurate measurements.

5.1.4 The Five-times Test

Another analysis was done for a new performed test on the chip 0x1896B. We did a test called the five-times test, which means that five tests were performed on the same chip consecutively without moving the chuck between the tests. Here the chip will not be damaged as a side effect of the multiple tests because the chuck didn't move between them so the pads surface will not be impacted by the multiple measurements.

The results of the parameter GNDA of those tests were plotted in a bar plot shown in left side of figure 5.9 a), where the results of the five-times test were represented each by a bar. Also, the result of the 48-hour test for IJCLab for the same chip was also represented by a bar on the same plot, to compare it with the results of the five-times test.

It was noticed in the previous plot that the voltage decreased compared to the voltage resulted from the 48-hour test for the IJCLab and that is very good, since we are facing a high ground voltage problem, that is, the less GNDA value, the better.

However, we still have floating, that is, the voltage is still high. To deal with this floating problem, a trial solution was suggested, this suggestion included separating the connection, that is, the probe card and the BDAQ53 must not be connected to the same power supply. This connection separation will help to create a more controlled and cleaner environment for both of their ground connection and prevent floating which will lead to more accurate, reliable and stable voltage measurements.

Also, for the same set up, additional wires connected to earth were used in which the LEMO connector that connects the probe card to the power supply was connected to earth and the BDAQ53 was also connected to earth as shown in figure 5.10 (see Appendix). This grounding will help stabilize the voltage via improving the noise filtering and lowering the ground impedance.

In addition, it is worth mentioning that, the connection wasn't strong enough while doing this five-times test, therefore, we were careful about ensuring the enough strong connection in the next test.

After doing the modifications explained previously regarding the connection separation, the grounding and ensuring the enough strong connection, the five-times test was repeated. This time, it was performed on a different chip called 0x18944. The reason of using a different chip for the test was to avoid the bad measurements that might be caused by the multiple scratches of the chip surface.

The same bar plot was made for this second five-times test as the previous plot that was done for the chip 0x1896B. This new bar plot is shown on the right side of figure 5.9 a). A great result came out, showing a huge decrease in the voltage value between every bar of each test and the bar that represents the 48-hour test of the IJCLab as shown on the right side of figure 5.9 a). Moreover, there was a stability in the voltage value for all the five tests, since all the five tests bars indicate the same value which was 40 mV.

The results we had got until this point were very good, however, the voltage data is still not perfect, because it doesn't equal to the reference results exactly as shown in figure 5.9 b) where we added to the plot on the right side of figure 5.9 a) a bar that represents the GNDA result from the reference 48-hour test in order to make the desired comparison between them.

Also, another graph was made illustrated in figure 5.11 (see Appendix), It includes two plots, the first one represents a bars plot of the Iref Current parameter results for the five-times test and the 48-hour test for both the IJCLab and the reference measurements, in which each one of these tests was represented by a bar. The second plot represents the Iref Tirm Bit Current parameter where the result of this parameter for each test was represented by a point. It was noticed that the Iref Tirm Bit Current is barely decreased by an amount of around few micro ambers which doest really have an important effect. Also the Iref current is nearly constant, which further confirms that the problem is not a current problem but a voltage one, because the stability of these two current parameters indicates the good measurements.

Figure 5.9

Bars plot of: a) the GNDA values for both the 0x1896B and 0x18944 chips of IJCLab's 48-hour test and the five-times test results. b) the GNDA values for the 0x18944 chip for the five-times test, the IJCLab's and the Bonn's 48-hour tests results

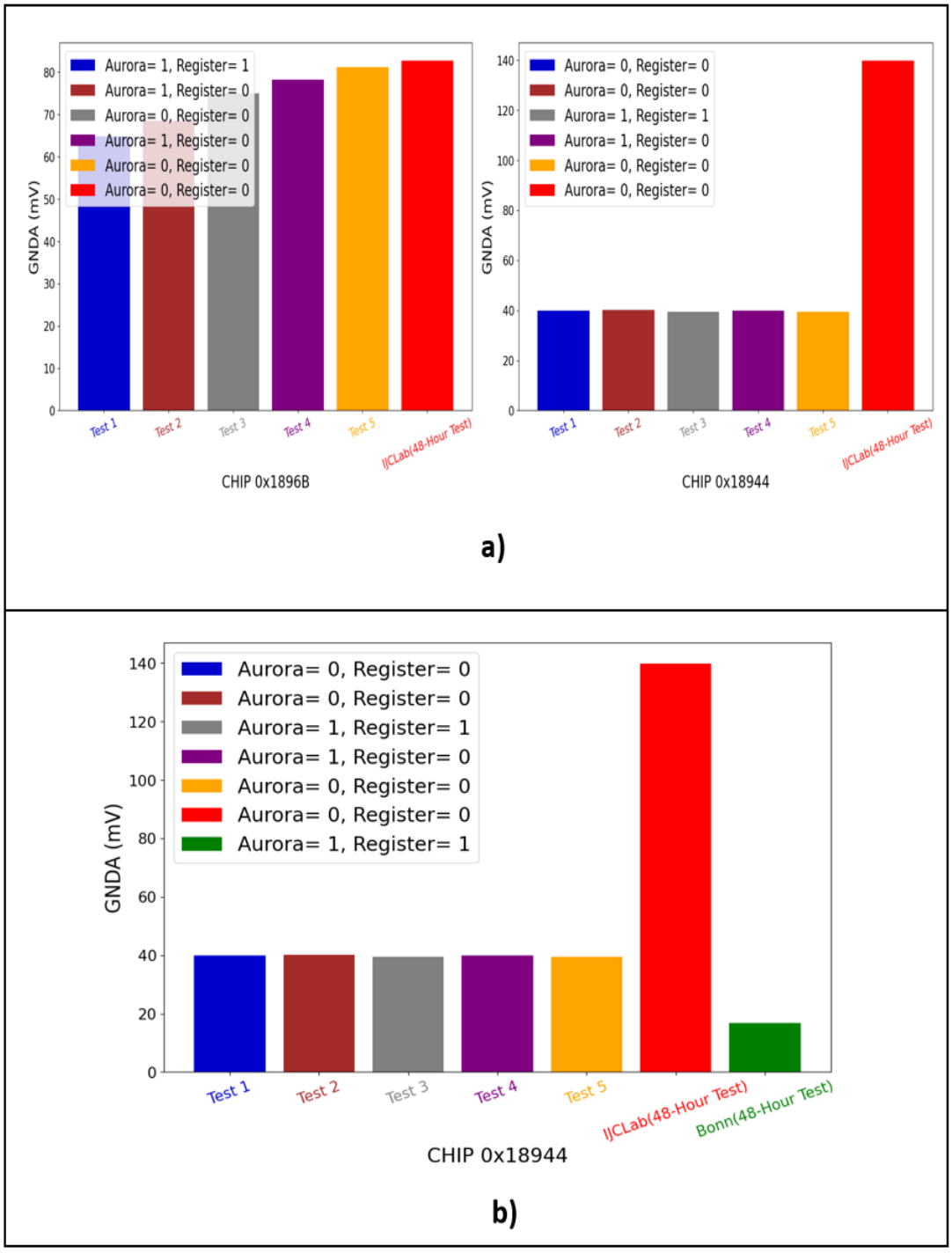

Now to check if this stability and decrease in the voltage value was because of the new connection that was performed or not, a 100 GND loop test was performed on the chip 0x18944 directly after the five-times test. Here the chips surface will not be damaged by the multiple tests just like in the five-times test case because the chuck didn't move between the tests.

The results of these 100 loop measurements were plotted for both the GNDA and GNDD parameters along with the reference results for the 48-hour test measurements of the same parameters for the same chip. The reference results were represented each by a straight line because it's a one value test as illustrated in figure 5.12 a).

In figure 5.12 a), we added the results of the reference 48-hour test measurements in order to compare it with the 100 loop test results, that is, the validity of this test was determined by how close the result is for being a straight line just like the one value test.

It was noticed from figure 5.12 a) that the results weren't completely a straight line, however, there was an apparent stability with some kind of inclined but no noticeable or obvious fluctuations.

After one hour, another 100 loop test was performed to check if the results will differ from the first 100 loop test. Again after three hours, a 500 loop test were performed on the same chip to examine whether a higher tests number will affect the stability , that is, a noticeable fluctuation will appear or not.

The results of the GND values for these three loop tests, the first and second 100 loop tests and the 500 loop test were plotted in figure 5.12 b) in which the three top ones represent the GNDA values of the three loop tests, the first 100 loop test in light blue, the second 100 loop test in light red and the 500 loop test in light green while the bottom three ones represent the same plots of the same tests but for the parameter GNDD in dark colors.

It was noticed that there was a stability in the measurements of each loop test which is good because this indicates that the stability of the measurements is not affected by the number of the performed tests. This proves that the connection separation and grounding solutions succeed in providing stability to the measurements.

Figure 5.12

Plots of: a) the 100 loop test values for the parameters GNDA and GNDD for both IJCLab's and Bonns's results and b) the GNDA and GNDD values for the first and the second 100 loop tests and the 500 loop test

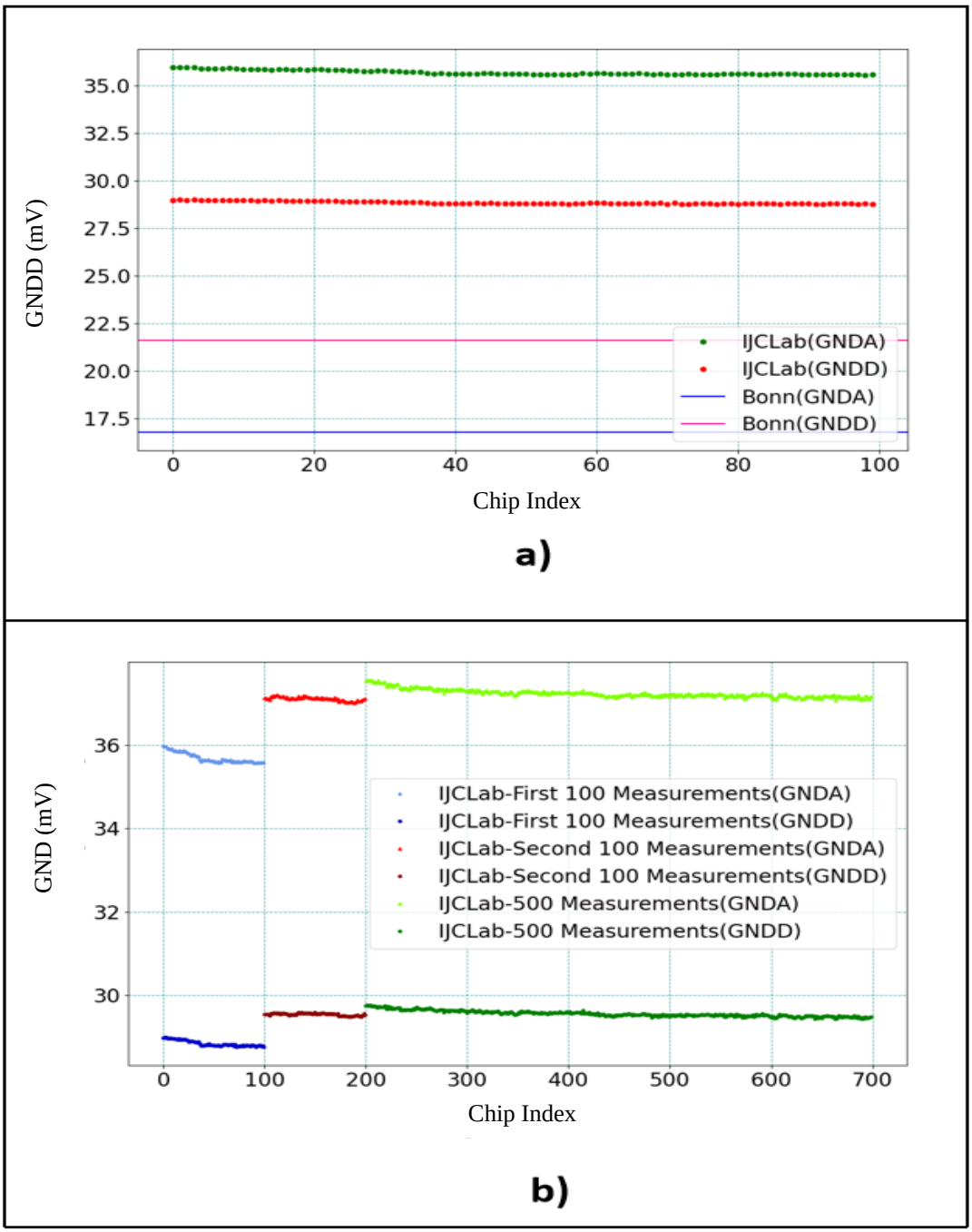

After all those tests, this ITkPix-V1 wafer is not functional anymore, therefore, a new wafer will be used to carry on the analysis. Also, while performing all these tests, it was found that the probes accumulate metal particles from the pad layer when they touch and scratch as illustrated in figure 5.13 (see Appendix), so this problem might also cause the bad measurements since parasitic added resistance which will change the measurement results.

5.2 Conclusion

The experimental part of this thesis is about the wafer probing tests that were performed to qualify the IJCLab team to participate in the quality control of the ITkPix-V1 chip.

This work was done in a clean room at IJCLab, using a wafer probing set-up that consists of a probe station with a BDAQ53 system developed by the University of Bonn.

The tests were done on a wafer containing 132 readout ITkPix-V1 chips, using the BDAQ53 system which is controlled through python software. This wafer has gone under a 48-hour test in the University of Bonn and we have done the same test in IJCLab. The results of this test done by Bonn were taken as reference results for the comparison with IJCLab results.

The comparison of both tests shows that part of the results were similar to the reference results while some results were not. In particular, we measure a relatively large drop in the VIN_A and VIN_D parameters from the injected voltage value. Also we measure high GNDA and GNDD values.

For this reason, I built python codes separated from the python analysis script used in the PC of the experiment in order to analyze the four previously mentions parameters.

It was concluded that there is a large background noise and fluctuations in the measurements, and the problem in the GND parameters is bigger than that in the VIN parameters. It was also observed that the success or fail of the Aurora Test and Register Test parameters was not related to whether the measurements are good or bad respectively.

The main conclusion is, that the problem is a hardware problem rather than a software one, that is, its related to the chuck planarity adjustment and the equipment connection. Also, it was found that the probes accumulate metal particles from the pads surfaces as

they touch and scratch, so this problem may also play a role in the bad measurements as a result of the parasitic added resistance.

Regarding the Planarity, when it's not well adjusted, that is the chuck is not completely horizontal, this causes the touch to be stronger in some regions and not enough in others, resulting in bad electrical contact and thus inaccurate measurements, so we have to ensure the perfect adjustment of the chuck.

As for the Connection, the BDAQ53 and the probe card must be connected to different power supplies to decrease the voltage floating and provide stable voltage measurements. Also, a grounding technique must be performed in which both the BDAQ53 and the probe card should be connected to earth to ensure the voltage stabilization.

In addition to these set-up adjustments, it must be taken care while doing the tests that the connection between the needles and the pads is not too strong, so it do not damage the wafer and not too weak in order to give the needed electrical contact between the probes and pads.

The ITkPix-V1 chip is no longer effective to do more tests, so another wafer will be used to continue the analysis and before doing any other 48-hour tests on the new wafer, the probes must be cleaned, and it must be made sure of the adjustment of the planarity in order to get accurate measurements.

List of Abbreviations

Abbreviation	Meaning
ATLAS	A Toroidal LHC Apparatus
LHC	Large Hadron Collider
HL-LHC	High Luminosity-Large Hadron Collider
ID	Inner Detector
ITk	Inner Tracker
IJCLab	Laboratoire De Physique Des 2 Infinite Irène Joliot-Curie
CERN	Conseil Européen pour la Recherche Nucléaire
ALICE	A Large Ion Collider Experiment
CMS	Compact Muon Solenoid
LHCb	Large Hadron Collider beauty
IBL	Insertable B-Layer
CNRS	Centre national de la recherche scientifique
m	Meter
Linac 4	Linear Particle Accelerator 4
MeV	Mega electron Volt
PSB	Proton Synchrotron Booster
H^-	Negative Hydrogen Atom
H^+	Positive Hydrogen Atom
KeV	Kilo electron Volt
GeV	Giga electron volt
PS	Proton Synchrotron
SPS	Super Proton Synchrotron
Km	Kilo meter
TeV	Tera electron volt
LS 1	Long Shut-down 1
p-p	Proton-proton
LS 2	Long Shut-down 2
VBF	Vector Boson Fusion
cm^{-2}/s^{-2}	$Centimeter^{-2}/second^{-2}$
fb^{-1}	Inverse Femtobarn
n_{eq}	1 Mev-Neutron Equivalent

SUSY	Supersymmetry
LAr	Liquid Argon
T	Tesla
TRT	Transition Radiation Tracker
SCT	Semiconductor Tracker
η	Pseudo-rapidity
FE	Front-end
mm	Millimeter
µm	Micrometer
kV	KiloVolt
Flex PCB	Flexible printed circuit board
P_T	Transverse momentum
Gray	Unit of radiation dose (1 Gray = 1 Joul/ Kilogram)
3D	3 Dimensional
V	Volt
RD53	Research and Development 53
HV	High Voltage
CMOS	Complementary Metal Oxide Semiconductor
BDAQ53	Board for Data Acquisition 53
VIN_A	Voltage input for the analog regulator
VIN_D	Voltage input for the digital regulator
GNDA	Analog ground.
GNDD	Digital ground.

References

1. Tahir NA, Goddard B. Impact of 7-TeV/c large hadron collider proton beam on a copper target. Journal of Applied Physics. 2005 Apr 7;97(8):083532.
2. CERN. The Large Hadron Collider [Available from: https://home.cern/science/accelerators/large-hadron-collider.
3. CERN. High-Luminosity LHC [Available from: https://home.cern/science/accelerators/high-luminosity-lhc.
4. Pernegger H. The Pixel Detector of the ATLAS experiment for LHC Run-2. Journal of Instrumentation. 2015 Jun 23;10(6):C06012.
5. Steentoft J. Aspects of the ATLAS ITk Inner Tracker development for the high luminosity upgrade of the Large Hadron Collider [Licentiate dissertation]. Uppsala: Uppsala University; 2022.
6. Tingey KB. Cycles of Life: Groundings for Human Affairs. ResearchGate 2016 Jul 3.
7. Spurio M, Giacomelli G, Braibant S. Particles and Fundamental Interactions: An Introduction to Particle Physics. 1st ed. Germany: Springer; 2011 Nov 16. 498 p.
8. CERN. The Standard Model [Available from: https://home.cern/science/physics/standard-model.
9. Talios V. The Standard Model Theory [May Be] a Wrong Theory. Journal of High Energy Physics, Gravitation and Cosmology. 2023 Jul;9(3):602-10.
10. May A, Dobrijevic D. The Large Hadron Collider: Inside CERN's atom smasher. Space.com; 2022 Jun 27.
11. CERN. Linear accelerator 4 [Available from: https://home.cern/science/accelerators/linear-accelerator-4.
12. Cid-Vidal X, Cid R, Vretenar M. Using basic electromagnetism to introduce LINAC4 (CERN). Physics Education. 2016 May 25;51(4):044002.
13. CERN. Accelerator upgrades during LS2 [Available from: https://home.cern/press/2022/accelerator-upgrades-during-ls2.

14. Cundy D, Gilardoni S. The Proton Synchrotron (PS): At the Core of the CERN Accelerators. In: Fabjan C, Taylor T, Treille D, Wenninger H, editors. Technology meets research : 60 years of CERN technology : selected highlights. New Jersey: World Scientific Publishing Company; 2017. p. 39-81.
15. Giommi L. Prototype of Machine Learning "as a Service" for CMS Physics in Signal vs Background discrimination [Master thesis]. Italy: Università di Bologna; 2017.
16. Dacey J. CERN achieves 7 TeV collisions at Large Hadron Collider. 2010 Mar 30.
17. CERN. The Higgs boson, ten years after its discovery [Available from: https://home.cern/news/press-release/physics/higgs-boson-ten-years-after-its-discovery.
18. Paus C, Rosati S. The Higgs Boson Discovery. In: Brüning O, Klein M, Rossi L, Spagnolo P, editors. The Future of the Large Hadron Collider: A Super-Accelerator with Multiple Possible Lives. Singapore: World Scientific Publishing Company; 2024. p. 37-49.
19. CERN. LHC prepares for new achievements [Available from: https://hep.phys.uic.edu/news-stories/lhc-prepares-for-new-achievements/.
20. Giagu S. Higgs and New Physics at ATLAS and CMS. Proceeding of Science. 2017 Dec 22;BORMIO2017:033.
21. Elsen E, Bordry F. A successful conclusion to Run 2. CERN; 2018 Dec 11.
22. CERN, Illinois Physics. LHC Run 3: physics at record energy starts July 5. 2022 Jul 4.
23. CERN. LHC Run 3 [Available from: https://home.cern/press/2022/run-3.
24. CERN. CMS Collaboration. THE TWO MOST MASSIVE QUARKS PUT THE SPOTLIGHT ON THE HIGGS BOSON [Available from: https://cms.cern/news/two-most-massive-quarks-put-spotlight-higgs-boson.
25. Herr W, Muratori B. Concept of luminosity. CAS - CERN Accelerator School: Intermediate Course on Accelerator Physics; CERN, Geneva, Switzerland: CERN; 2006. p. 361-78.
26. Dunning H. Ground broken on upgrades to the Large Hadron Collider. IMPERIAL; 2018 Jun 15.

27. Sguazzoni G. The CMS Pixel Detector for the High Luminosity LHC. The International Workshop on Vertex Detectors (VERTEX 2022); Tateyama, Japan: CERN; 2022 Dec 11. p. 11.

28. Lamont M. An encouraging start for Run 3. CERN; 2022 Aug 31.

29. CMS Collaboration. CMS Silicon Strip Tracker Performance in 2023. CERN; 2023 Jul 14. CMS DP -2023/040.

30. Calace N, on behalf of the ATLAS Collaboration. Track and Vertex reconstruction in ATLAS for LHC Run-3 and High-Luminosity phases. European Physics Society conference on High Energy Physics 2021; Online conference: CERN; 2021 July 26.

31. Moscatelli F, Morozzi A, Passeri D. Analysis of surface radiation damage effects at HL-LHC fluences: Comparison of different technology options. Nuclear Instruments and Methods in Physics Research, Section A: Accelerators, Spectrometers, Detectors and Associated Equipment. 2019 Apr 21;924:198-202.

32. The High-Luminosity LHC (HL-LHC) Project. CERN; 2016 May 30.

33. Kurashige H. Highlight of Results from ATLAS at LHC. Physics Procedia. 2015 Dec 80: 14-8.

34. Hooberman B, on behalf of the ATLAS Collaboration. First tracking performance results from the ATLAS Fast TracKer. Connecting the Dots and Workshop on Intelligent Trackers (CTD/WIT 2019); ; Instituto de F´ısica Corpuscular (IFIC), Valencia, Spain: CERN; 2019 Nov 11. p. 8.

35. Kate HT. Superconducting Magnet System for the ATLAS Detector at CERN. IEEE Transactions on Applied Superconductivity. 1999 Jun;9(2):841-6.

36. ATLAS Collaboration. Successful mapping of the solenoid magnet 2006 Oct 5 [Available from: https://atlas.cern/updates/news/successful-mapping-solenoid-magnet.

37. Morgenstern S. ATLAS LAr calorimeter performance in LHC Run-2. Nuclear Instruments and Methods in Physics Research Section A: Accelerators, Spectrometers, Detectors and Associated Equipment. 2019 Aug 21; 936:86-9.

38. Boumediene DE. ATLAS calorimeters: Run 2 performance and Phase-II upgrades. Proceeding of Science. 2018 Mar 20;EPS-HEP2017:485.

39. Solovyanov O. Performance of the ATLAS Hadronic Tile Calorimeter in Run-2 and its Upgrade for the High Luminosity LHC. The European Physical Journal Conferences. 2017 Jan;158(1):06002.

40. Assran Y, Sharma A. Transport Properties of operational gas mixtures used at LHC. 2011 Oct 31. arXiv:1110.6761 [physics.ins-det].

41. Snuverink J. The ATLAS muon spectrometer: commissioning and tracking [PhD thesis]. Twente, Enschede: University of Twente; 2009 Oct.

42. Matheson J, Taylor J. ATLAS ITk pixel endcap demonstrator "Ring-0" construction and testing. Nuclear Instruments and Methods in Physics Research Section A: Accelerators, Spectrometers, Detectors and Associated Equipment. 2021 Jan 11; 986:164753.

43. Bingül A. The ATLAS TRT and its Performance at LHC. Journal of Physics: Conference Series. 2012 Feb;347(1):012025.

44. Alison J. Alignment of the ATLAS Inner Detector Tracking System. Proceeding of Science. 2009 Oct 8;ACAT08: 074.

45. CERN. The Inner Detector [Available from: https://atlas.cern/Discover/Detector/Inner-Detector.

46. Llacer MM, for the ATLAS SCT collaboration. ATLAS SemiConductor Tracker: Operation and Performance. 2011 IEEE Nuclear Science Symposium and Medical Imaging Conference; Valencia, Spain: CERN; 2011 Oct. p. 5.

47. Campabadala F, Fleta C. Design and performance of the ABCD3TA ASIC for readout of silicon strip detectors in the ATLAS semiconductor tracker. Nuclear Instruments and Methods in Physics Research Section A: Accelerators, Spectrometers, Detectors and Associated Equipment. 2005 Nov;552(3):292-328.

48. Nagai K. ATLAS Strip Detector: Operational Experience and Run 1-> Run 2 Transition. Proceeding of Science. 2015 May 21;Vertex2014:002.

49. The ATLAS collaboration. Operation and performance of the ATLAS semiconductor tracker in LHC Run 2. Journal of Instrumentation. 2022 Jan 10;17:P01013.

50. The ATLAS TRT collaboration. The ATLAS TRT Barrel Detector. Journal of Instrumentation. 2008 Feb 29;3:P02014.

51. Mindur B. ATLAS Transition Radiation Tracker (TRT): Straw Tubes for Tracking and Particle Identification at the Large Hadron Collider. Nuclear Instruments and Methods in Physics Research Section A: Accelerators, Spectrometers, Detectors and Associated Equipment. 2017 Feb 11;845:257-61.

52. Vogel A. ATLAS Transition Radiation Tracker (TRT): Straw Tube Gaseous Detectors at High Rates. Nuclear Instruments and Methods in Physics Research Section A: Accelerators, Spectrometers, Detectors and Associated Equipment. 2013 Dec 21;732:277-80.

53. Aaboud M. Performance of the ATLAS Transition Radiation Tracker in Run 1 of the LHC: tracker properties. Journal of Instrumentation. 2017 May 3;12(5):P05002.

54. Fournier D, Virdee T. The ATLAS and CMS detectors at the LHC. Comptes Rendus Physique. 2015 May 14;16(4):356-67.

55. Aad G, Ackers M. ATLAS pixel detector electronics and sensors. Journal of Instrumentation. 2008 Jul 24;3(7):P070

56. Große-Knetter J. Vertex Measurement at a Hadron Collider-The ATLAS Pixel Detector [PhD thesis]. Germany: Bonn University, Physikalisches Institut; 2008.

57. Mandelli B. The Pixel Detector of the ATLAS Experiment for the Run 2 at the Large Hadron Collider. Nuclear and Particle Physics Proceedings. 2016 Apr;273-275:1166-72.

58. Mijovic L. Track reconstruction in high-multiplicity environments with the ATLAS Detector at the LHC. Proceeding of Science. 2018 Dec 21;LHCP2018:036.

59. MOSKOWITZ C. Higgs Boson Looks "Standard," but Upgraded LHC May Tell a Different Tale. Scientific American; 2014 Jun 26.

60. SALEEM T. Development of pixel detector for ATLAS Inner Tracker (ITk) upgrade at HL-LHC and Searching for the Standard Model Higgs boson decay into b-quark pair with ATLAS experiment [PhD thesis]. France: Université Paris Saclay (COmUE); 2019 Jan 8.

61. La-Rosa A. The ATLAS Insertable B-Layer: from construction to operation. Journal of Instrumentation. 2016 Dec 15;11(12):C12036.

62. Wermes N. Pixel Vertex Detectors. 2006 Nov 7. arXiv:physics/0611075 [physics.ins-det].

63. Franconi L. Insertable B-Layer integration in the ATLAS experiment and development of future 3D silicon pixel sensors [PhD thesis]. Norway: University of Oslo; 2018

64. Backhaus M. Characterization of new hybrid pixel module concepts for the ATLAS Insertable B-Layer upgrade. Journal of Instrumentation. 2012 Jan 10;7(1):C01050.

65. Raighne AM. Precision scans of the Pixel cell response of double sided 3D Pixel detectors to pion and X-ray beams. Journal of Instrumentation. 2011 May 5;6(5):P05002.

66. Duarte-Campderros J, on behalf of the RD50 Collaboration. Pixelated 3D sensors for tracking in radiation harsh environments. Journal of the Physical Society of Japan. 2021;34:010005.

67. Takubo Y. ATLAS IBL operational experience. Proceeding of Science. 2017 Aug 3;Vertex 2016:004.

68. Roy-Garand S. ATLAS Inner TracKer Upgrade. Proceeding of Science. 2024 Jan 15;LHCP2023:002.

69. Carney R. Silicon Tracking and a Search for Long-lived Particles [PhD thesis]. Stockholm: Stockholm University; 2019.

70. Ravera S. Development of systems and test of devices for the ATLAS ITk detector moving from R & D to construction [Master thesis]. Italy: Universita di Genova; 2022 Sep.

71. The ATLAS Collaboration. Clustering and Tracking in Dense Environments with the ATLAS Inner Tracker for the High-Luminosity LHC. ATL-PHYS-PUB-2023-022. Geneva: CERN; 2023 Aug 14.

72. Mclaughlin D, Scanlon T. Improving the tracking performance in dense jets within the ATLAS detector. UCL – IOP HEP & APP CONFERENCE; DEPARTMENT OF PHYSICS & ASTRONOMY, UNIVERSITY COLLEGE LONDON: ATLAS Experiment; 2022 Apr 5.

73. Gonella L. The ATLAS ITk Detector System for the Phase-II LHC Upgrade. Nuclear Instruments and Methods in Physics Research Section A: Accelerators, Spectrometers, Detectors and Associated Equipment. 2023 Jan 1;1045:167597.

74. Kuehn S. The Upgrade of the Inner Tracker of the ATLAS experiment for the High-Luminosity LHC. CERN Detector Seminar. 2019 Nov 29.

75. Wang H. The ATLAS experiment at the LHC. University of California, Berkeley. 2020 Sep 9.

76. Alonso AG, on behalf of the ATLAS ITk Collaboration. ATLAS ITk Strip Detector for the Phase-II LHC Upgrade. Proceeding of Science. 2024.

77. Mandić I. Design and construction of the ATLAS ITk Strip Detector. Proceeding of Science. 2024 Jun 25;VERTEX2023:020.

78. Wonsak S. The ATLAS ITk Strip Detector System for the Phase-II LHC Upgrade. Proceeding of Science. 2020 Sep 14;Vertex2019:017.

79. Latonova V, Allportc PP, Bachd E. Characterization of the Polysilicon Resistor in Silicon Strip Sensors for ATLAS Inner Tracker as a Function of Temperature, Pre- And Post-Irradiation. Nuclear Instruments and Methods in Physics Research Section A: Accelerators, Spectrometers, Detectors and Associated Equipment. 2023 May;1050:168119.

80. Meng L, on behalf of the ATLAS Collaboration. ATLAS ITk Pixel Detector Overview. 2021 May 21. arXiv:2105.10367 [physics.ins-det].

81. Heggelund AL, Sanchez FM, Rizatdinova F. Overview of the ATLAS ITk Pixel Detector. Journal of Instrumentation. 2023 Feb 7;18(2):C02014.82. Meng L. Module and System Test Development for the Phase-II ATLAS ITk Pixel Upgrade. Proceeding of Science. 2020 Apr 21;TWEPP2019:122.

83. Hayward H. ITk Pixel Detector Overview. The International Workshop on Vertex Detectors (VERTEX 2022); Tateyama, Japan: CERN; 2022 Oct 26.

84. Standke MH. Characterization of the Joined ATLAS and CMS RD53A Pixel Chip [Master thesis]. Bonn, Germany: Bonn University; 2019 Mar 1.

85. Menouni M. Single event effects testing of the RD53B chip. Journal of Physics: Conference Series. 2022 Nov;2374(1):012084.

86. The RD53B Pixel Readout Chip Manual (Version 1.31). 2020 Sep 13. 130 p.

87. Loddo F, Bari INFN, on behalf of the RD53 Collaboration and ITkPixV1 Testing Team. RD53 status report. 2021 Jun 2.

88. Standke M, on behalf of the RD531 and The ATLAS ITk Pixel Collaboration. RD53B Wafer Testing for the ATLAS ITk Pixel Detector. Journal of Physics: Conference Series. 2022;2374(1):012087.

89. Sharma A, on behalf of the ATLAS ITk Collaboration. Module development for the ATLAS ITk Pixel Detector. Journal of Physics: Conference Series. 2022;2374 (1)012068.

90. Möbius S, on behalf of the ATLAS ITk Group. Module development for the ATLAS ITk pixel detector. Journal of Instrumentation. 2022 Mar 28;17(3):C03042.

Appendices

Appendix A

Figures

Figure 1.1

Schematic view of the LHC ring and the four main LHC detectors, ATALS, CMS, ALICE and LHCb

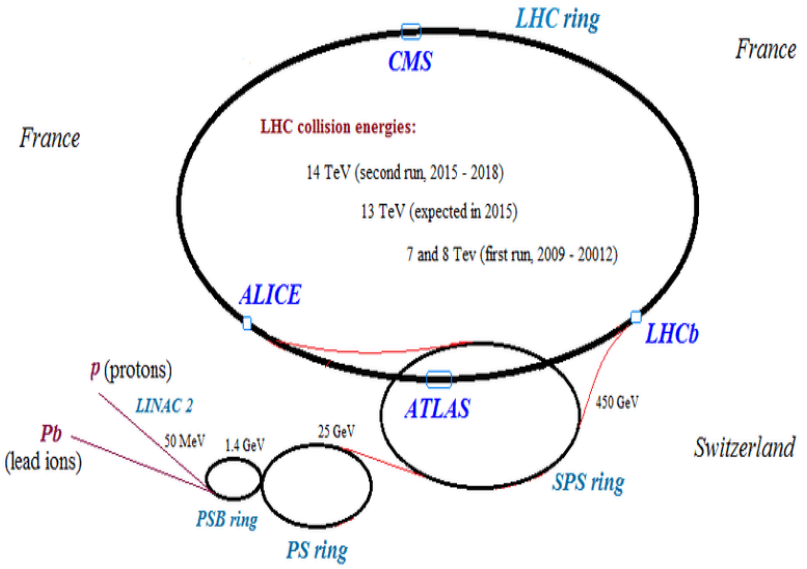

Figure 1.2

The Standard Model

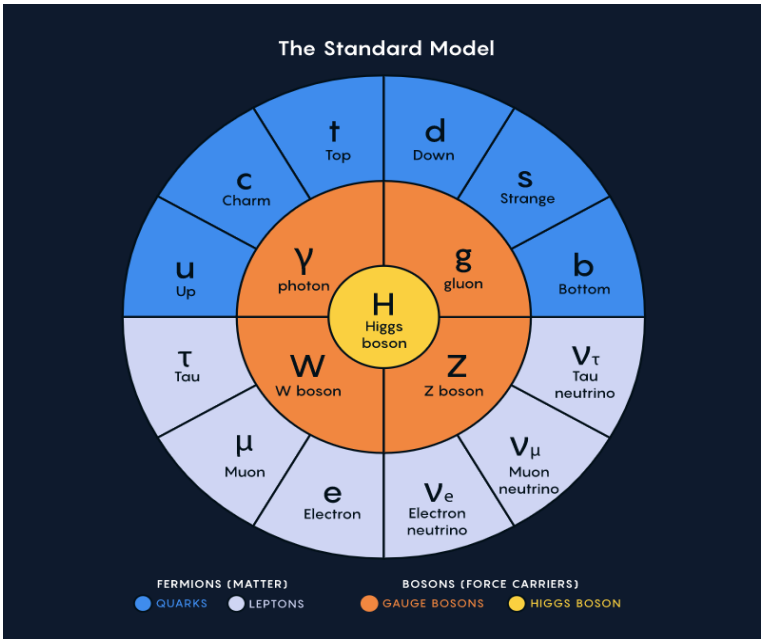

Figure 1.3

Linear accelerotor(linac): a) Linear Accelerator working Principle and b) Linac4 Layout

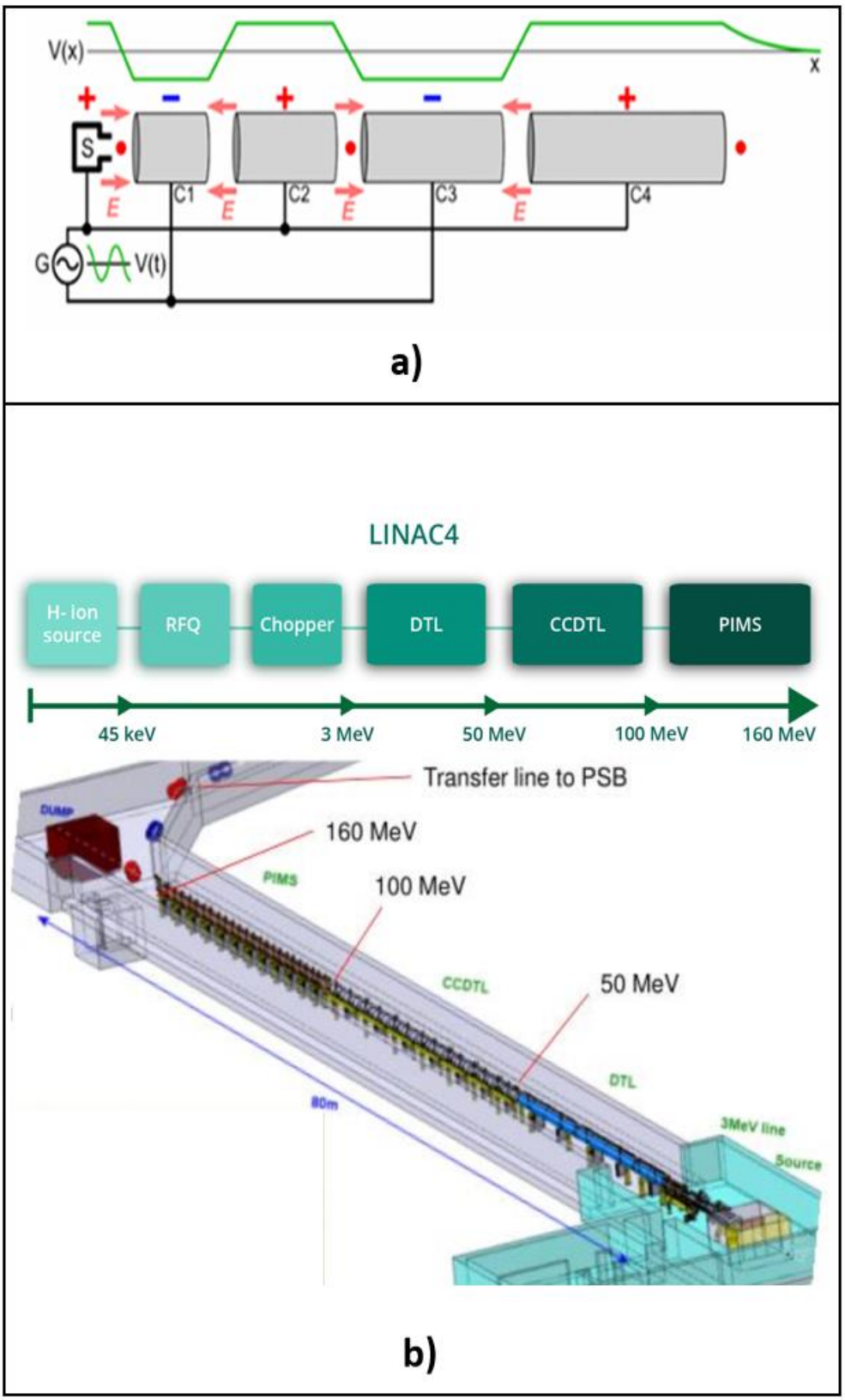

Figure 1.4

Schematic view of the LHC showing the locations where the stages of accelerations happens

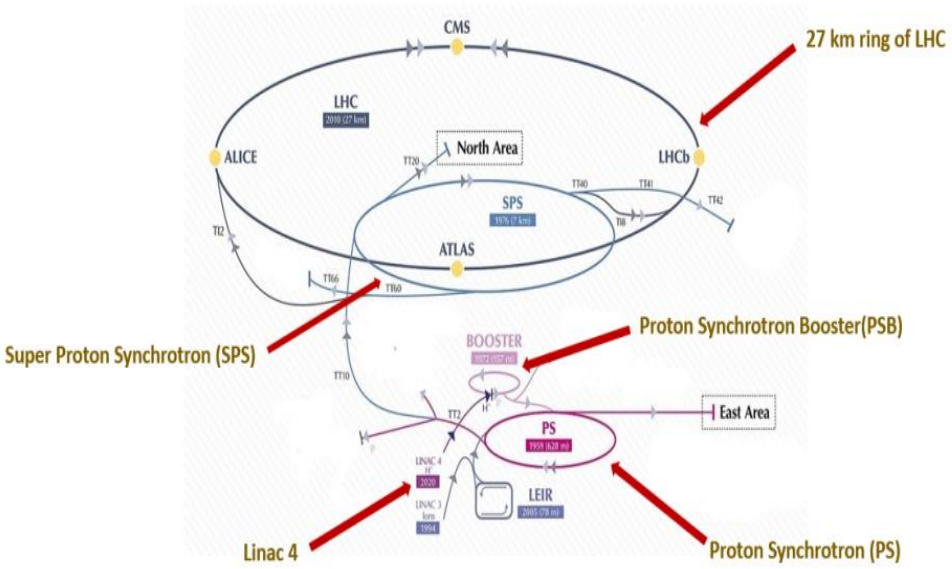

Figure 1.5

LHC/HL-LHC running plan

Figure 2.1

ATLAS detector at the LHC with illustration of its main components

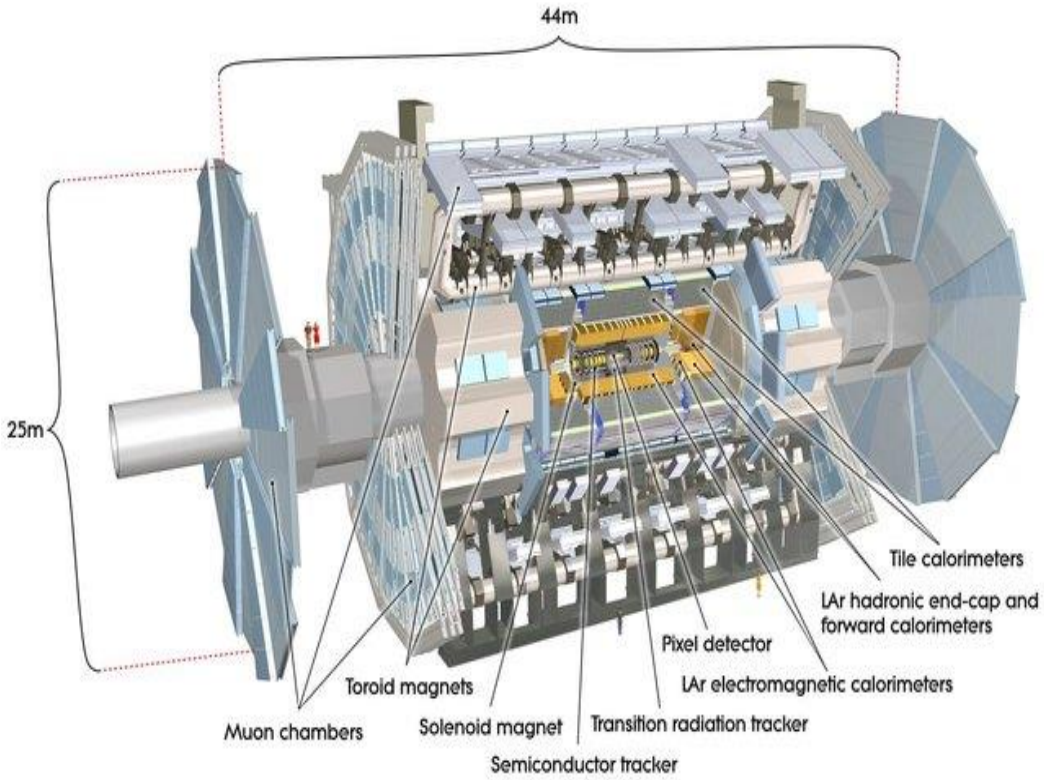

Figure 2.2

Schematic view of the magnet system of ATLAS

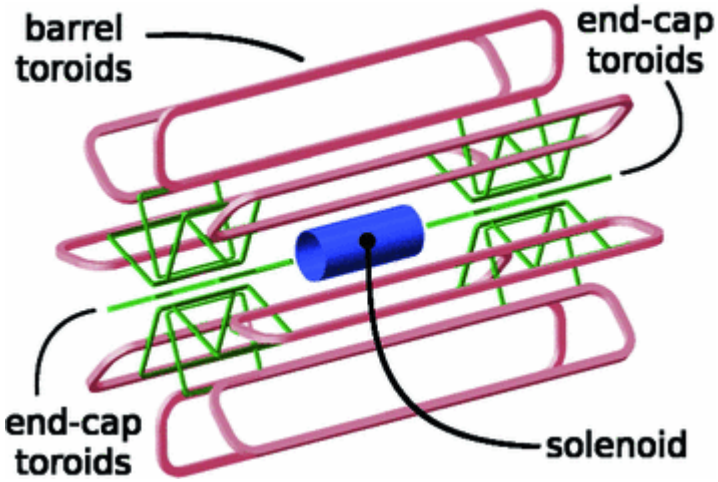

Figure 2.3

Schematic view for ATLAS calorimeters

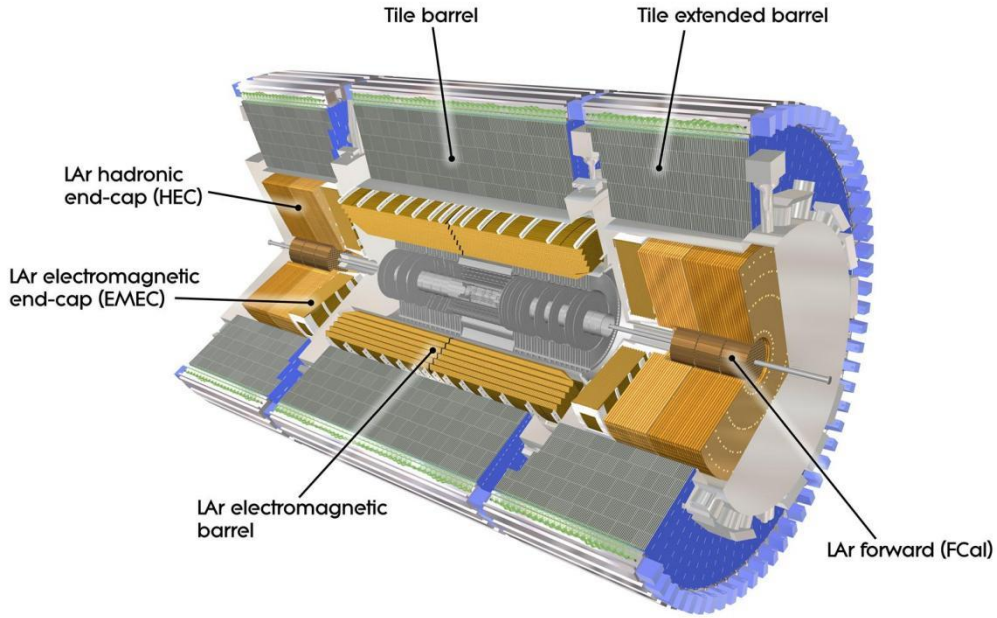

Figure 2.4

Detection of different particles in ATLAS: a) particle identification through ATLAS sub-detectors and b) illustration of how different particles interact with the layers of ATLAS

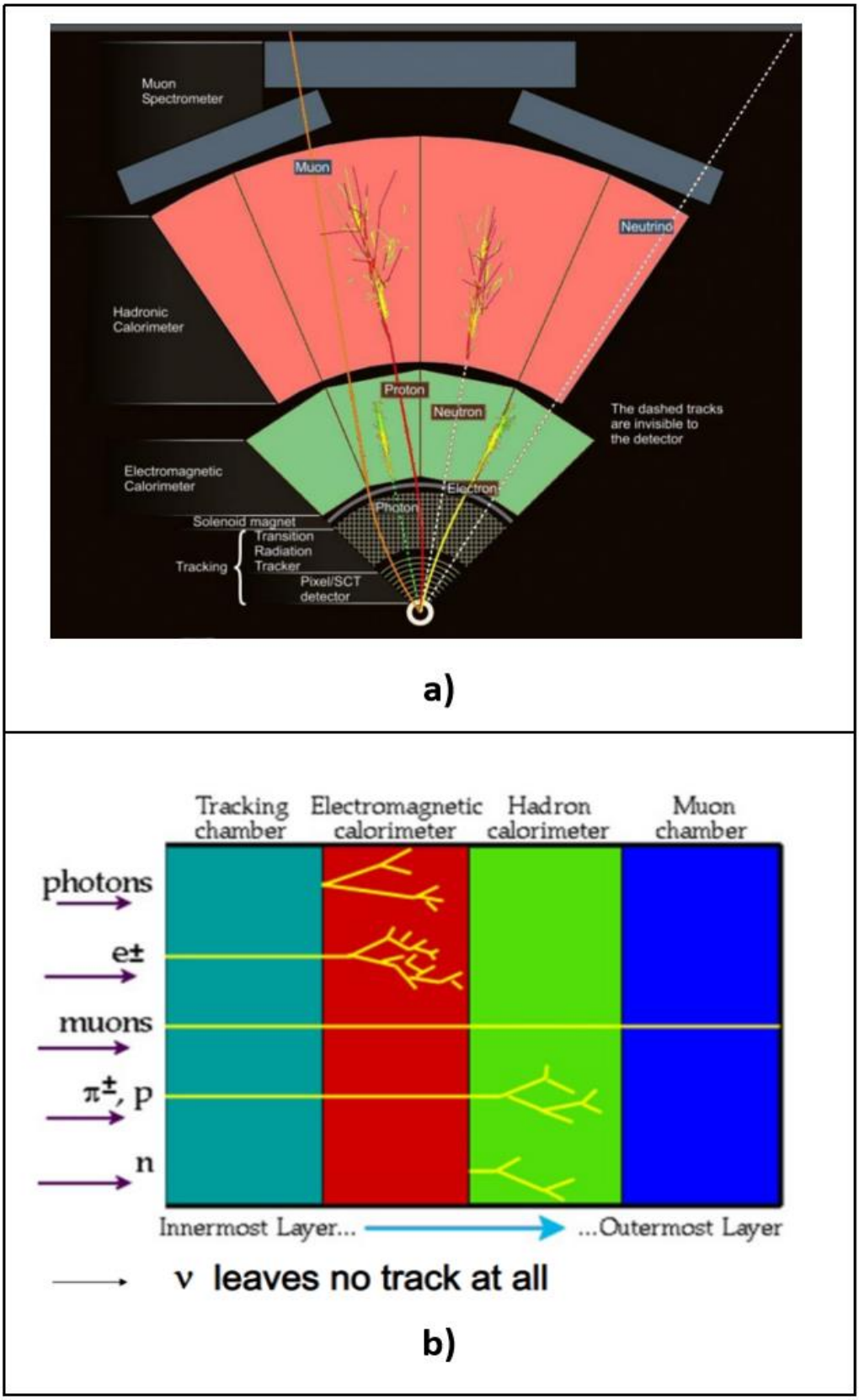

Figure 2.5

Layers of the ID of ATLAS: a) layout of ATLAS's ID layers and b) trajectory of the particle while it passes through the ID layers

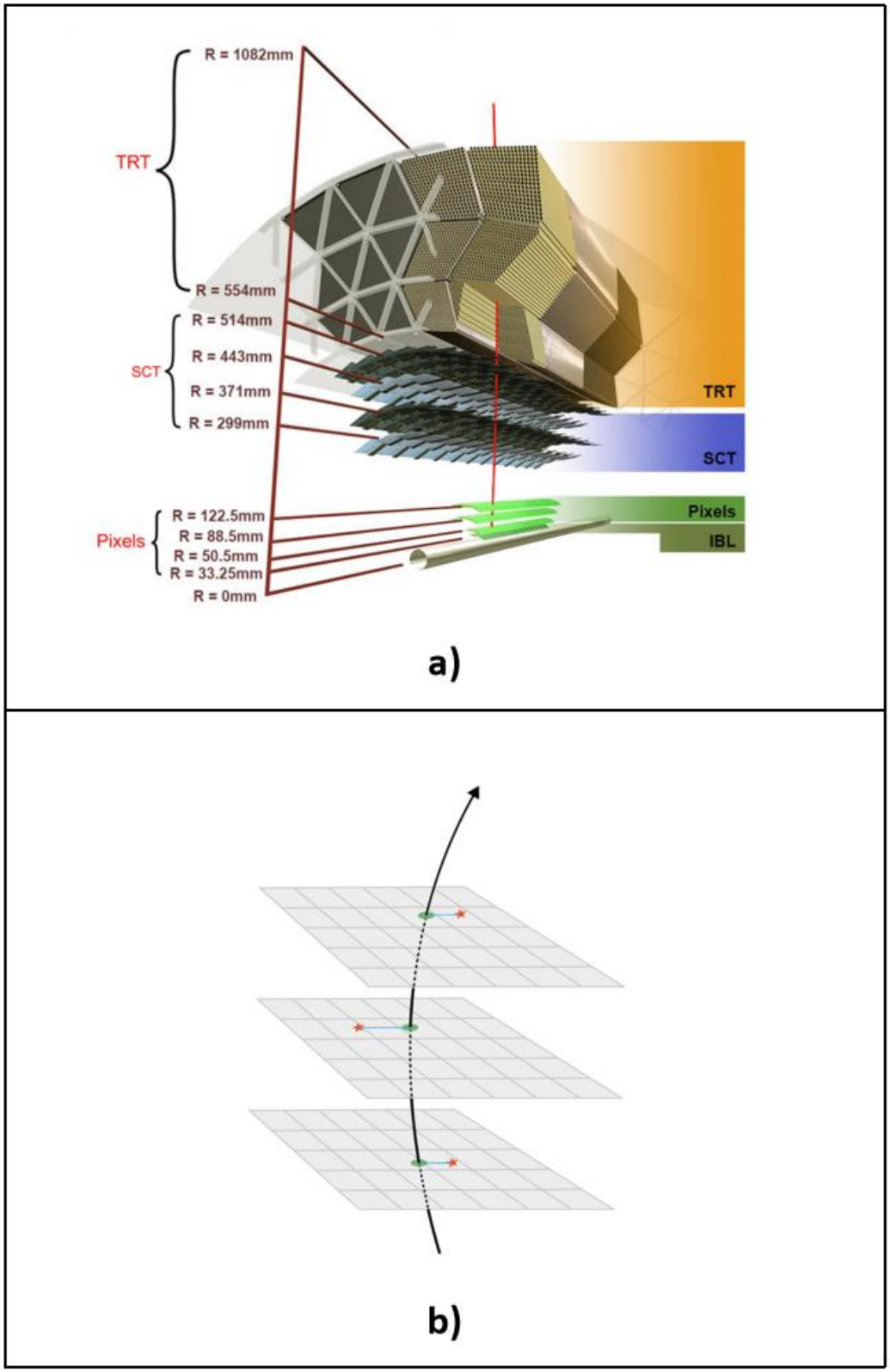

Figure 2.6

Schematic view of the ID of ATLAS

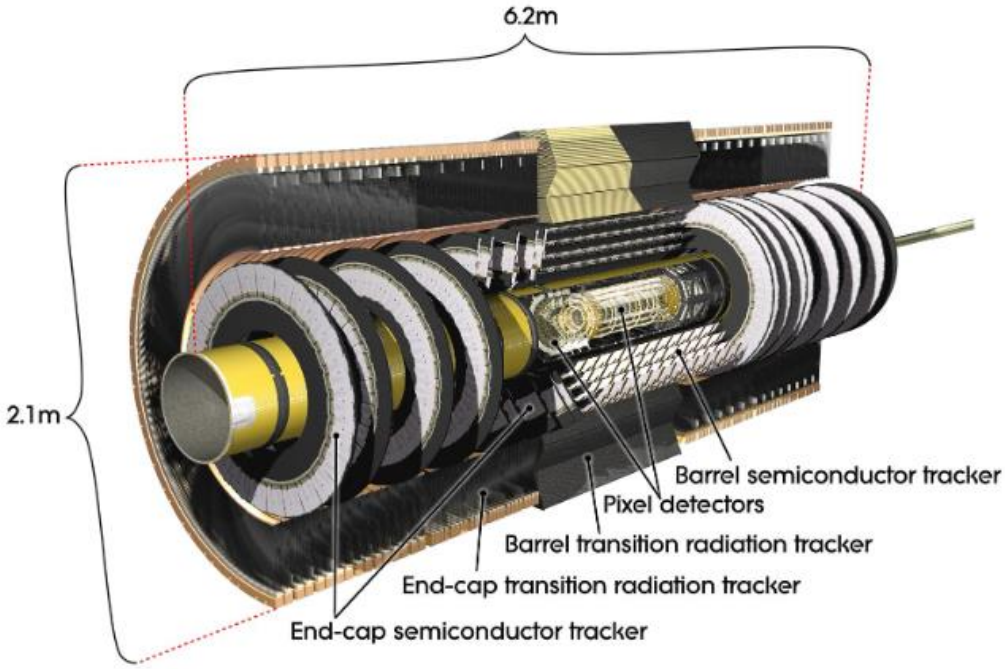

Figure 2.7

SCT and TRT of ATLAS detector: a) schematic view of the SCT of ATLAS and b) schematic view of the TRT of ATLAS

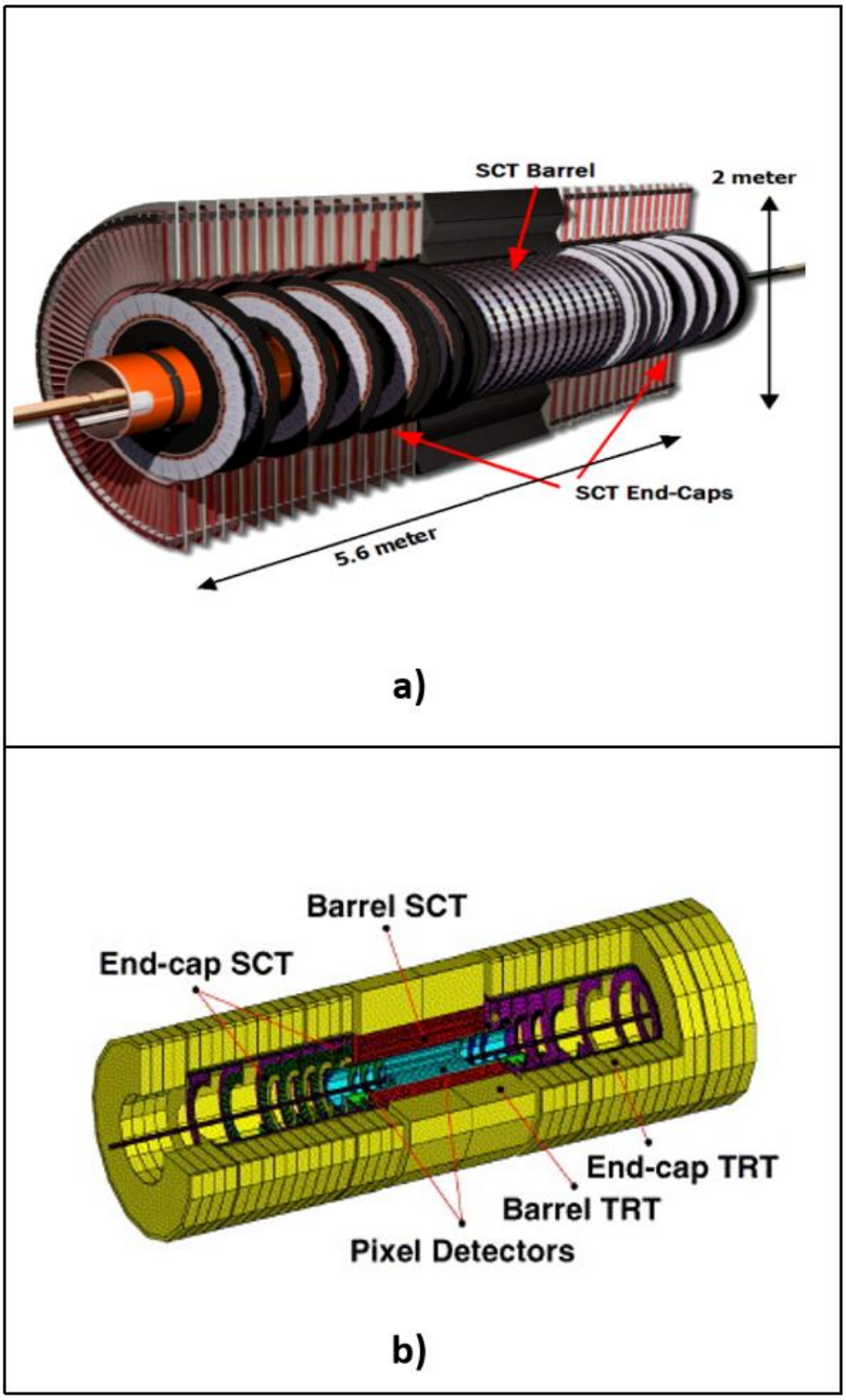

Figure 2.8

Schematic view of the pixel detector of ATLAS

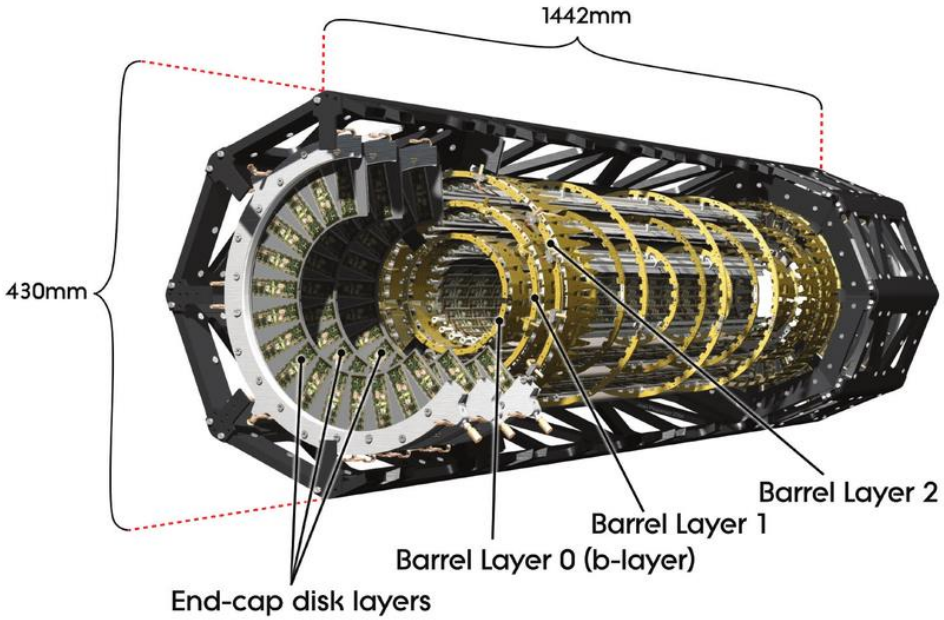

Figure 2.9

Layers of the pixel module illustrating the solder bumps layer that connects the readout layer with the sensor layer

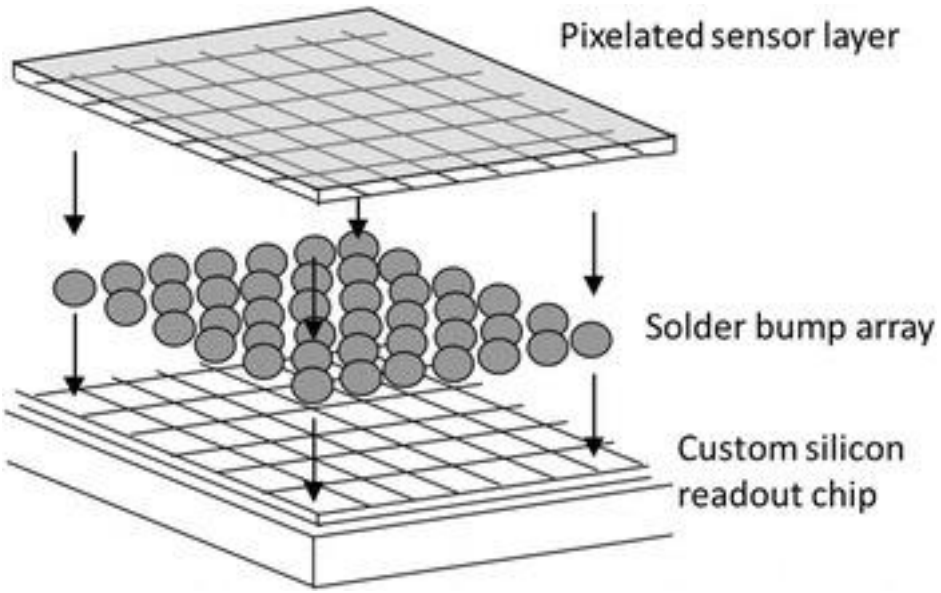

Figure 2.10

Hybrid pixel detector: a) schematic view of the layers of the hybrid pixel detector and b) pixel cell from the hybrid pixel detector

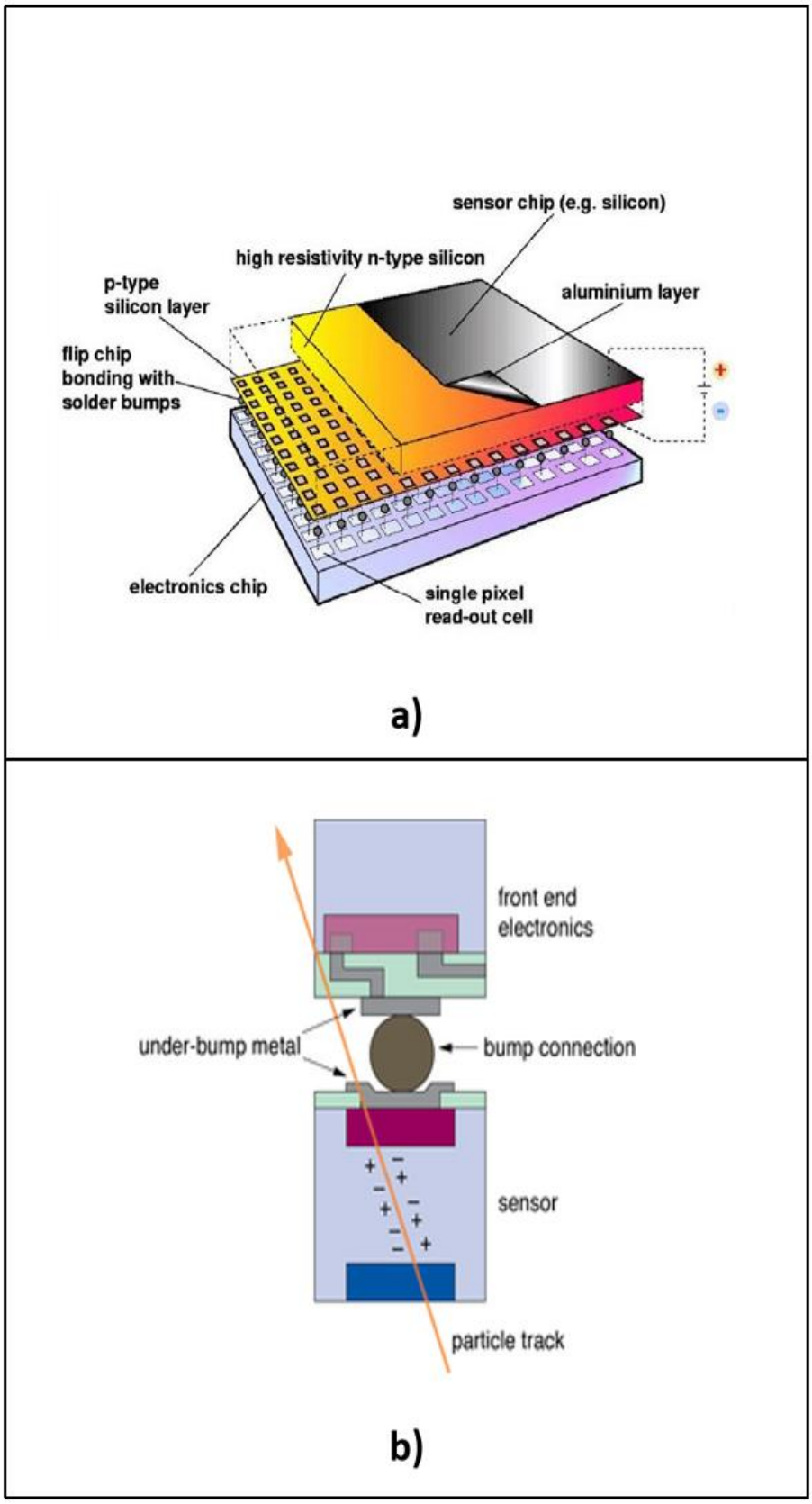

Figure 2.11

Diode formation: a) n-type and p-type doped silicon and b) pn-junction diode

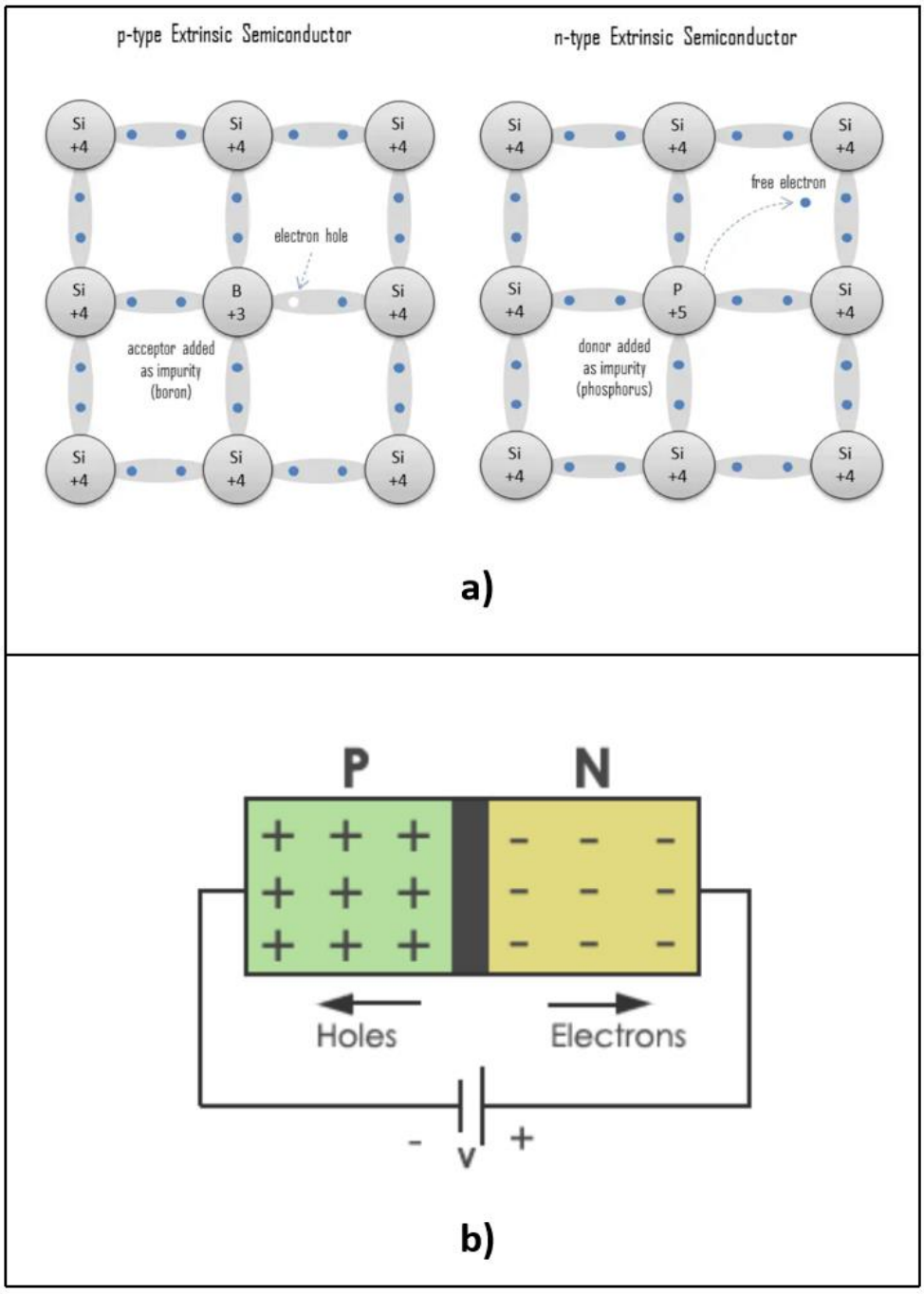

Figure 2.12

The pn-junction formed between the n-type and p-type silicon material showing the electric field created due to the depleted charges

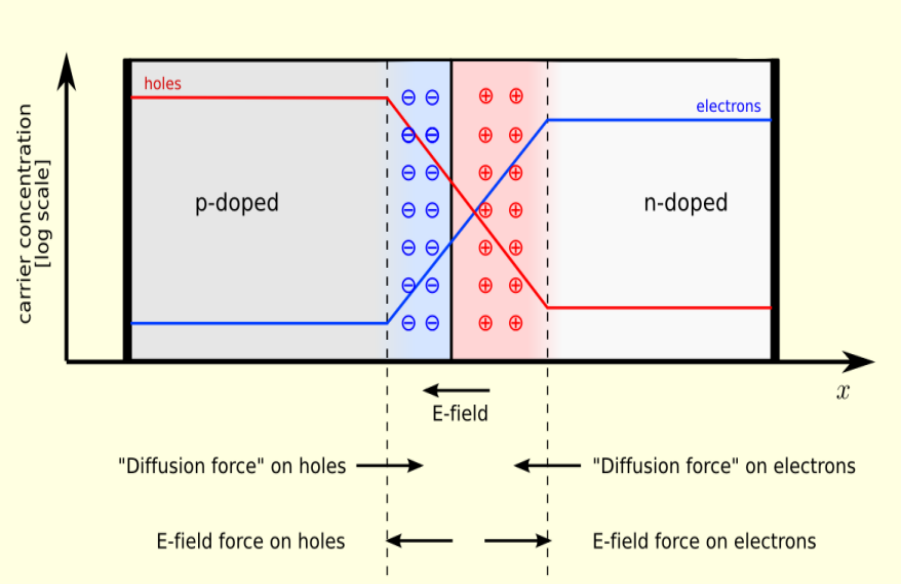

Figure 2.13

Track reconstruction: a) illustration of the track reconstruction for a charged particle resulted from the p-p collision and b) the high quality and low-quality track candidates

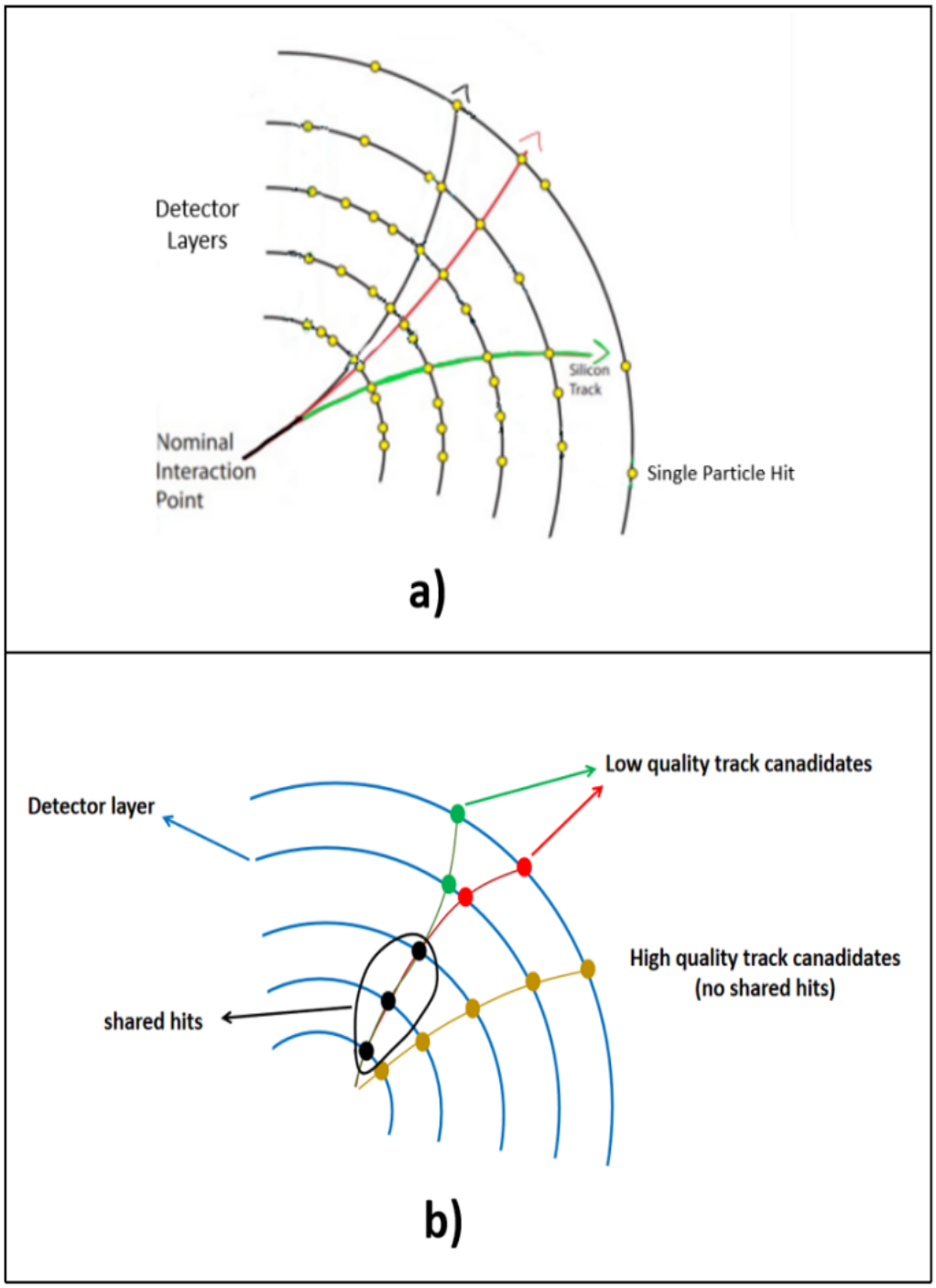

Figure 2.14

Particle path in ATLAS detector: a) the helical path that the particle resulted from the p-p collision takes while passing within the detector and b) particle trajectory in the magnetic field

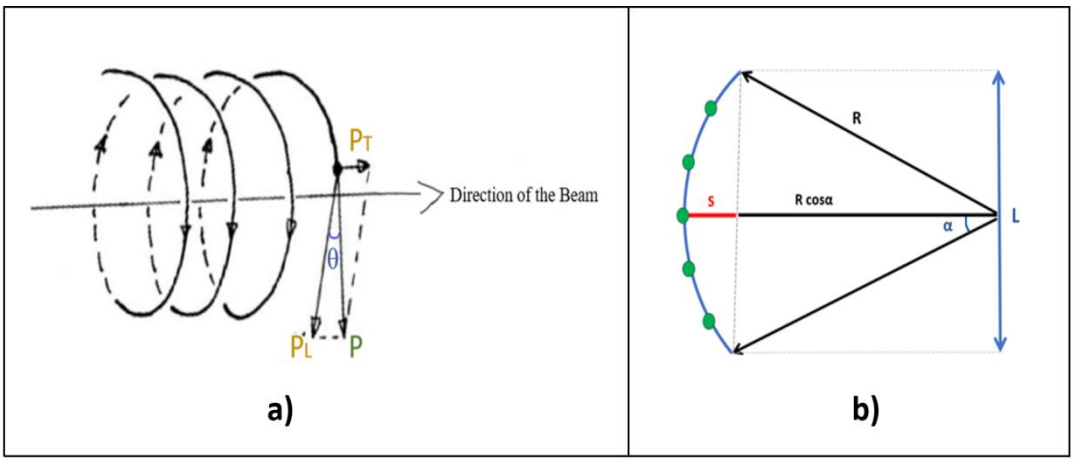

Figure 3.1

IBL of ATLAS detector: a) schematic view of the IBL of ATLASand b) schematic view of the pixel detector of the ID after inserting the IBL

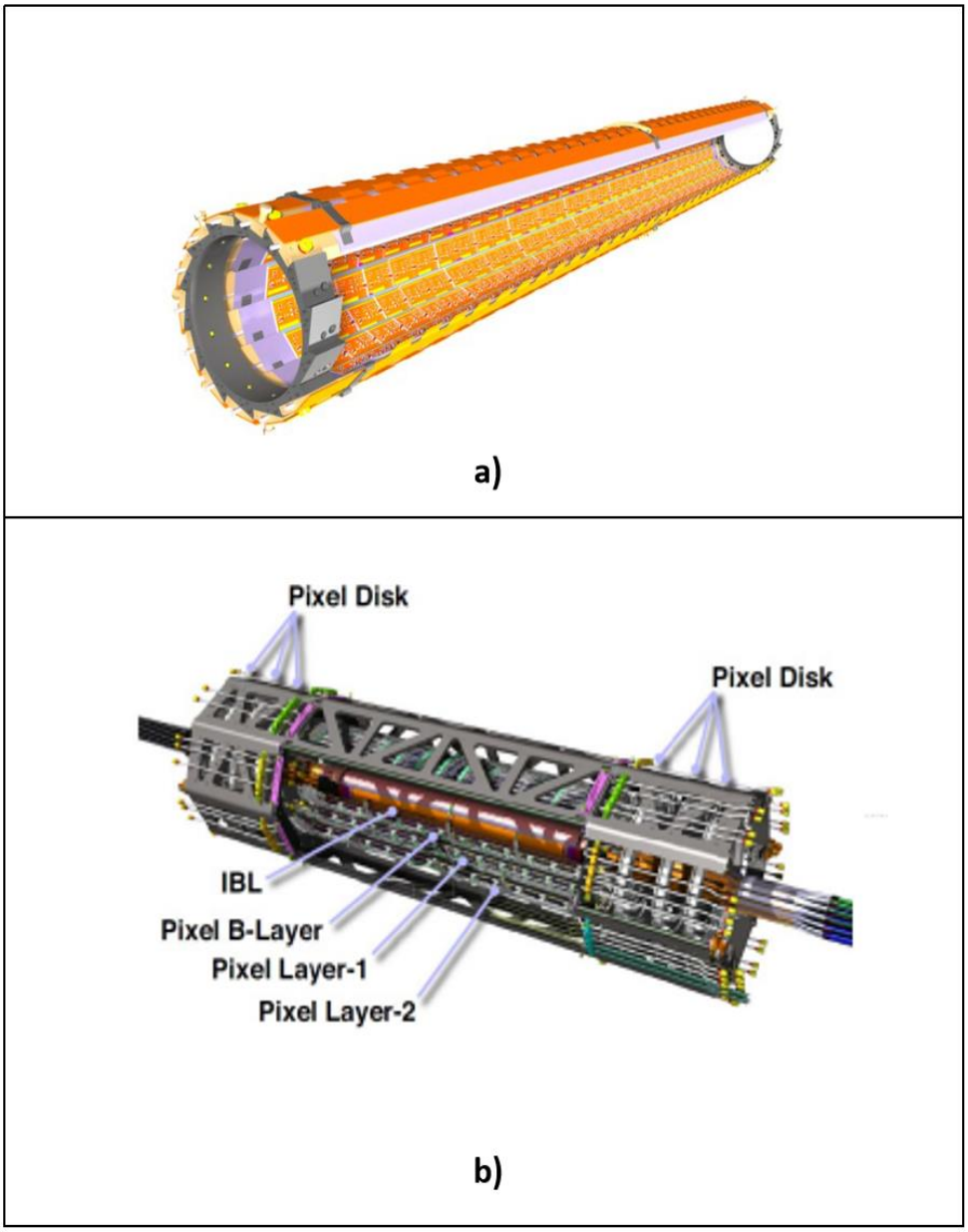

Figure 3.2

Comparison between the planar sensor and the 3D sensor

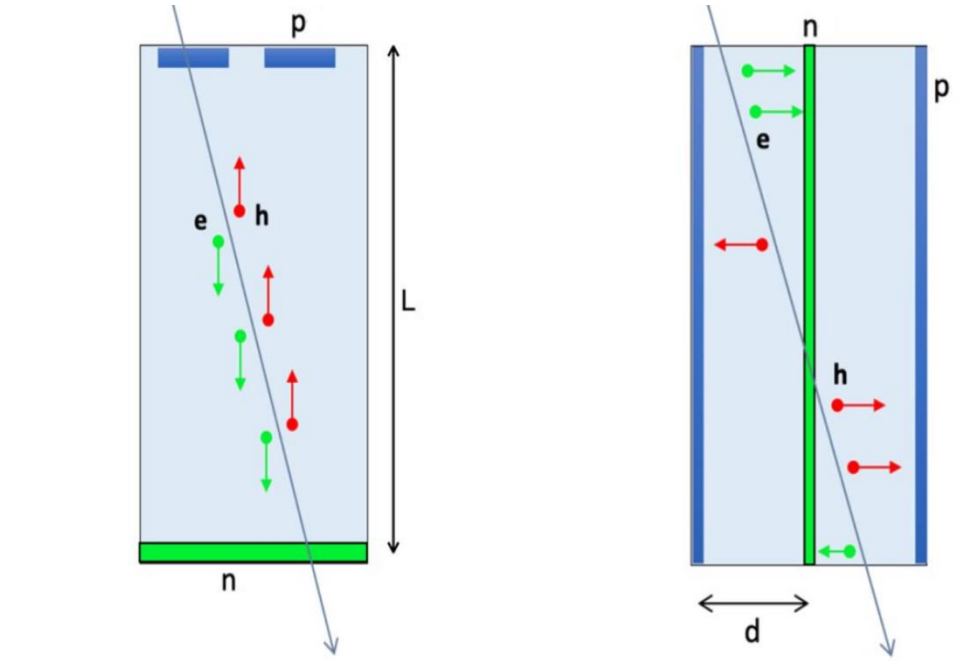

Planar silicon sensor
(L= Sensor thickness= Distance between electrodes)

3D silicon sensor
(d= Distance between electrodes)

Figure 3.3

Illustration of the single-particle clusters and merged clusters and how different particles trajectories collimate as a result of the increased PT

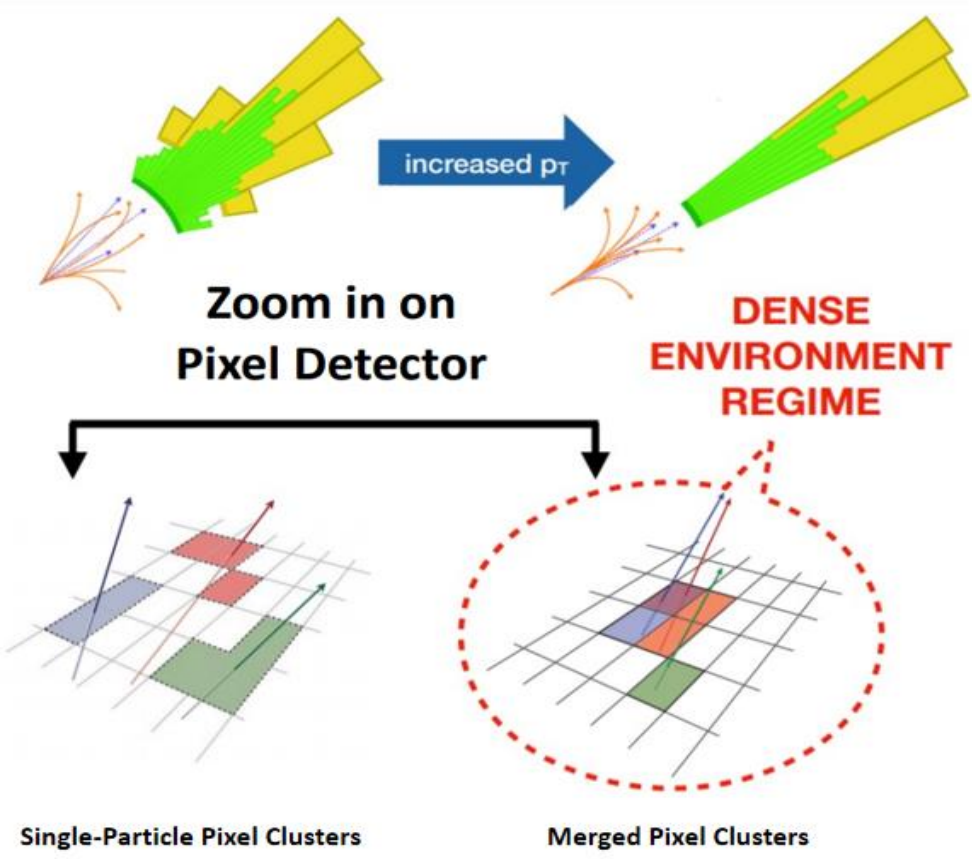

Figure 3.4

Schematic layout for the ITk of ATLAS detector

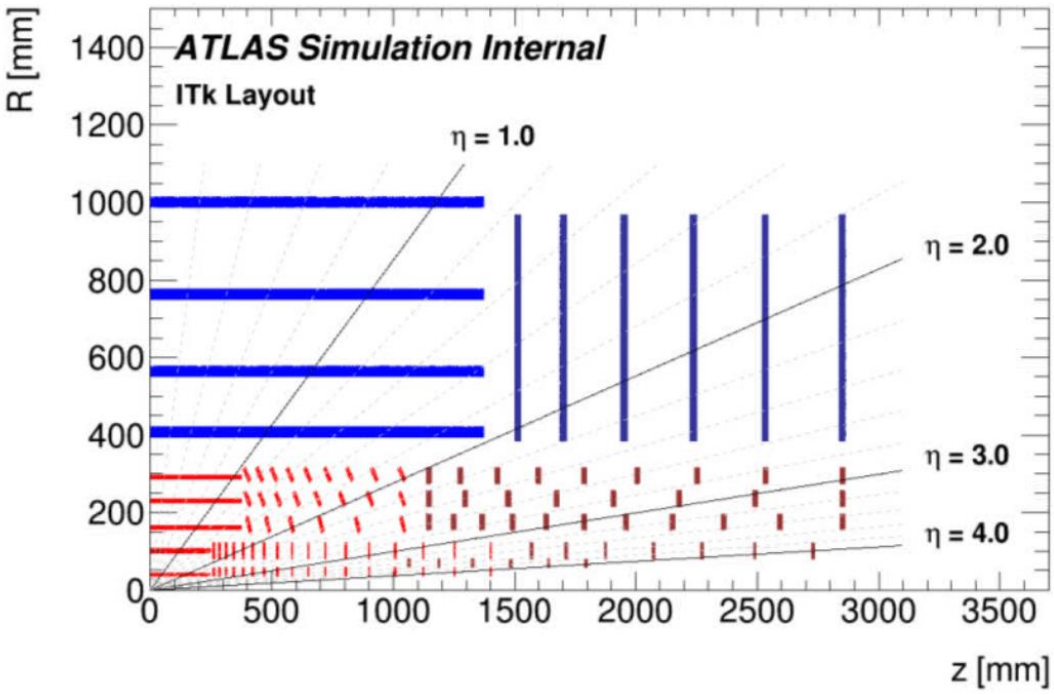

Figure 3.5

Layout of the ITk of ATLAS detector

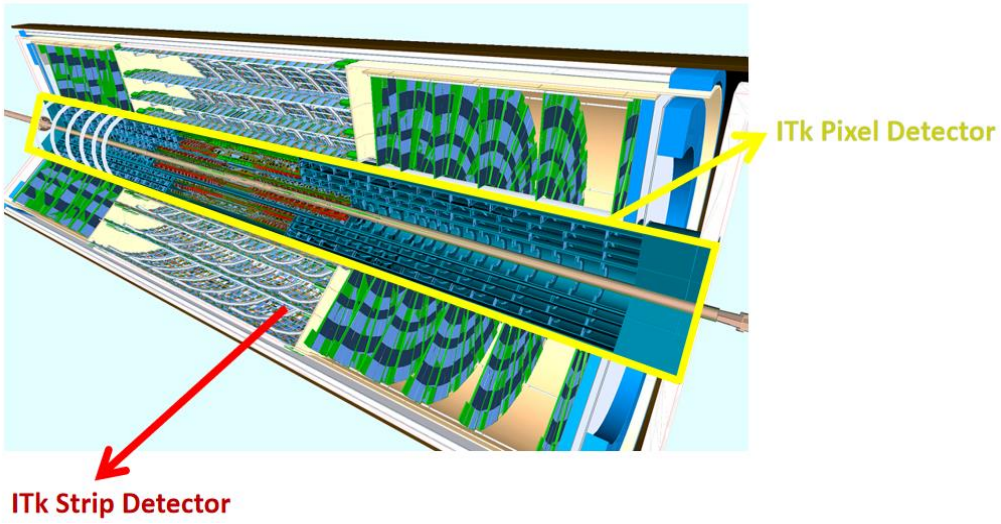

Figure 3.6

ITk's strip detector illustration: a) schematic view of the strip detector of the ITk of ATLAS and b) a petal from the strip disk

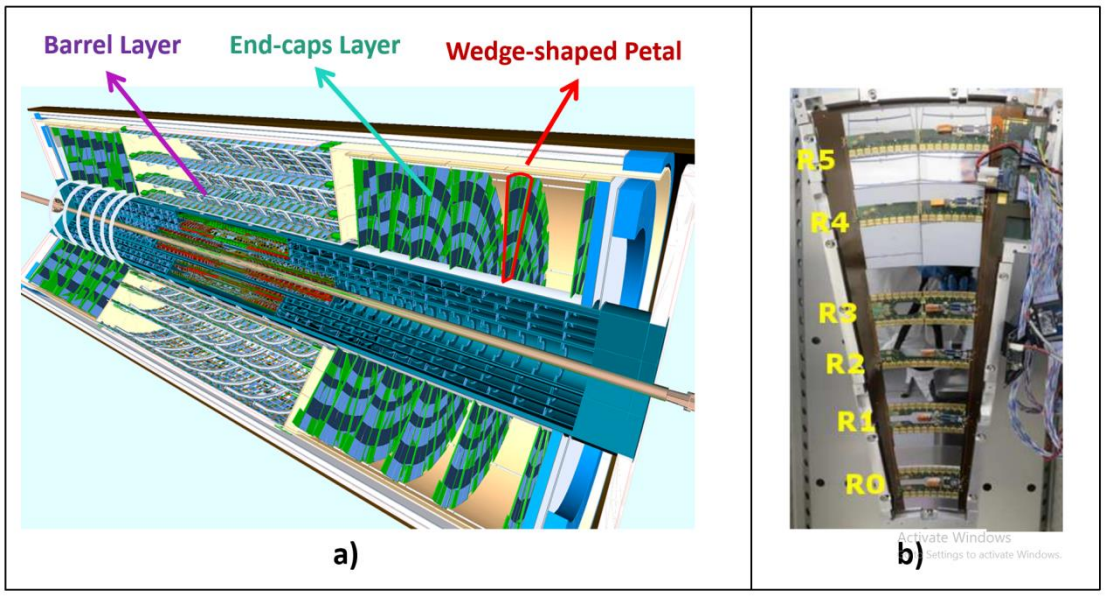

Figure 3.7

Schematic view for the short strip module

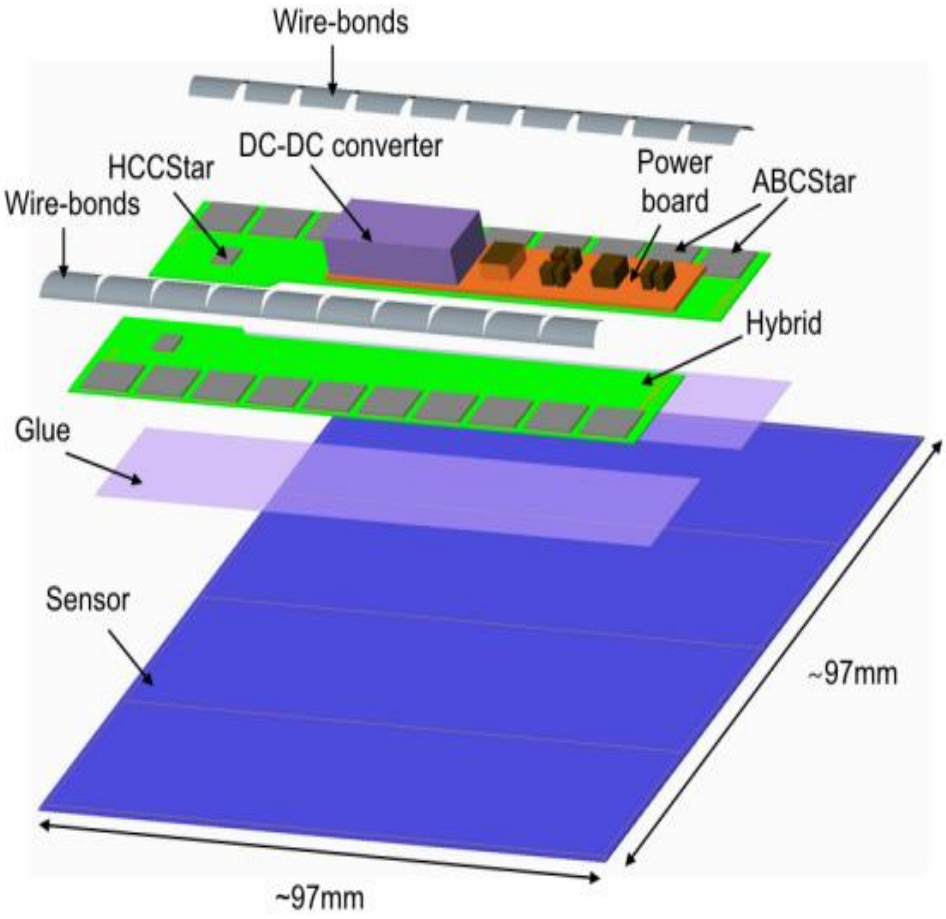

Figure 3.8

Inner system of the ITk's pixel detector: a) the three designs of rings used in the system and b) layout for one of the integrating quarters used to assemble the system

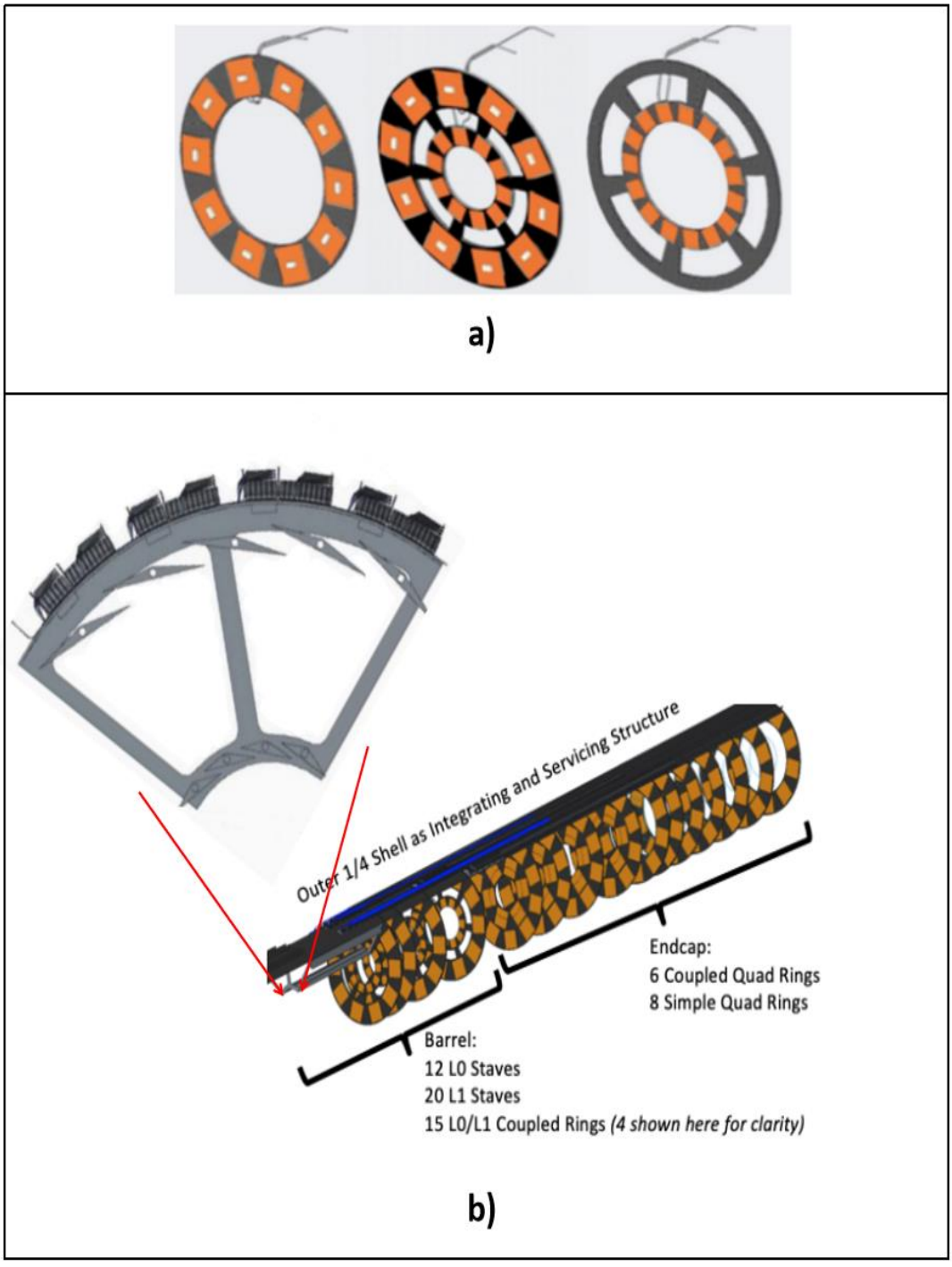

Figure 3.9

Local supports of the ITk's outer system

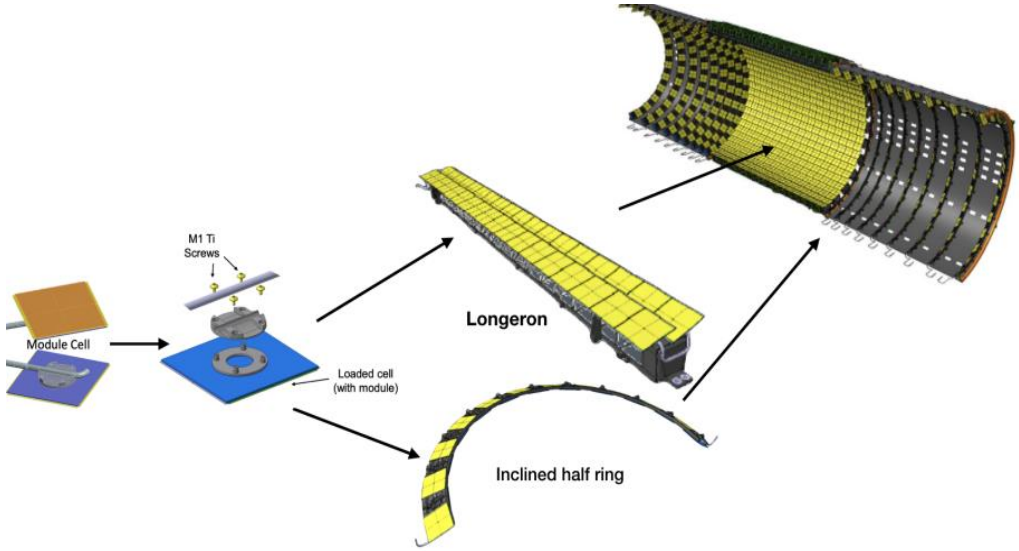

Figure 3.10

Illustration of how the particles resulted from the p-p collision tend to traverse the barrel layers of the pixel detector of the ITk

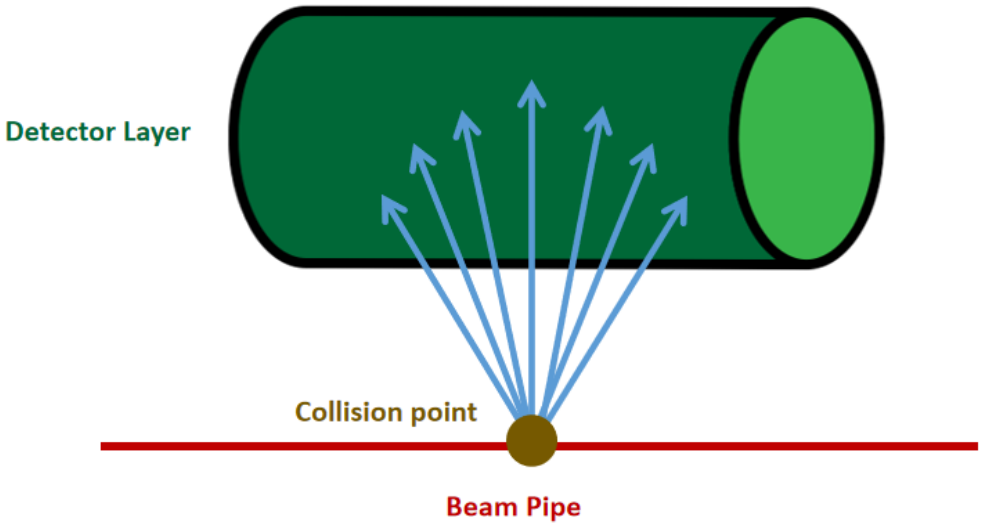

Figure 3.11

Outer system of the ITk's pixel detector: a) one of the two-sided half rings of the outer end-caps part and b) layout of one of the outer end-caps

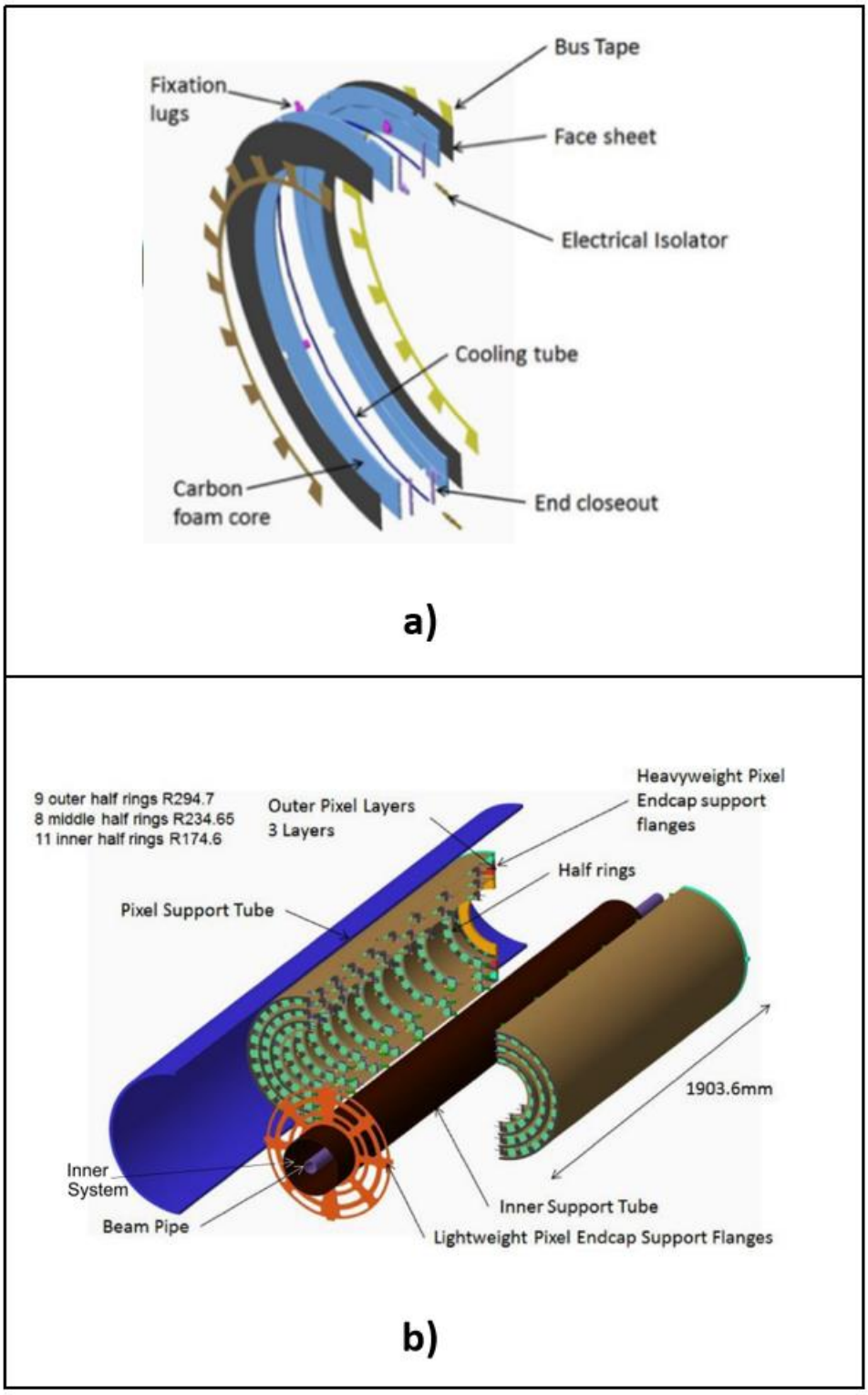

Figure 3.12

Modules of the ITk's pixel detector: a) cross section of the ITk's pixel modules, b) the barrel triplet module and c) the quad module

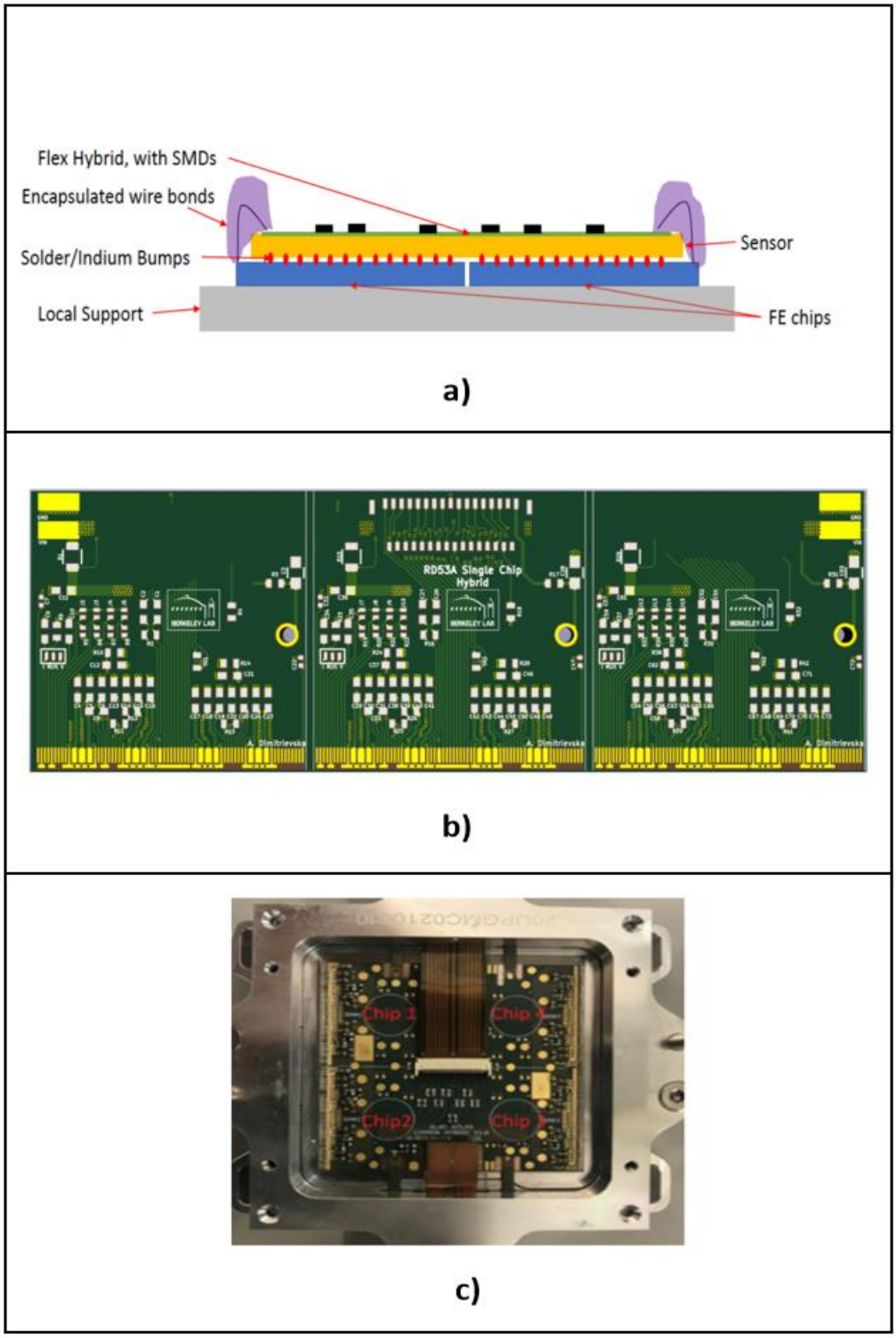

Figure 3.13

Comparison between the prototype chip RD53A and the RD53B chip of the pixel detector of the ITk of ATLAS

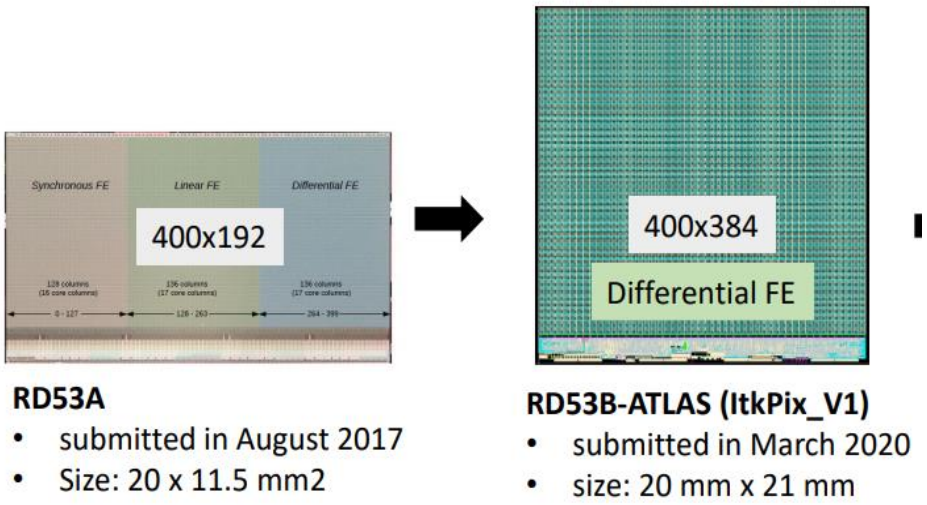

Figure 3.14

RD53B readout chip: a) floorplan of the chip and b) chip framework

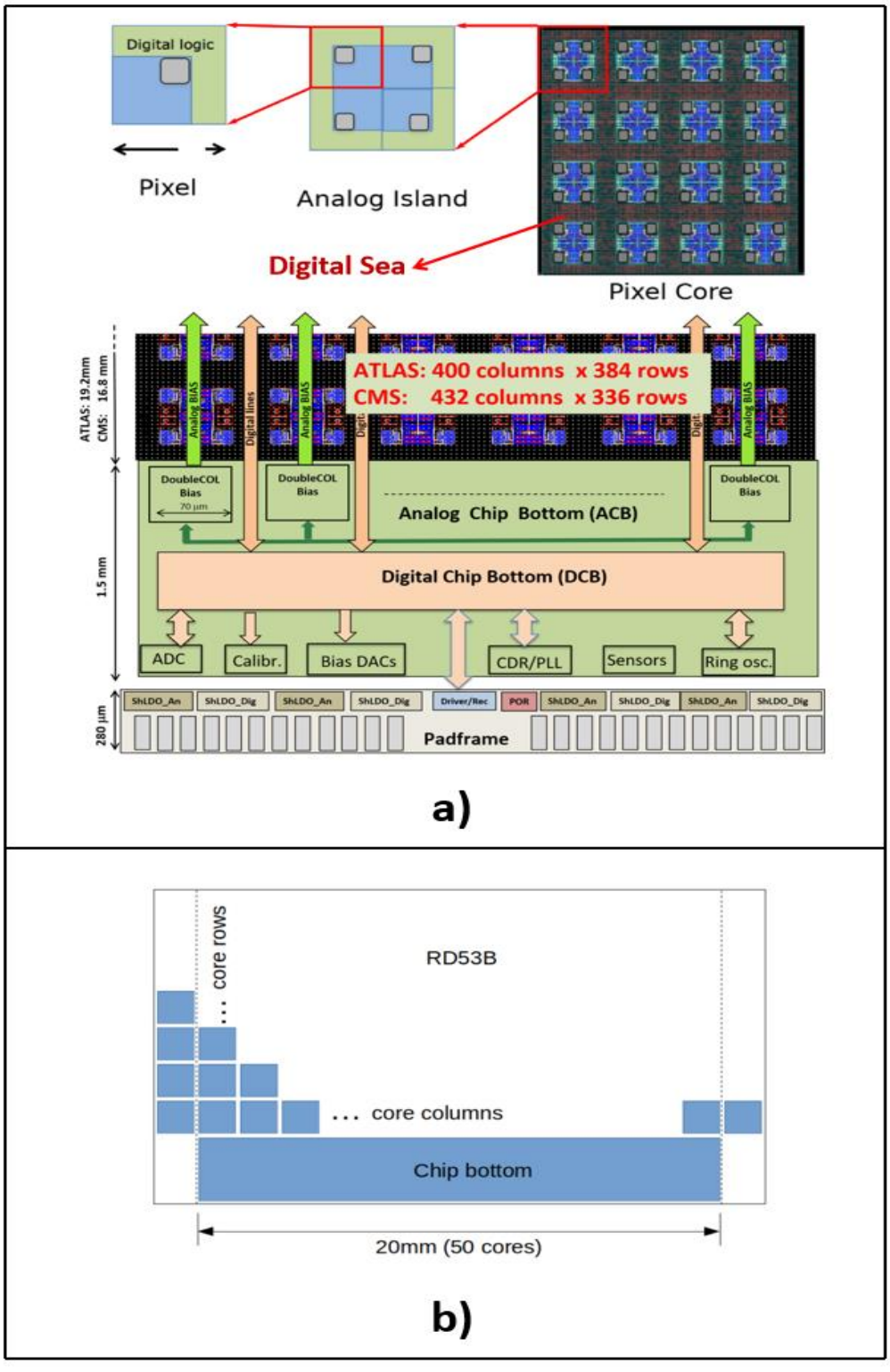

Figure 4.1

Module layers assembly: a) schematic view of the quad module layers and b) the stencil tool used to assemble the module

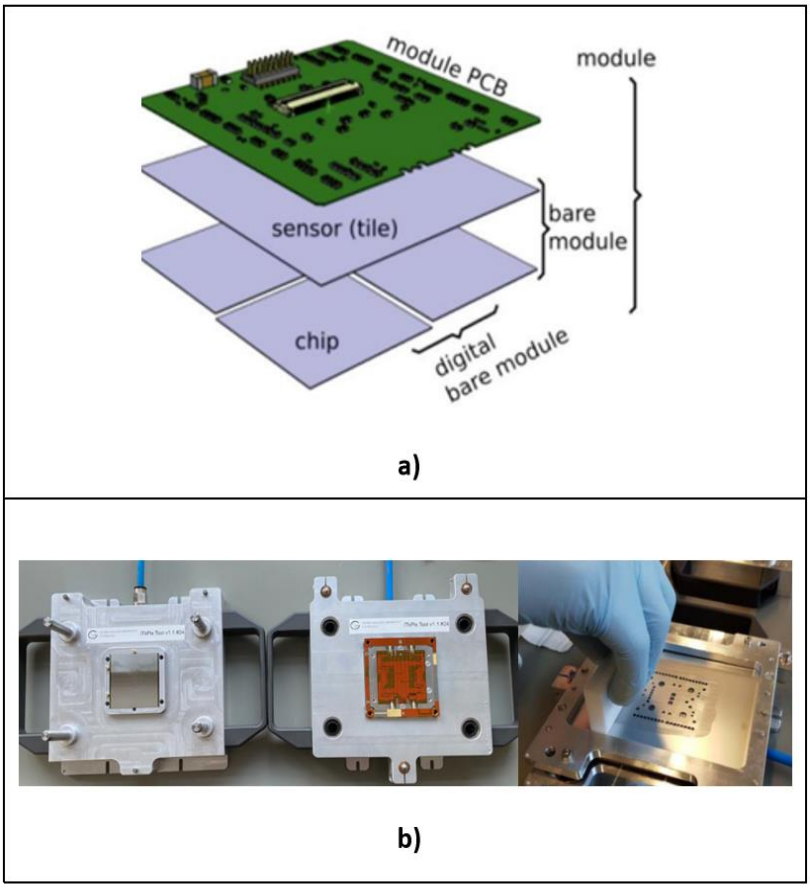

Figure 4.4

The knobs used to adjust the planarity of the chuck

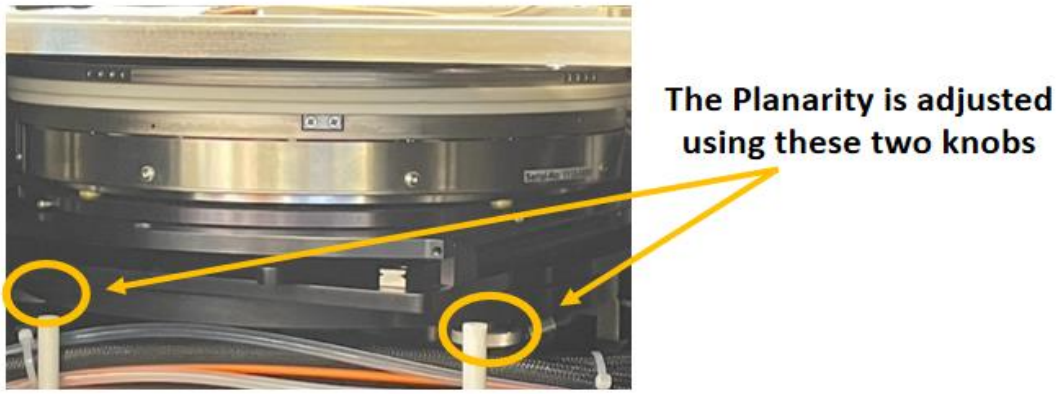

Figure 4.5

Yield map of the ITkPix-V1 Wafer

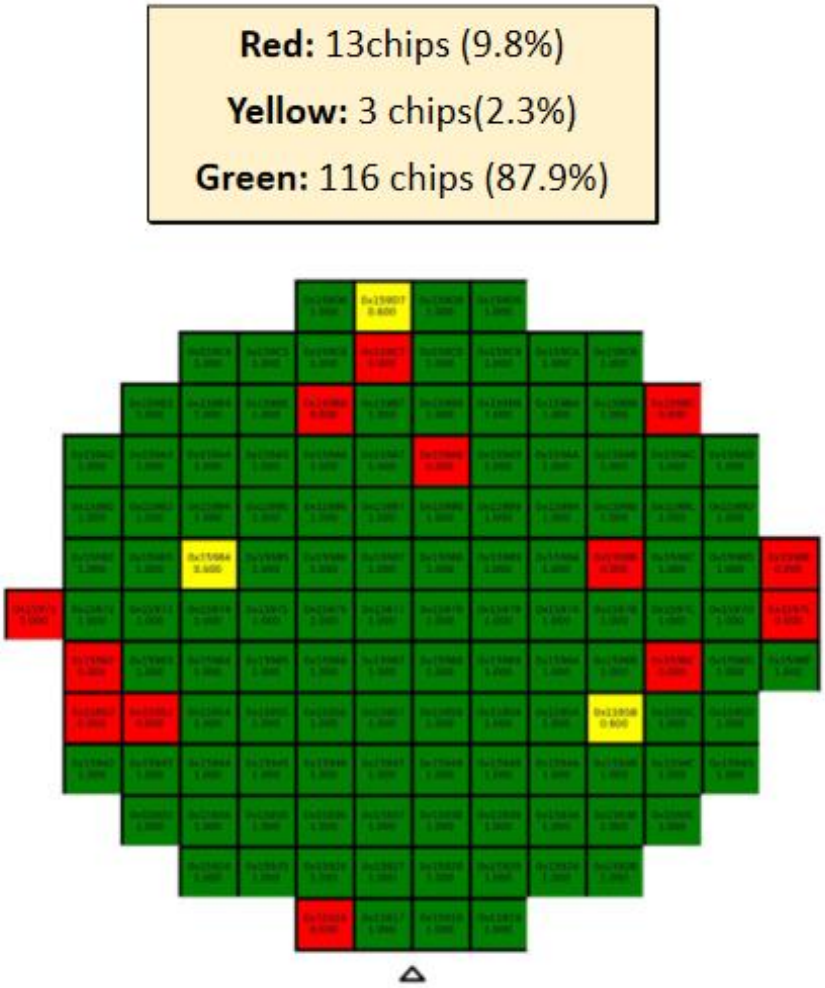

Figure 5.1

Screen-shot from one of the resulted YAML files for one of the tested chips from IJCLab's 48-hour test

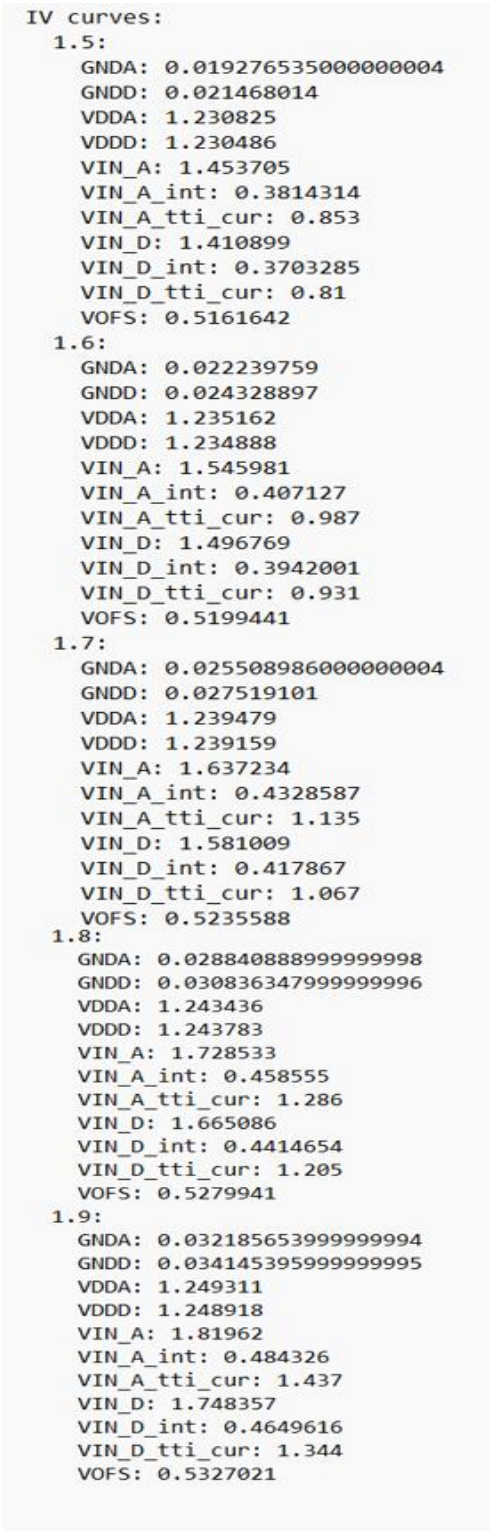

```
IV curves:
  1.5:
    GNDA: 0.019276535000000004
    GNDD: 0.021468014
    VDDA: 1.230825
    VDDD: 1.230486
    VIN_A: 1.453705
    VIN_A_int: 0.3814314
    VIN_A_tti_cur: 0.853
    VIN_D: 1.410899
    VIN_D_int: 0.3703285
    VIN_D_tti_cur: 0.81
    VOFS: 0.5161642
  1.6:
    GNDA: 0.022239759
    GNDD: 0.024328897
    VDDA: 1.235162
    VDDD: 1.234888
    VIN_A: 1.545981
    VIN_A_int: 0.407127
    VIN_A_tti_cur: 0.987
    VIN_D: 1.496769
    VIN_D_int: 0.3942001
    VIN_D_tti_cur: 0.931
    VOFS: 0.5199441
  1.7:
    GNDA: 0.025508986000000004
    GNDD: 0.027519101
    VDDA: 1.239479
    VDDD: 1.239159
    VIN_A: 1.637234
    VIN_A_int: 0.4328587
    VIN_A_tti_cur: 1.135
    VIN_D: 1.581009
    VIN_D_int: 0.417867
    VIN_D_tti_cur: 1.067
    VOFS: 0.5235588
  1.8:
    GNDA: 0.028840888999999998
    GNDD: 0.030836347999999996
    VDDA: 1.243436
    VDDD: 1.243783
    VIN_A: 1.728533
    VIN_A_int: 0.458555
    VIN_A_tti_cur: 1.286
    VIN_D: 1.665086
    VIN_D_int: 0.4414654
    VIN_D_tti_cur: 1.205
    VOFS: 0.5279941
  1.9:
    GNDA: 0.032185653999999994
    GNDD: 0.034145395999999995
    VDDA: 1.249311
    VDDD: 1.248918
    VIN_A: 1.81962
    VIN_A_int: 0.484326
    VIN_A_tti_cur: 1.437
    VIN_D: 1.748357
    VIN_D_int: 0.4649616
    VIN_D_tti_cur: 1.344
    VOFS: 0.5327021
```

Figure 5.8

Illustration of how the mis-alighnment of the chuck causes the wafer to be inclined

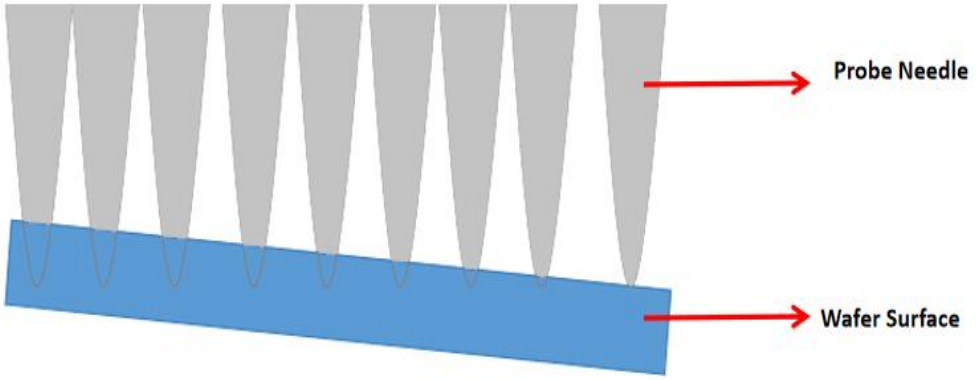

Figure 5.10

Schematic drawing illustrates both the separation of connection and the grounding solutions

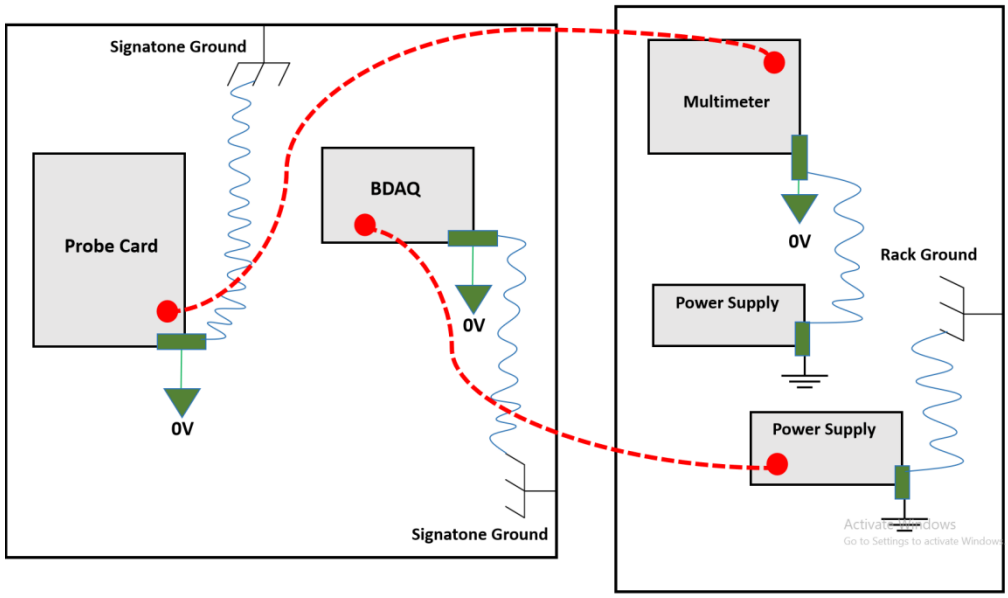

Figure 5.11

Two plots of the Iref Current and the Iref Trim Bit parameters values of the five-times test along with IJCLab's and Bonn's 48-hour test results for the 0x18944 chip

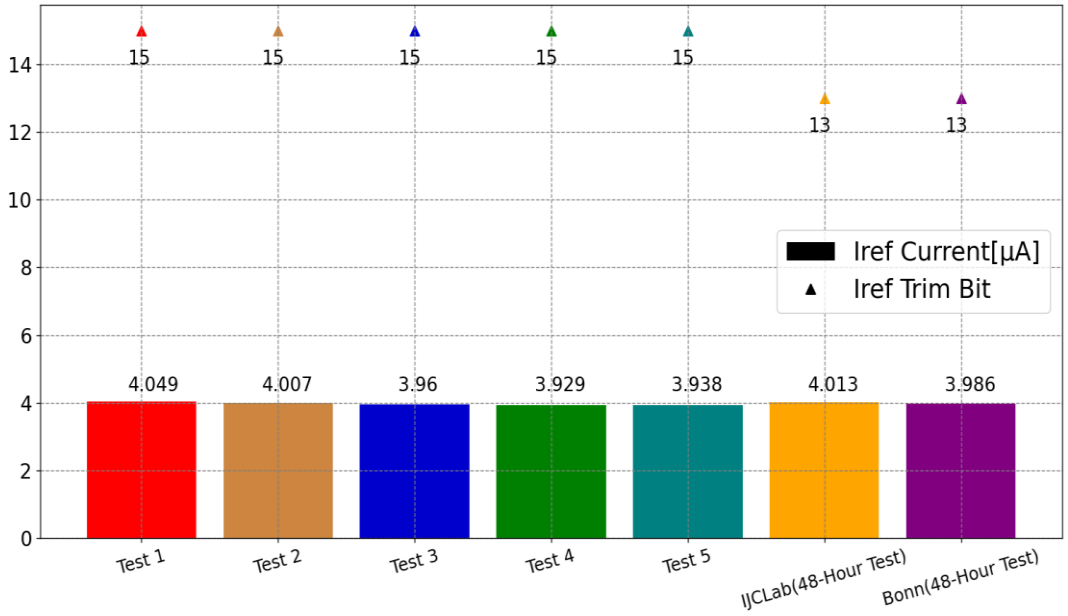

Figure 5.13

A picture under the microscope shows the dirt accumulated on the probe needles of the probe card

جـامعـــة النجاح الوطنية

كليـــة الدراســـات العليـــا

قياسات فحص الرقاقة ل ITkPix-V1 لترقية ITk Pixel ATLAS

إعداد

حسنية سليم محمد صلاحات

إشراف

د. أحمد بصلات

قدمت هذه الرسالة استكمالا لمتطلبات الحصول على درجة الماجستير في الفيزياء، من كلية الدراسات العليا، في جامعة النجاح الوطنية، نابلس– فلسطين.

2024

قياسات فحص الرقاقة ل ITkPix-V1 لترقية ITk Pixel ATLAS

إعداد

حسنية سليم محمد صلاحات

إشراف

د. أحمد بصلات

الملخص

هذه الأطروحة متعلقة بكاشف أطلس(ATLAS) الذي يعد أحد الكاشفات متعددة الأغراض لدى مصادم الهادرونات الكبير(LHC). داخل حلقة هذا المصادم، يتصادم شعاعان من الهادرونات. تم بناء كاشف أطلس و أجهزة كشف أخرى بغرض تتبع هذا التصادم والكشف عنه. حيث أن الكشف عن هذا التصادم سوف يمكن العلماء والباحثين من تحليله ودراسته، الأمر الذي سوف يساعد في التحقق من تنبؤات نظريات فيزياء الجسيمات المختلفة، مثل خصائص بوزون هيغز والذي يعد أمر بالغ الأهمية بالنسبة للنموذج القياسي للجسيمات الأولية.

يحتاج الباحثون إلى تعزيز أداء LHC من خلال زيادة اللمعان المتكامل بما يتجاوز عشرة أضعاف قيمته التصميمية بغرض زيادة إمكانية الاكتشافات في سنة 2029, حيث يطلق على المصادم في مرحلة اللمعان العالي هذه (HL−LHC). لهذا السبب, يخضع كاشف أطلس لعمليات ترقية متعددة حتى يتناسب أدائه مع ظروف اللمعان العالي التي سوف تتواجد في فترة HL−LHC. أحد عمليات الترقية هذه تهدف إلى استبدال كاشفه الداخلي الذي يتكون جزئيًا من السيليكون بمتتبع داخلي جديد يتكون من السيليكون فقط ويتمتع بأداء محسن مقارنة بالكاشف الداخلي الحالي ويطلق عليه اسم (ITk) ويتكون من كاشف شريط وكاشف بكسل.

الوحدات الأساسية المكونة لكاشف البكسل هي (Pixel modules) واللتي تحتوي على رقائق سيليكون للقراءة. يجب أن تخضع رقائق السيليكون هذه لعمليات مراقبة جودة عن طريق خضوعها لاختبارات كهربائية تسمى اختبارات فحص الرقاقة (Wafer Probing Tests) لنتمكن من تحديد مدى ملاءمة هذه الرقائق لاستخدامها في بناء وحدات البكسل. ولكن قبل ذلك، يجب أن تخضع الأجهزة المستعملة في إجراء هذ الاختبارات لعملية مراقبة جودة بهدف تحديد مدى ملاءمتها لإجراء هذه الاختبارات ومدى صحة النتائج التي نحصل عليها منها. أحد هذه الأجهزة يتواجد

في مختبر (IJCLab) الواقع في منطقة أورسي في فرنسا. تتم عملية مراقبة جودة الجهاز عن طريق إجراء الاختبارات على رقائق السيليكون التي تحمل اسم (ITkPix−V1) .

لذا فإن الموضوع الرئيسي لهذه الأطروحة هو تحليل نتائج الاختبارات التي تم إجراؤها على هذه الرقائق بواسطة جهاز فحص الرقاقة في مختبر IJCLab ومقارنتها بالقياسات المرجعية من جامعة بون والتي أجرت نفس الاختبارات على نفس الرقائق وحصلت على نتائج جيدة جداً من أجل المساعدة في تأهيل الجهاز ليقوم باختبارات الفحص. كانت بعض نتائج الاختبارات مشابهة للنتائج المرجعية وبعضها الاخر لم يكن كذلك و اعتماداً على التحليل اللذي تم اجراؤه تم العثور على بعض الأسباب اللتي سببت النتائج البعيدة عن النتائج المرجعية.

الكلمات المفتاحية: ITkPix−V1, ITk, HL−LHC, LHC, ATLAS.